Politecnico di Milano
Dept. of Aerospace Science and Technology
Master of Science in Space Engineering

Attitude and Orbital Dynamics Coupling for High Area-to-Mass Ratio Spacecraft for the OUFTI-Next 3U Cubesat and the ZodiArt iSEE MicroSat missions

Master Thesis of:
Cristiano Contini
ID:
872867

Supervisor at Politecnico di Milano:
Prof. Camilla Colombo
Supervisor at University of Liége:
Prof. Gaëtan Kerschen

Academic year 2018/19

Dedicated to my grandparents and to the seekers of adventure in Space

ABSTRACT

Nec refert quibus adsistas regionibus eius, usque adeo quem quisque locum possedit, in omnís tantundem partís infinitum omnem relinquit. Praeterea si iam finitum constituatur omne quod est spatium, si quis procurrat ad oras ultimus extremas iaciatque volatile telum, id validis utrum contortum viribus ire quo fuerit missum mavis longeque volare, an prohibere aliquid censes obstareque posse?

Lucrezio, *De Rerum Natura*, I, 951/983

MODERN spacecrafts are characterised by peculiar shapes, optimised for advanced scientific and commercial activities. Moreover, interests in satellites large constellations or MicroSat in formation flying are increasing and, as a consequence, also the challenges related to the Attitude Determination and Control Subsystem, being related to the capability to sustain uncommon disturbances torques, to enhance a fine pointing budget and to be able to take into account the coupling between attitude and orbital dynamics. In this Thesis two Attitude Determination and Control Subsystem simulators build in Matlab/Simulink^{TM}will be presented, one dynamically decoupled and exploited to provide simulations for the OUFTI-Next 3U CubeSat mission, by Centre Spatial de Liége and the University of Liége, and one coupled, fundamental to evidence the fine coupling between orbital and attitude dynamics in the ZodiArt iSEE mission, by Politecnico di Milano. Both of the simulators are characterised by a complete disturbances model, including the Earth zonal harmonics, the Moon and Sun third body perturbations, solar radiation pressure, drag and lift. In particular, solar radiation pressure and drag/lift coupled effects on satellite fine relative positioning, while orbiting in formation, will be presented in a compact set of plots, here called *Orbital long-track*

envelopes. Thanks to the tool implemented, these analyses can be generalised to every kind of small satellites and orbit. In addition, peculiarities, opportunities and criticalities of the previously mentioned missions will be inspected and fully described.

I moderni veicoli spaziali sono caratterizzati da forme peculiari, ottimizzate per scopi scientifici e commerciali. L'interesse nelle grandi costellazioni di satelliti e il volo in formazione di microsatelliti sta crescendo e conseguentemente il controllo e la determinazione dell'assetto stanno diventando sfide sempre più impegnative, poiché, per assicurare un'elevata precisione di puntamento, dovranno far fronte a disturbi sempre più complessi a causa dell'accoppiamento fra dinamica orbitale e di assetto. In questa Tesi verranno presentati due simulatori del sottosistema deputato al controllo e alla determinazione di assetto, implementati in Matlab/Simulink: il primo, a dinamiche disaccoppiate, è stato utilizzato per simulare la missione OUFTI-Next 3U CubeSat, patrocinata dal Centre Spatial de Liége e dall'Università di Liegi; il secondo, a dinamiche accoppiate, è stato invece fondamentale per la missione ZodiArt iSEE, patrocinata dal Politecnico di Milano. Entrambi i simulatori sono caratterizzati da un modello di disturbi completo di non sfericità terrestre, perturbazioni di terzo corpo provocate da Luna e Sole, pressione di radiazione solare, resistenza e portanza aerodinamiche. In particolare, gli effetti accoppiati della pressione di radiazione solare e della resistenza/portanza sul posizionamento relativo dei satelliti durante il volo in formazione, verranno presentati in grafici compatti, qui chiamati *Orbital long-track envelopes*. Grazie agli strumenti implementati, queste analisi possono essere eseguite per ogni tipo di satellite e di orbita. Verranno infine ampiamente descritte anche peculiarità, potenzialità e criticità delle sopracitate missioni.

ACKNOWLEDGEMENTS

We are only as strong as we are united,
as weak as we are divided.

Albus Dumbledore, J.K. Rowling

THIS work and the life experiences related to it have been possible thanks to Professor Camilla Colombo, who first introduced me to the European dimension of the Space Engineering. She encouraged me to leave Italy and start a new and unexpected adventure, that made me know a wonderful country and meet amazing people. Then, I wish to thank Prof. Gaëtan Kerschen and Dr. Xavier Werner who made me feel part of a big family, since the first day I arrived. They transmitted me their enthusiasm and let me be part of the OUFTI-Next project. Their support and encouragement have been fundamental to me during the months I spent in Liége. The opportunity to design a machine that will fly in space is the dream of every Space Engineering student, continuously inspired by the human desire to go beyond the limits, try what nobody could do before and explore the unknown.
During the months spent in Liége, I had the pleasure to show and compare my work with Tjorven Delabie by KULeuven and I want to thanks him for the fundamental informations and data about the *KULeuven ADCS unit* he provided me. Thanks also to Klemen Košir for sharing with me the latest results about SRI401 cryocooler structural tests. The animations produced with STK by AGI have been possible only thanks to Fabrizio Gemma, GMSPAZIO Marketing Manager, who allowed me to have part of the software's Pro licence.
A special thanks goes to my relatives, my father Paolo, my mother Giovanna and my brother Edoardo, who trusted and supported me during this years of studies, efforts, difficulties and successes, you have always been the polar star of my life.

I wish to thank in particular my girlfriend and adventure companion Barbara, who makes me always see what is good on Earth with respect to space. You are the one who inspired me the desire to travel and see this world with great enthusiasm.
Thanks also to ASSYST team: Andrea P., Luca M., Andrea S., Adriano G., Francesca S., Paolo V., Giovanni B., Andrea G. and Marco G. who taught me how to work in team, being my family for almost a semester and especially to Francesca, Andrea P. and Luca, who shared with me their elegant pieces of code.
Thanks to Alberto Della Noce, for the afternoons spent reasoning about aerodynamics forces and for the great and challenging night-matches against me and Simone. Finally, a special thanks goes to Simone, who supported, helped and beared me -under the effects of caffeine and not- everyday, during the years of our University career. I hope all your dreams will come true.

TABLE OF CONTENTS

LIST OF FIGURES

LIST OF TABLES

Part I

The Attitude-Orbit Coupled Simulator Architecture

CHAPTER 1

INTRODUCTION

男の夢...決して死ぬことはない!
A man's dream...will never end!

Eiichirō Oda

NOWADAYS spacecrafts are designed with complex shapes and large surfaces, in order to accomplish peculiar mission objectives, maintaining a low mass to reduce the launch cost. Moreover, the possibility to launch clusters of small satellites in formation flying is becoming reality and a precise knowledge of the relative position among the platforms will be mandatory. As a result, for Earth observation satellites, aerodynamic drag and solar radiation pressure become the main actors, driving and coupling the orbital dynamics with the attitude one. This is the case of the ZodiArt iSEE mission [1], a new mission design carried out by Politecnico di Milano and lead by Prof. Camilla Colombo, whose aim is to launch a set of MicroSat, each of them equipped with a reflective balloon, to promote space advertisement during twilight time and to enhance Earth observation during day time.
The challenges related to the dynamics of such a peculiar spacecraft are mostly related to the Attitude Determination and Control Subsystem (ADCS), since the

platform is characterised by high and uncommon, for this class of spacecraft, disturbances torques and a complex operative scenario such a constellation orbiting in formation. In these cases the modelling and simulation of attitude determination and control subsystem, coupled with the perturbed orbital dynamics, become of fundamental importance. In this Thesis an ADCS simulator built in Matlab/Simulink^{TM}is presented, whose dynamically decoupled version was exploited to provide simulations for the OUFTI-Next 3U CubeSat mission, by Centre Spatial de Liége (CSL) and the University of Liége (ULiége), while the coupled version was fundamental to evidence the fine coupling between orbital and attitude dynamics in the ZodiArt iSEE mission, by Politecnico di Milano. The simulator is characterised by a complete disturbances model, including the Earth zonal harmonics, the Moon and Sun third body perturbations, Solar Radiation Pressure (SRP), drag and lift, capable of providing reliable and accurate results in terms of actuators and sensors sizing, as well as in terms of mission operation simulations.

1.1 Literature review

1.1.1 Attitude-orbital coupled simulators

The spacecraft ADCS simulators are usually characterised by an orbit propagator decoupled from the attitude dynamics, as reported in [2], and neglect the coupling introduced by atmospheric drag, lift and solar radiation pressure, since the orbit perturbation induced by these forces can be counteracted with station keeping manoeuvres performed periodically. Nevertheless, as a consequence of the CubeSat and MicroSat missions wide-spreading [3], cheap station keeping and formation flying strategies, exploiting natural perturbations, are required. The analyses of the coupling forces effects are not new in literature: for instance in [4] the coupling effect of the solar radiation pressure on high area-to-mass ratio satellites is inspected, but neglecting atmospheric lift and drag. Other works analyse the drag and lift only, but their model are quite simplified. Here are reported the most common approximations in works related to the use of drag and lift to control spacecrafts:

- Drag is oriented only in the direction of the spacecraft velocity, under the assumption of low inclination orbits, in order to neglect the cross-track effects, as done in [5], where no SRP was considered.
- Perturbative accelerations due to drag and lift are assumed to have a constant and given value and their effect was studied in [6], decoupling the attitude-orbit dynamics and focusing on the relative motion of two small satellites while performing a rendezvous.

Moreover, in none of the previous works there is a complete disturbances model representing also all the other common external disturbances acting on a spacecraft such as:

- Earth zonal harmonics.
- Third body perturbations due to Sun and Moon.

It is worth mentioning that a coupled simulator implementing a complete disturbances model, considering all the orbit and attitude perturbative forces and torques, is an high fidelity model, which was never implemented in the reviewed academic literature and that will become more important in future studies about formation flying precise manoeuvreing. For instance, ESA provides an high-fidelity and standardised Simulink^{TM}perturbances model, called PEET, [7], which comprehends all the perturbations affecting the pointing error, but it can not directly provide results on the orbital dynamics, coupled with the attitude one. A similar work to this Thesis, but based on J_2 and drag effects only, was performed in [8], where also an anti-disturbance cooperative controller is proposed to achieve relative position keeping and small attitude angle tracking simultaneously. In [9], instead, an attitude-orbital coupled simulator is developed to consider the effects of the vectored thrust on attitude dynamics, but no coupling disturbances are considered. For what concerns instead the model implementation, in the literature there are several examples of unified models based on quaternions or non-physical variables to model the orbital-attitude dynamics, such as the one reported in [10]. However, as explained in the same paper, non-physical variables are not broadly employed in current sensors and actuators; as a consequence, in the Thesis it was decided not to adopt a unified variable model.

1.1.2 Reflective balloons missions

Large inflatable or deployable surfaces have been inspected through the years, mainly based on three geometrical shapes: flat plate, pyramid and sphere, [11]. In the ZodiArt mission the shape selected was the sphere, mainly due to the fact that attitude control is not requested to orientate the balloon with respect to the Sun direction. This simplifies the control action, but does not allow to exploit completely the drag, lift and solar radiation pressure perturbations to drive the spacecraft attitude and orbital dynamics. In fact, the sphere does not produce lift if not put in rotation with respect to the relative wind, [12].
The pyramidal shape worths to be mentioned, since it is characterised by the best stowed volume and mass ratio, [13]. Nevertheless, with respect to the solar sail, it has never been tested in space, even if an inflatable deployment pyramidal structure has been tested on Earth, [14].

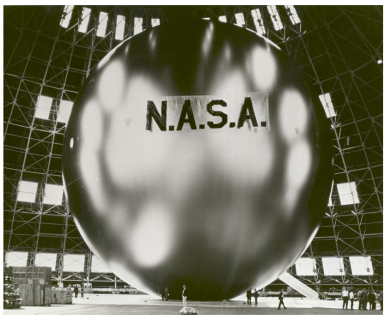

(a)

(b)

Figure 1.1: *Example of balloon missions: Echo I, [18] and Humanity Star, [16].*

The most used materials used to produce solar sails are: aluminised Mylar, aluminised Mylar with a chromium back surface, aluminised Colorless Polyamide (LaRCTM CP1) and aluminised Kapton, [15].
Humanity star is an example of Space sensibilisation activities, launched by Rocket Lab. on 21^{st} of January 2018, Figure 1.1 *(b)*, [16]. It consisted in a one-meter-tall carbon fiber geodesic sphere made up of 65 highly reflective panels. From ground it appeared as a shooting star passing every 90 minutes. The aim of the mission was to build a symbol in the night sky that encourages everyone to look up and to reflect about humanity's place as one species on a small planet in a vast universe, [16]. Other missions with high reflective balloons were placed on orbit, like Echo I, Figure 1.1 *(a)*, Echo II and PAGEOS I, whose balloon had the same dimensions and material of Echo I: 30.48 m diameter, made in Mylar with vapor deposited aluminum. The details about each of these missions and the comparison with similar ones can be found in [17]. Another example of the use of large inflatable balloons is the Gossamer Orbit Lowering Device (GOLD), [19], which can modulate the balloon cross section area, but does not embark a dedicated ADCS. Differently from the previously mentioned missions, which are not characterised by any control system, the challenge for the ADCS of the ZodiArt iSEE platform is to counteract the high environmental disturbances torques induced by the large distance between the MicroSat centre of mass and centre of pressure.

1.2 Thesis contributions

The aim for the Thesis is to develop a tool to simulate the ADCS, characterized by a complete disturbances model and capable to evidence the orbital-attitude coupling in high area-to-mass spacecraft. Moreover, the simulator will be able to provide analysis about the differential height and shift achieved performing a differential drag/lift manoeuvre, under the effect of all the previously mentioned

perturbances, at different epochs, in function of the platform angle of attack and given the initial true anomaly. The tool implemented can be generalized to any kind of spacecraft and in this Thesis it will be used to size both the OUFTI-Next and the ZodiArt ADCS, providing simulations about their nominal mission profiles, as well as analyses about each project peculiarities, proving its versatility and robustness.

1.3 Thesis outline

The Thesis is subdivided in four parts: Part I addresses the simulator architecture description, from the preliminary orbital-attitude decoupled model, presented in Chapter 2, to the final dynamically coupled one, reported in Chapter 3; in Part II Chapter 4 to 6 are dedicated to the OUFTI-Next platform ADCS sizing, exploiting the simulator decoupled version, while, in Chapter 7, analyses about mission peculiarities and emergency modes are provided; In Part III the orbital-attitude coupled simulator is exploited to size the ZodiArt platform ADCS, as presented in Chapter 9 and 10, where simulations about the nominal mission profile are provided, as well as the perturbations effects on orbit propagation. In Chapter 11, instead, the fine coupling between orbital and attitude dynamics while performing differential drag is analysed. Finally, Part IV is dedicated to the Thesis general conclusions.

CHAPTER 2

ORBITAL-ATTITUDE DECOUPLED SIMULATOR

In this chapter the decoupled simulator implementation is described. Firstly, the nomenclature and reference frames used in this Thesis, as well as a general overview about the ADCS loop are presented in Section 2.1 and 2.3. Section 2.4 to 2.9 address the characterisation of each element of the ADCS loop. Finally in Section 2.10 the differential equations solver choice and numerical stability analysis are reported.

2.1 Nomenclature and reference frames

In the Thesis, three main reference systems are used: the *inertial reference frame*, the non-inertial *body-fixed reference frame* and *Local Vertical Local Horizontal (LVLH) reference frame*. The first one has its origin in the centre of the Earth, its X-axis is oriented towards the vernal direction and the Z-axis is pointed towards the North Pole. The second reference frame instead is a non-inertial frame, centred in the spacecraft centre of mass and dependent on the platform considered (in Part II and III this reference frame will be presented respectively for the OUFTI-Next and the ZodiArt platforms). The last reference frame is also a non-inertial reference frame whose orthogonal unit vectors are $\hat{\mathbf{r}}$, $\hat{\mathbf{s}}$ and $\hat{\mathbf{w}}$, where $\hat{\mathbf{r}}$ is the osculating

position vector direction. $\hat{\mathbf{w}}$, instead, is the unit vector normal to the osculating orbital plane, in the direction of angular momentum vector $\boldsymbol{h_m}$, the transverse vector $\hat{\mathbf{s}}$ is normal to both $\mathbf{r}$ and $\hat{\mathbf{w}}$ and it therefore points in the direction of the orbiting body's local horizon, as shown in Figure 2.1, where u is the argument of latitude.

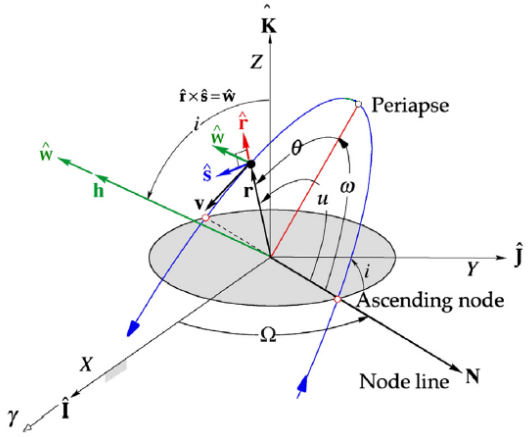

Figure 2.1: *The local vertical local horizon $\hat{\boldsymbol{r}}\hat{\boldsymbol{s}}\hat{\boldsymbol{w}}$ frame [20].*

The subscript $(\cdot)_{b/n}$, means a rotation from the *inertial reference frame*, indicated by n, to the *body-fixed reference frame*, indicated by b. $\boldsymbol{A_{LVLH}}$, is actually a rotation with respect to the *inertial frame* and can be also indicated as $(\cdot)_{l/n}$. As a result the following matrix multiplication can generate a rotation from the *LVLH frame* to *body-fixed reference frame*, $\boldsymbol{A_{b/l}}$:

$$\boldsymbol{A_{b/l}} = \boldsymbol{A_{b/n}} \boldsymbol{A_{l/n}^T} \tag{2.1}$$

where $(\cdot)^T$ is the transpose of the matrix. Eq. (2.2) represents the transformation of a vector from the *Inertial reference frame* to the *body-fixed reference frame* and can be generalized to any kind of change of bases.

$$\boldsymbol{a_b} = \boldsymbol{A_{b/n}} \boldsymbol{a_n} \tag{2.2}$$

The attitude was implemented exploiting the quaternion formulation, 4-dimensional numbers representing a single rotation in 3D space. This is due to the *Euler's rotation theorem* [21] which states that any single rotation can be represented by a vector, $\hat{\boldsymbol{e}}$, (eigenvector) that remains fixed during that rotation and a simple rotation around that vector by an angle, θ (eigenangle). The four components of

a quaternion are reported in Eq. (2.3) and shall satisfy the constrain equation 2.4.

$$\begin{cases} q_1 = e_1 sin\frac{\theta}{2} \\ q_2 = e_2 sin\frac{\theta}{2} \\ q_3 = e_3 sin\frac{\theta}{2} \\ q_4 = cos\frac{\theta}{2} \end{cases} \tag{2.3}$$

$$q_1^2 + q_2^2 + q_3^2 + q_4^2 = 1 \tag{2.4}$$

Other kind of implementations are: *direct cosine matrices*, *Euler angles* and *Rodrigues vectors*, [22]. The reasons why it was decided to use quaternions instead of the other kind of representation are the following:

- Only 4 parameters are needed to be integrated. This is a good trade-off between the *direct cosine matrices* (9) and the *Euler angles/Rodrigues vectors* (3).

- They are globally defined, meaning that no singularities are present. Singularities affect both the *Euler angles* and the *Rodrigues vector formulation.*

The disadvantages are the fact that they are not unique, meaning that more than one quaternion can indicate the same rotation, they need a quaternion normalisation at each integration step and they are not intuitive.

The attitude matrices are direction cosine matrices indicated with $\boldsymbol{A}$ and they will be transformed in quaternion, $\boldsymbol{q}$, using the following relations:

$$\boldsymbol{A_{b/n}(q)} = \begin{bmatrix} q_1^2 - q_2^2 - q_3^2 + q_4^2 & 2(q_1q_2 + q_3q_4) & 2(q_1q_3 - q_2q_4) \\ 2(q_1q_2 - q_3q_4) & -q_1^2 + q_2^2 - q_3^2 + q_4^2 & 2(q_2q_3 + q_1q_4) \\ 2(q_1q_3 + q_2q_4) & 2(q_2q_3 - q_1q_4) & -q_1^2 - q_2^2 + q_3^2 + q_4^4 \end{bmatrix} \tag{2.5}$$

One of the possible inverse transformations from direction cosine matrices to quaternions is reported from Eq. (2.6) to Eq. (2.9), while the other ones can

be found in Appendix C.

$$q_1 = \frac{1}{4q_4}(A_{23} - A_{32}) \tag{2.6}$$

$$q_2 = \frac{1}{4q_4}(A_{31} - A_{13}) \tag{2.7}$$

$$q_3 = \frac{1}{4q_4}(A_{12} - A_{21}) \tag{2.8}$$

$$q_4 = \pm\frac{1}{2}\sqrt{1 + A_{11} + A_{22} + A_{33}} \tag{2.9}$$

Finally, the cross product between two 3-dimensional vectors will be also performed through the skew-symmetric operator, $S(\cdot)$, defined in [23] as following:

$$\boldsymbol{a} \times \boldsymbol{b} = \boldsymbol{S(a)b} = \begin{bmatrix} 0 & -a_3 & a_2 \\ a_3 & 0 & -a_1 \\ -a_2 & a_1 & 0 \end{bmatrix} \boldsymbol{b} \tag{2.10}$$

2.2 Choice of the software

One of the most used softwares for system control design is Simulink^{TM}, but it is not the best option when more complex systems have to be coded and optimisations algorithms have to be run in parallel. As a result, it was decided to use Matlab^{TM}. The only exception is the de-tumbling phase, for which it was used a Simulink^{TM} model, as it will be explained in Section 5.1.

2.3 The Attitude Determination and Control Subsystem

The ADCS has the aim to control the spacecraft attitude, providing the requested control torque to perform each mission phase, and determine its attitude and angular velocity (part of the state), in order to close the feedback loop shown in Figure 2.2.

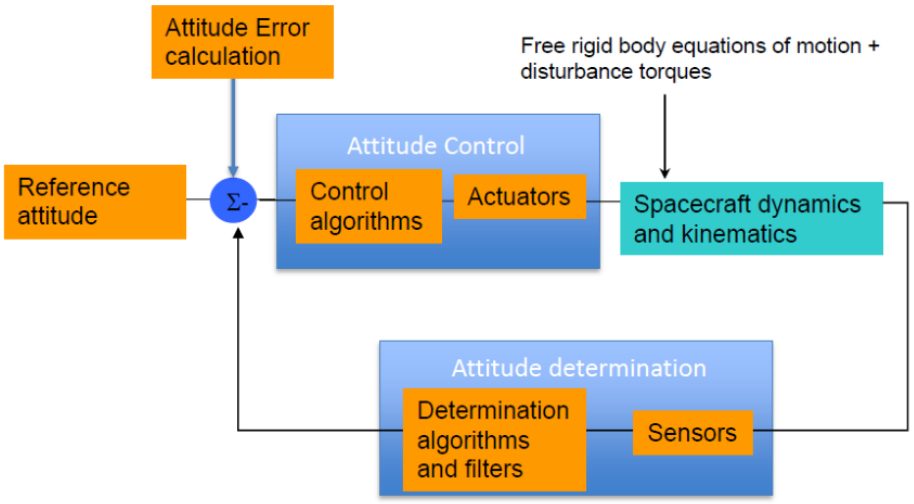

Figure 2.2: *ADCS feedback loop.*

Generally an ADCS simulator is composed by:

- Spacecraft dynamics and kinematics model.
- Control algorithm.
- Actuators models.
- Sensors models.
- Attitude determination algorithms.
- Target attitude.
- External and internal disturbances models.
- Orbital model or ephemeris of the spacecraft.

The following sections describe each element of the loop and the logic behind their implementations.

2.4 Dynamics

The dynamics is modeled using Euler equations:

$$\begin{cases} \dot{\omega}_1 = \frac{I_2 - I_3}{I_1}\omega_2\omega_3 + \frac{u_1 + d_1}{I_1} \\ \dot{\omega}_2 = \frac{I_3 - I_1}{I_2}\omega_1\omega_3 + \frac{u_2 + d_2}{I_2} \\ \dot{\omega}_3 = \frac{I_1 - I_2}{I_3}\omega_2\omega_1 + \frac{u_3 + d_3}{I_3} \end{cases} \tag{2.11}$$

where I_i are the inertias of the spacecraft in the three principal axes, u_i the components of torque control vector and d_i the components of the disturbance torques. From the angular velocities, ω_i, the 4 components of the quaternion representing the attitude of the spacecraft are obtained integrating:

$$\dot{\boldsymbol{q}} = \frac{1}{2}\begin{bmatrix} 0 & \omega_3 & -\omega_2 & \omega_1 \\ -\omega_3 & 0 & \omega_1 & \omega_2 \\ \omega_2 & -\omega_1 & 0 & \omega_3 \\ -\omega_1 & -\omega_2 & -\omega_3 & 0 \end{bmatrix} \boldsymbol{q} \tag{2.12}$$

The initial velocities in rad/s depend on the mission phase. Once the Euler equations have been integrated, the angular velocities in body frame, $\boldsymbol{\omega_{b/n}}$, are obtained and used to integrate the quaternion, which will be then transformed in the body-fixed frame representing the actual attitude, $\boldsymbol{A_{b/n}}$, as described in Section 2.1.

2.5 Orbital model and ephemeris generation

The simulator presented in this Thesis was firstly implemented as decoupled from the orbital dynamics and then improved to model and simulate also the effects of the coupling forces: solar radiation pressure, drag and lift.
In order to obtain the spacecraft ephemeris, an orbital propagator was implemented in Matlab^{TM}. It is based on the restricted 2-body problem perturbed equation:

$$\frac{d^2\mathbf{r}}{dt} = -\frac{\mu}{r^3}\mathbf{r} + \mathbf{p} \tag{2.13}$$

where $\mathbf{r}$ is the position vector, μ the Earth planetary constant and $\mathbf{p}$ the perturbation acceleration,considering the spacecraft as a point mass with the maximum cross-area. This last vector is obtained considering the perturbations induced by:

- The Earth zonal harmonics.

- The Sun and Moon third body perturbations.
- Solar radiation pressure.
- Atmospheric drag.

The ephemeris and the osculating orbital elements are obtained exploiting the Gauss planetary equations [20], Eqs. (2.14) to 2.19, once the initial conditions and $\mathbf{p}$ are provided.

$$\dot{h}_m = r p_s \tag{2.14}$$

$$\dot{e} = \frac{h}{\mu} sin\theta p_r + \frac{1}{\mu h}[(h^2 + \mu r)cos\theta + \mu e r]p_s \tag{2.15}$$

$$\dot{\theta} = \frac{h}{r^2} + \frac{1}{eh}[\frac{h^2}{\mu} cos\theta p_r - (r + \frac{h^2}{\mu})sin\theta p_s] \tag{2.16}$$

$$\dot{\Omega} = \frac{r}{h sin\, i} sin(\omega + \theta) p_w \tag{2.17}$$

$$\dot{i} = \frac{r}{h} cos(\omega + \theta) p_w \tag{2.18}$$

$$\dot{\omega} = -\frac{1}{eh}[\frac{h^2}{\mu} cos\theta p_r - (r + \frac{h^2}{\mu})sin\theta p_s] - \frac{r sin(\omega + \theta)}{h tan\, i} p_w \tag{2.19}$$

where:

- $r = \frac{h^2}{\mu(1+ecos\theta)}$
- h_m: Angular momentum.
- e: Eccentricity.
- Ω: Right ascension of the ascending node.
- i: Orbit inclination.
- ω: Anomaly of the perigee.
- θ: True anomaly.

The decoupled orbit propagator, based on Eqs. (2.14) to 2.19 was implemented using Matlab^{TM}classes. To exploit this set of equations, the vector $\boldsymbol{p}$ must be decomposed along the non-inertial LVLH frame. Then the model exploits *spline* interpolation of the spacecraft ephemeris and the Sun-satellite vector computed before the simulation. The *Spline* interpolation was preferred to the *linear* one, since it avoids discontinuities in interpolated vectors, which would affect strongly the numerical integration. In the orbital model the following quantities are evaluated through interpolation: position, velocity and Sun-satellite vectors. Then the

angular momentum vector is evaluated through:

$$\boldsymbol{h_m} = \boldsymbol{r} \times \boldsymbol{v} \tag{2.20}$$

After having obtained this quantities, the target body-fixed frames are evaluated depending on the mission phase. These matrices represent the desired attitude and will be discussed in Chapter 5. Each raw of these matrices is a desired direction of the body-fixed frame and they are indicated as $\boldsymbol{A_t}$.

2.6 Orbital perturbative accelerations

In this section each perturbative acceleration formulation will be described.

2.6.1 Earth zonal harmonics perturbative acceleration

The Earth oblateness effect is modeled as perturbative acceleration, $\boldsymbol{p}$, evaluated as

$$\boldsymbol{p_{obl}} = -\boldsymbol{\nabla}\Phi \tag{2.21}$$

where, Φ is the perturbation of the gravitational potential due to the planet's oblateness, function of the satellite distance, r, and the polar angle measured from the positive z-axis to the radial, ψ [20]:

$$\Phi(r,\psi) = \frac{\mu}{r}\sum_{k=2}^{\infty} J_k \left(\frac{R}{r}\right)^k P_k(cos\psi) \tag{2.22}$$

with

$$\psi = tan^{-1}\frac{\sqrt{x^2+y^2}}{z} \tag{2.23}$$

where x, y and z are written in the Earth centred fixed reference frame. J_k are the *zonal harmonics* of the planet, R is its equatorial radius ($R/r < 1$), and P_k are the Legendre polynomials. The zonal harmonics are dimensionless numbers that are not derived from mathematics but are inferred from observations of satellite motion around a planet, and they are unique to that planet [20]. The polynomial $P_k(x)$ may be obtained by the Rodrigues formula's, [20]:

$$P_k(x) = \frac{1}{2^k k!}\frac{d}{dx^k}(x^2-1)^k \tag{2.24}$$

The complete formulation of the acceleration $\boldsymbol{p_{obl}}$ till the 7^{th} order, can be found in [20].

2.6.2 Sun and Moon third body perturbations

The Sun and Moon third body perturbation are modeled under the assumption of the restricted circular three body problem, adding to Eq. (2.13), the perturbative acceleration [20]:

$$\boldsymbol{p}_{\text{RC3BP}} = \mu_2 \left(\frac{\boldsymbol{r_{21}}}{r_{21}^3} - \frac{\boldsymbol{r_2}}{r_2^3} \right) \tag{2.25}$$

where $\boldsymbol{r_2}$ and r_2 are respectively the second body (Moon or Sun) position vector and the distance from the center of the main attractor, the Earth, while $\boldsymbol{r_{21}}$ and r_{21} are respectively the second body position vector and the distance from the spacecraft.

2.6.3 Solar radiation pressure perturbative acceleration

The solar radiation pressure perturbative acceleration is evaluated exploiting the cannonball model, reported in [20]:

$$\boldsymbol{p_{SRP}} = -\frac{P_{SR}}{m} C_r A_s \hat{\boldsymbol{S}} \tag{2.26}$$

where:

- P_{SR} is the solar radiation pressure at 1 Astronomic Unit (AU), whose value is 4.56×10^{-6} N/m^2 (4.56 μPa).
- m is the mass of the spacecraft.
- C_r is the reflective coefficient, whose value spans between 1 (black body) and 2 (ideal reflector) for a flat surface, while it is always 1 for a sphere, [24].
- A_s is the cross surface exposed to the solar radiation.
- $\hat{\boldsymbol{S}}$ is the satellite-Sun unit vector.

2.6.4 Atmospheric drag perturbative acceleration

The model for atmospheric drag acceleration formulation can be found in [20] as well and it is mainly dependent on the satellite surfaces exposed to the incoming air flux. To analyse the worst case scenario, the maximum cross-sectional area was considered for both the OUFTI-Next and the ZodiArt missions.

$$\boldsymbol{p_{drag}} = -\frac{1}{2}\rho(h)C_d\frac{A_d}{m}\boldsymbol{v_{rel}}||\boldsymbol{v_{rel}}|| \tag{2.27}$$

where:

- $\rho(h)$ is the atmospheric density model, dependent on the altitude h.
- C_d is the drag coefficient.
- A_d is the platform cross surface exposed to the relative wind.
- $\boldsymbol{v_{rel}}$ is the wind relative velocity, obtained as vectorial difference between the spacecraft velocity and the atmospheric velocity vector, $\boldsymbol{v_{atm}}$, both in the *Inertial reference system*:

$$\boldsymbol{v_{atm}} = \begin{bmatrix} 0 \\ 0 \\ \omega_\oplus \end{bmatrix} \times \boldsymbol{r} \tag{2.28}$$

$$\boldsymbol{v_{rel}} = \boldsymbol{v} - \boldsymbol{v_{atm}} \tag{2.29}$$

  where $\omega_\oplus$ is the Earth angular velocity: 0.000072921 rad/sec.

The model used for atmospheric density is a simple exponential model, [25]:

$$\rho = \rho_0 exp\left[-\frac{h-h_0}{H}\right] \tag{2.30}$$

where:

- ρ_0 is reference density.
- h_0 is the reference altitude.
- H is the scale height

H varies from 7.25 km at the Earth's surface to 268 km at 1000 km altitude and it is the altitude over which the density changes by the Euler's number e ($e = 2.72$). The reference density varies from 1.225 kg/m^3 at the surface to 3.019×10^{-15} kg/m^3 at 1000 km altitude [25]. The source for the previous parameters, depending on the

height, is [26], which uses the *U.S. Standard Atmosphere* (1976) for 0 km, CIRA-72 for $25 - 500$ km and CIRA-72 with exospheric temperature $T_{\text{inf}} = 1000$ K for $500 - 1000$ km. The scale heights were adjusted to maintain a piecewise-continuous formulation of the density.

2.6.5 Atmospheric lift perturbative acceleration

According to the aerodynamics theory, a profile moving inside a flow experiences a drag force in the direction of relative wind and a lift force in the orthogonal direction:

$$\frac{\boldsymbol{v_{rel}} \times (\boldsymbol{v_{rel}} \times \boldsymbol{n})}{||\boldsymbol{v_{rel}} \times (\boldsymbol{v_{rel}} \times \boldsymbol{n})||}$$

where $\boldsymbol{n}$ is the normal to the surface exposed to the relative wind, as reported in [6]. An exhaustive description of the effects of lift on near circular orbits, for small spacecrafts can be found in [27]. The lift perturbative acceleration was modeled as follow [28]:

$$\boldsymbol{p_{lift}} = \frac{1}{2}\rho(h) C_l \frac{A_d}{m} \frac{\boldsymbol{v_{rel}} \times (\boldsymbol{v_{rel}} \times \boldsymbol{n})}{||\boldsymbol{v_{rel}} \times (\boldsymbol{v_{rel}} \times \boldsymbol{n})||} ||\boldsymbol{v_{rel}}||^2 \tag{2.31}$$

where C_l is the lift coefficient and α is the spacecraft angle of attack.

2.7 Attitude disturbances model

The attitude disturbances are torque vectors, $\boldsymbol{d}$, that will be inserted in the 3D rigid body dynamics of the spacecraft, Eq. (2.11). In this section the four main sources of disturbance will be analysed in detail.

2.7.1 Atmospheric drag torque

The atmospheric drag force was modeled using Eq. (2.27) and multiplying it times the spacecraft mass:

$$\boldsymbol{F_{drag}} = -\frac{1}{2}\rho(h) C_d A_d v_{rel}^2 \frac{\boldsymbol{v_{rel}}}{||\boldsymbol{v_{rel}}||} \tag{2.32}$$

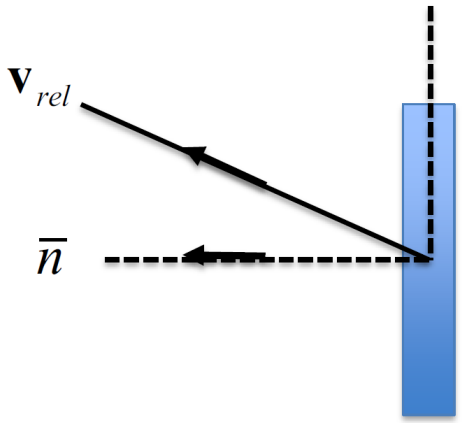

Figure 2.3: *Spacecraft surface with respect to relative velocity.*

To obtain the overall torque vector acting on the spacecraft, the force vector is multiplied by the vector connecting the centre of mass and the assumed centre of pressure, $\boldsymbol{r_{cp}}$. Since its position is uncertain or dependent on time, a 10% error is considered. Obviously, if the product between the surface's normal and the relative velocity is less than 0, the resulting torque is null. In index form:

$$\boldsymbol{T_{drag}} = \begin{cases} -\frac{1}{2}\rho(h)C_d v_{rel}^2 \frac{\boldsymbol{v_{rel}}}{||\boldsymbol{v_{rel}}||} \sum_{i=1}^{N} \boldsymbol{r_{cp,i}} \times (\boldsymbol{n_i} \cdot \frac{\boldsymbol{v_{rel}}}{||\boldsymbol{v_{rel}}||}) A_i & (\boldsymbol{n_i} \cdot \frac{\boldsymbol{v_{rel}}}{||\boldsymbol{v_{rel}}||}) > 0 \\ \mathbf{0} & (\boldsymbol{n_i} \cdot \frac{\boldsymbol{v_{rel}}}{||\boldsymbol{v_{rel}}||}) < 0 \end{cases} \tag{2.33}$$

where N is the spacecraft number of surfaces.

2.7.2 Solar radiation pressure torque

To model the torque induced by the solar radiation torque, the cannonball model reported in Eq. (2.26) can not be exploited, because it is based the assumption that the spacecraft can be approximated to a sphere. According to this assumption, the spacecraft attitude would be the same in all the directions. As a consequence, the solar radiation pressure force was modeled using the flat plate approximation, [29]:

$$\boldsymbol{F_{SRP}} = P_{SR}\boldsymbol{A_s}\Big[\rho_a(\hat{\boldsymbol{S}} \cdot \boldsymbol{n}) + 2\rho_s(\hat{\boldsymbol{S}} \cdot \boldsymbol{n})^2 \cdot \boldsymbol{n} + \frac{2}{3}\rho_d(\hat{\boldsymbol{S}} \cdot \boldsymbol{n})\Big] \tag{2.34}$$

where:

- $\hat{\boldsymbol{S}}$ is the unit vector pointing from the Sun to the surface as shown in Figure 2.4.
- $\boldsymbol{n}$ is the surface normal vector.
- ρ_a is the surface absorption coefficient.
- ρ_d is the surface diffusive coefficient.
- ρ_s is the surface scattering coefficient.

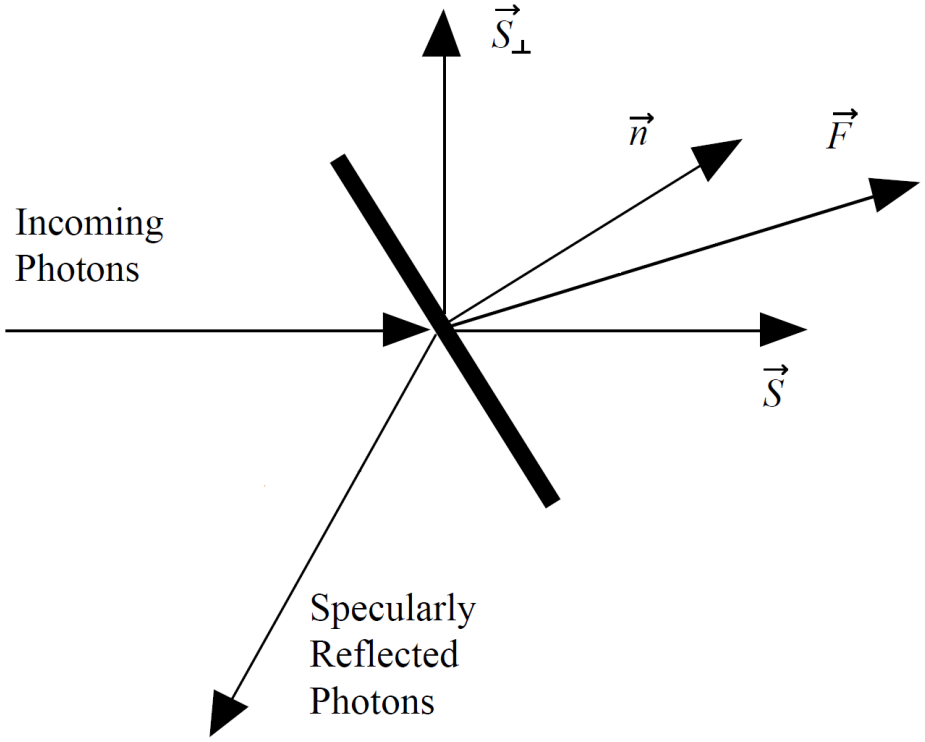

Figure 2.4: *Incoming photons impacting on a flat surface.*

As for the drag, in order to obtain the overall torque, a multiplication times the arm is required and, as before, a 10% error was considered in the position of the centers of pressure, r_{cp} on the platform surfaces:

$$\boldsymbol{T_{SRP}} = \begin{cases} \sum_{i=1}^{N} \boldsymbol{r_{cp,i}} \times \boldsymbol{F_{SRP_i}} & (\hat{\boldsymbol{S}} \cdot \boldsymbol{n_i}) > 0 \\ \boldsymbol{0} & (\hat{\boldsymbol{S}} \cdot \boldsymbol{n_i}) < 0 \end{cases} \tag{2.35}$$

where N is the spacecraft number of surfaces. As we can notice from Eq. (2.35), if the Sun-Earth vector projection on the surface normal is negative, there is no SRP torque.

In order to simulate more precisely this effect, an eclipse model was implemented [25]:

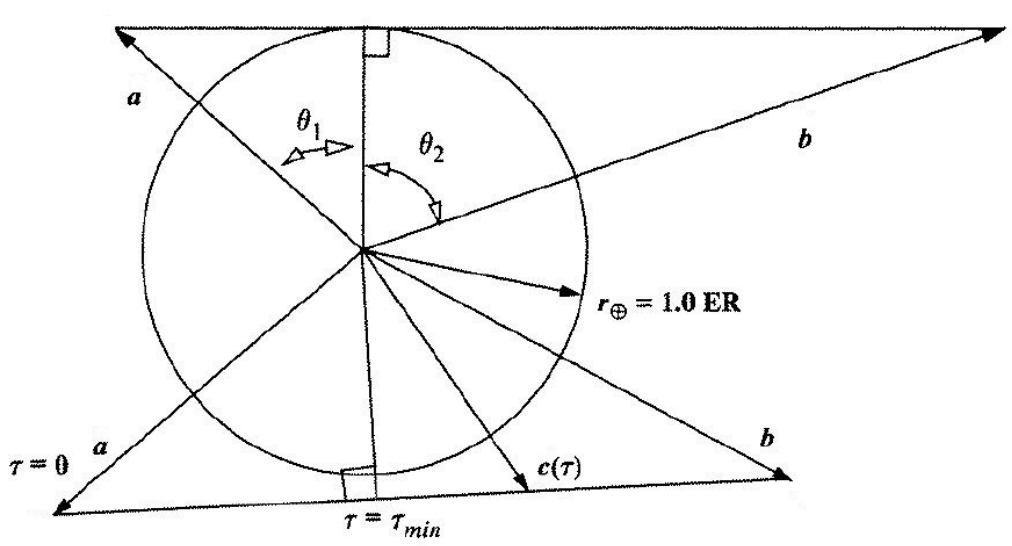

Figure 2.5: *Light-shadow model [25].*

All the vectors are normalized with respect to the Earth radius and $\boldsymbol{a}$ and $\boldsymbol{b}$ represent respectively the Sun vector [25] (assumed mission day-one: January the 1^{st} 2019 at 12:00 GMT+0) and the satellite position vector. $\boldsymbol{c}$, instead, can be obtained as function of τ_{min} as follows:

$$|\boldsymbol{c}(\tau_{min})|^2 = (1 - \tau_{min})|\boldsymbol{a}|^2 + (\boldsymbol{a} \cdot \boldsymbol{b})\tau_{min} \tag{2.36}$$

$$\tau_{min} = \frac{\boldsymbol{a} \cdot (\boldsymbol{a} - \boldsymbol{b})}{|\boldsymbol{a} - \boldsymbol{b}|} \tag{2.37}$$

$\boldsymbol{a}$, $\boldsymbol{b}$ and $\boldsymbol{c}$ symbols are used with this meaning only in this section, in order to be consistent with the notation used in [25].

In this way, once found τ_{min}, if $\tau_{min} < 0$ or $\tau_{min} > 0$, there is line-of-sight between the two vectors. In fact both vectors are in the same quadrant with respect to the attracting body, as shown in Figure 2.5. If τ_{min} assumes a value between 0 and 1, it has to be substituted into Eq. (2.36) to determine the square of the magnitude at the minimum location. If this squared magnitude is equal or larger than 1, line-of-sight exists. In all remaining cases, it does not [25].

2.7.3 Geomagnetic field

The Earth magnetic field is modeled with the Matlab^{TM} build-in function *wrldmagm.m*, [30], which evaluates the Earth magnetic field components in the years between 2015 and 2020, requiring as inputs:

- The orbit height in meters.
- A scalar geodetic latitude, in degrees, where north latitude is positive, and south latitude is negative.
- A scalar geodetic longitude, in degrees, where east longitude is positive, and west longitude is negative.
- A scalar decimal year. Decimal year is the desired year in a decimal format to include any fraction of the year that has already passed.

The function output, once obtained in *inertial reference frame*, is then transformed in body-frame coordinates through:

$$\boldsymbol{B_b} = \boldsymbol{A_{b/n}} \boldsymbol{B_n} \tag{2.38}$$

Finally the magnetic torque can be computed, considering as satellite internal induction, $\boldsymbol{m}$:

$$\boldsymbol{T_{magnetic}} = \boldsymbol{m} \times \boldsymbol{B_b} \tag{2.39}$$

It is important to underline the limitations of this model, as reported in [30]: "The World Magnetic Model (WMM) specification produces data that is reliable five years after the epoch of the model, which begins January 1 of the model year selected. The WMM specification describes only the long-wavelength spatial magnetic fluctuations due to the Earth's core. Intermediate and short-wavelength fluctuations, contributed from the crustal field (the mantle and crust), are not included. Also, the substantial fluctuations of the geomagnetic field, which occur constantly during magnetic storms and almost constantly in the disturbance field (auroral zones), are not included."
To reduce the computational time of de-tumbling phase, an approximated Earth magnetic field model, based on the Schmidt quasi-normalised associated Legendre Polynomial [31] was implemented and it will be described in the section dedicated to de-tumbling phase.

2.7.4 Gravity gradient torque

The gravitational disturbance is modeled as follows:

$$\boldsymbol{T_{gravity}} = \frac{3\mu}{r^5} \int_M (\boldsymbol{r_b} \cdot \boldsymbol{r})(\boldsymbol{r_b} \times \boldsymbol{r}) dm \tag{2.40}$$

where M is the spacecraft total mass, $\boldsymbol{r}$ is the satellite position vector and $\boldsymbol{r_b}$ is the vector connecting its center of mass to the infinitesimal cube of mass dm. In order to get an easier expression, the torque can be rearranged in this way:

$$\boldsymbol{T_{gravity}} = \int_M \begin{bmatrix} (y^2 - z^2)c_2c_3 \\ (z^2 - x^2)c_1c_3 \\ (x^2 - y^2)c_1c_2 \end{bmatrix} dm = \frac{3\mu}{R^3} \begin{bmatrix} (I_3 - I_2)c_2c_3 \\ (I_1 - I_3)c_1c_3 \\ (I_2 - I_1)c_1c_2 \end{bmatrix} \tag{2.41}$$

where c_i are three parameters defined as:

$$\begin{bmatrix} c_1 \\ c_2 \\ c_3 \end{bmatrix} = nadir\ direction = - \begin{bmatrix} \hat{r}_x \\ \hat{r}_y \\ \hat{r}_z \end{bmatrix} \tag{2.42}$$

with $\hat{\boldsymbol{r}}$ the normalised position vector.

2.8 Sensors and attitude determination

The aim of the *sensors and attitude determination* block in the ADCS feedback-loop, Figure 2.6, is to introduce noises and measurement errors inside the integrated states, in order to simulate the sensors accuracy effect on the system and then reconstruct the state, thanks to the attitude determination algorithm. First of all, the models of sensors had been implemented and then two different attitude determination strategies were adopted.

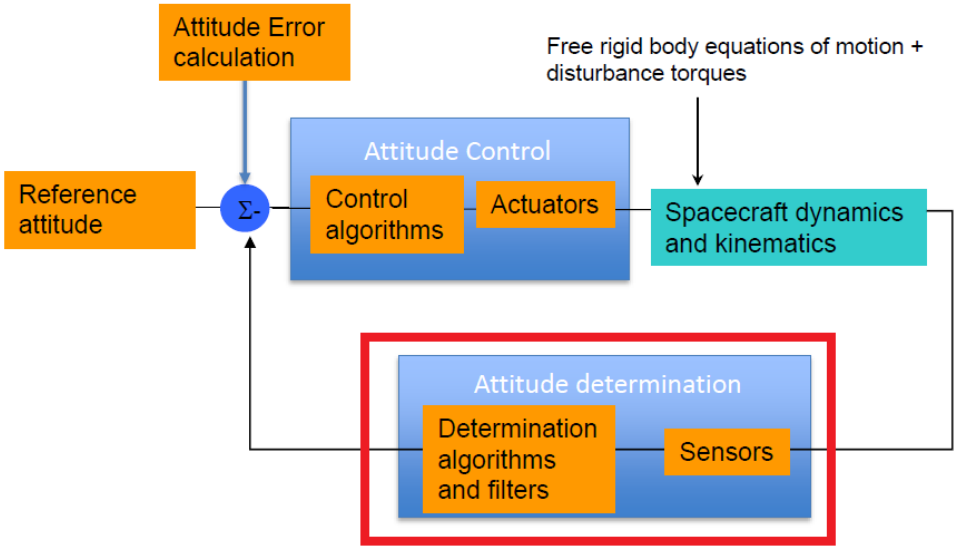

Figure 2.6: *ADCS feedback loop with* sensors and attitude determination *block highlighted.*

It is important to remark, that no white noises nor sensors update frequencies were inserted in the final simulation, since they slow down the simulations too much. Indeed, they badly affect the computational time, since the mission profiles to be simulated are characterised by long time intervals to be integrated. During the work, the presence of noises and update rates, was implemented on simplified and shorter simulations, providing positive results in terms of accuracy of the determination even in presence of this kind of effects. In Chapter 6 the simulation of the final and complete models for short time intervals will be provided, considering also this sources of measurements errors to show the effects on the determination. In this section the models of the main sensors (star tracker and gyroscopes) are described, as well as the determination algorithms used.

2.8.1 Gyroscopes

To model the gyroscopes, the angular velocities in body fixed frame, $\boldsymbol{\omega_{b/n}}$, should be perturbed by a dynamic Gaussian noise and the accuracy matrix presented in Eq. (2.43), where the argument of trigonometric functions are the accuracy on each axis, $\hat{\theta}$, $\hat{\phi}$, $\hat{\psi}$, [32].

$$\boldsymbol{A_\epsilon} = \begin{bmatrix} cos(\hat{\psi})cos(\hat{\theta}) & cos(\hat{\psi})sin(\hat{\theta})sin(\hat{\phi}) + sin(\hat{\psi})cos(\hat{\phi}) & -cos(\hat{\psi})sin(\hat{\theta})cos(\hat{phi}) + sin(\hat{\psi})sin(\hat{\phi}) \\ -sin(\hat{\psi})cos(\hat{\theta}) & -sin(\hat{\psi})sin(\hat{\theta})sin(\hat{\psi}) + cos(\hat{\psi})cos(\hat{\theta}) & sin(\hat{\psi})sin(\hat{\theta})cos(\hat{\psi}) + cos(\hat{\psi})sin(\hat{\theta}) \\ sin(\hat{\theta}) & -cos(\hat{\theta})sin(\hat{\phi}) & cos(\hat{\theta})cos(\hat{\phi}) \end{bmatrix} \tag{2.43}$$

$$\boldsymbol{\omega_{b/n,real}} = \boldsymbol{A_\epsilon A_{b/n} w_{b/n}} + \boldsymbol{noise} \tag{2.44}$$

where the $\boldsymbol{noise}$ is evaluated as the sum of the measurement noise $\boldsymbol{n_e}$, and the drift rate ramp $\boldsymbol{n_u}$, defined in [32] as:

$$\begin{cases} \boldsymbol{n_e} = \boldsymbol{\sigma_\epsilon} \zeta_e \\ \boldsymbol{n_u} = \boldsymbol{n_u}(t - \delta t) + \boldsymbol{\sigma_u} \sqrt{\delta t} \zeta_u \end{cases} \tag{2.45}$$

with:

- ζ_e and ζ_u are normally distributed random variables with 0 mean value and standard deviation 1.
- $\boldsymbol{\sigma}$ is the standard deviation of the measurements.
- δt is the sampling time.

2.8.2 Star tracker

The star tracker is a sensor capable to obtain directly the attitude of the satellite, the matrix $\boldsymbol{A_{b/n}}$, through an algebric attitude determination law, that will be presented in Subection 2.8.5. In order to model its output, $\boldsymbol{A_{b/n}}$, shall be perturbed by the accuracy matrix presented in Eq. (2.43), $\boldsymbol{A_\epsilon}$, where the argument of trigonometric functions are the accuracies on each axis, and then, once transformed in quaternion, a random Gaussian noise shall be added.

$$\boldsymbol{A_{b/n,real}} = \boldsymbol{A_\epsilon A_{b/n}} \tag{2.46}$$

$$\boldsymbol{q_{real}} = \boldsymbol{q} + \boldsymbol{noise} \tag{2.47}$$

2.8.3 Kalman filter

The Kalman filter is an algorithm capable of obtaining an estimation of the state, with the additional knowledge of the covariance matrix of the state error, $\boldsymbol{P}$, representing the deviation with respect to the actual state, starting from noisy measurements. It is the best way to estimate the state starting from measurements subjected to Gaussian noise with 0 mean value, like the ones provided by spacecrafts' sensors and at the same time have an estimation of the determination error, through $\boldsymbol{P}$. In this paragraph a short theoretical description is provided, based on [33].

As shown in Figure 2.7 the filter assumes that the state variables, position and velocity, are random and with a Gaussian distribution. The variances in position and velocity are identified with σ_p^2 and σ_v^2 respectively.

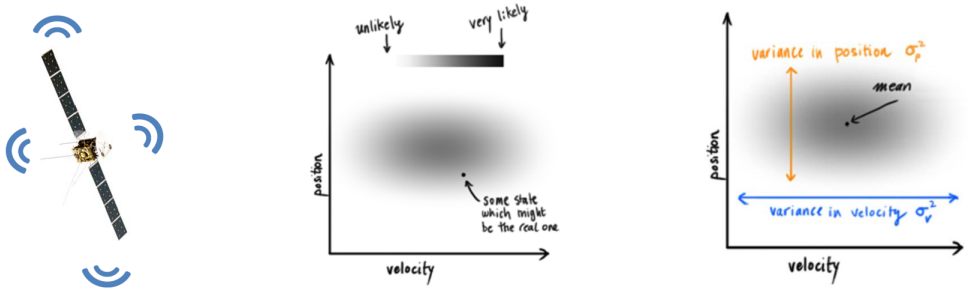

Figure 2.7: *Kalman filter and the random state with Gaussian distribution, [33].*

Then looking at the current state, $\boldsymbol{x_{k-1}}$, it predicts the next state, $\boldsymbol{x_k}$, according to the dynamical model, $\boldsymbol{F_k}$. In a similar fashion it is possible to obtain also the predicted covariance matrix, $\boldsymbol{P_{k-1}}$, as shown in Figure 2.8 and reported in Eqs. (2.48)–(2.49).

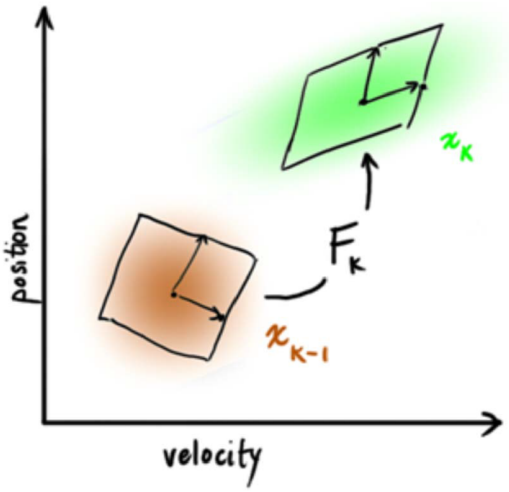

Figure 2.8: *State and covariance matrix prediction, [33].*

$$\boldsymbol{x_k} = \boldsymbol{F_k x_{k-1}} \tag{2.48}$$

$$\boldsymbol{P_k} = \boldsymbol{F_k P_{k-1} F_k^T} \tag{2.49}$$

In order to be robust against some unmodelled dynamics or external disturbances, an additional uncertainty, $\boldsymbol{Q_k}$, is applied to the predicted covariance matrix, as

shown in Figure 2.9 and detailed in Eq. (2.50).

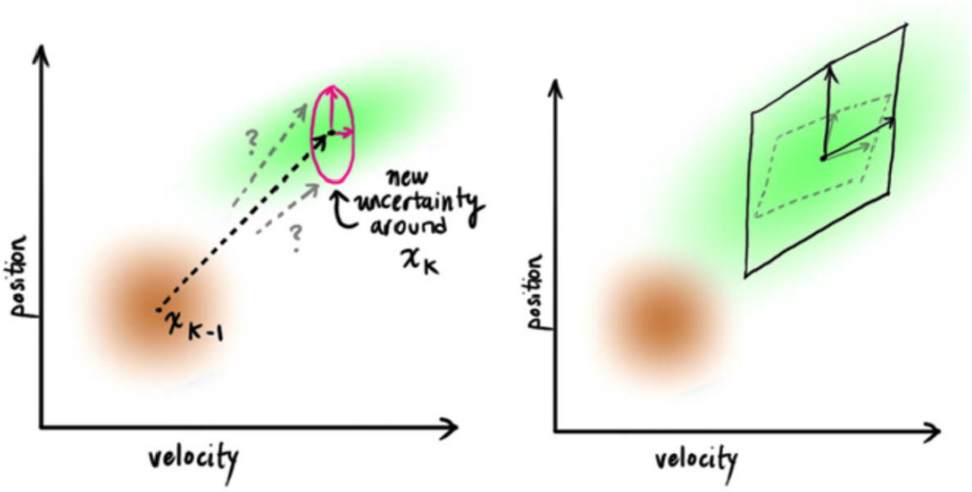

Figure 2.9: *Additional uncertainty addition to predicted covariance, [33].*

$$\boldsymbol{P_k} = \boldsymbol{F_k P_{k-1} F_k^T} + \boldsymbol{Q_k} \tag{2.50}$$

The predicted value has to be refined with measurements from sensors, Figure 2.10. As for the state, it is possible to obtain the expected measurements, $\hat{\boldsymbol{\mu}}_{\boldsymbol{expected}}$, and their covariance matrix, $\boldsymbol{\Sigma_{expected}}$, from the current state and through the measurement model, $\boldsymbol{H_k}$, Eqs. (2.51)–(2.52).

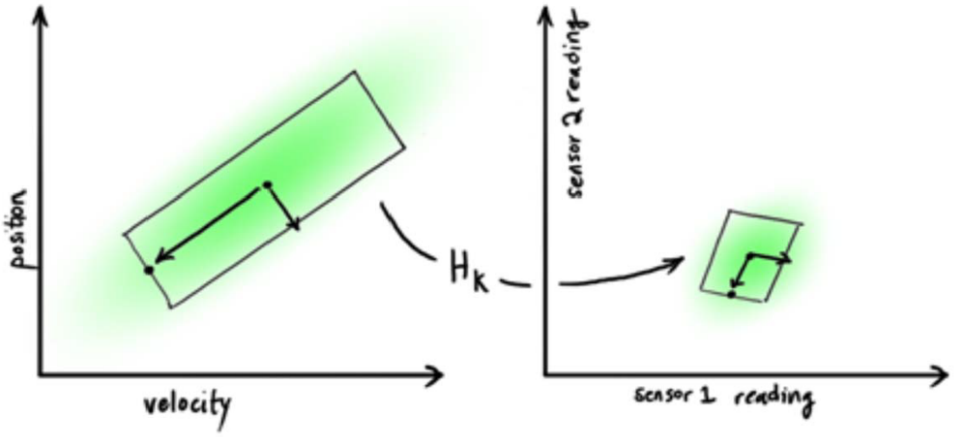

Figure 2.10: *Measurements and their covariance matrix prediction, [33].*

$$\hat{\boldsymbol{\mu}}_{\boldsymbol{expected}} = \boldsymbol{H_k x_k} \tag{2.51}$$

$$\boldsymbol{\Sigma_{expected}} = \boldsymbol{H_k P_k H_k^T} \tag{2.52}$$

Sensors instead produce given measurements $\boldsymbol{z_k}$ with an associate uncertainty, $\boldsymbol{R_k}$. Multiplying the estimated state obtained through the measurement model and the obtained measurements together with their Gaussian distributions, it is possible to obtain the Kalman update factor, $\boldsymbol{z_k - H_k \hat{x}_k}$, providing a correction to the predicted variables previously obtained, Figure 2.11.

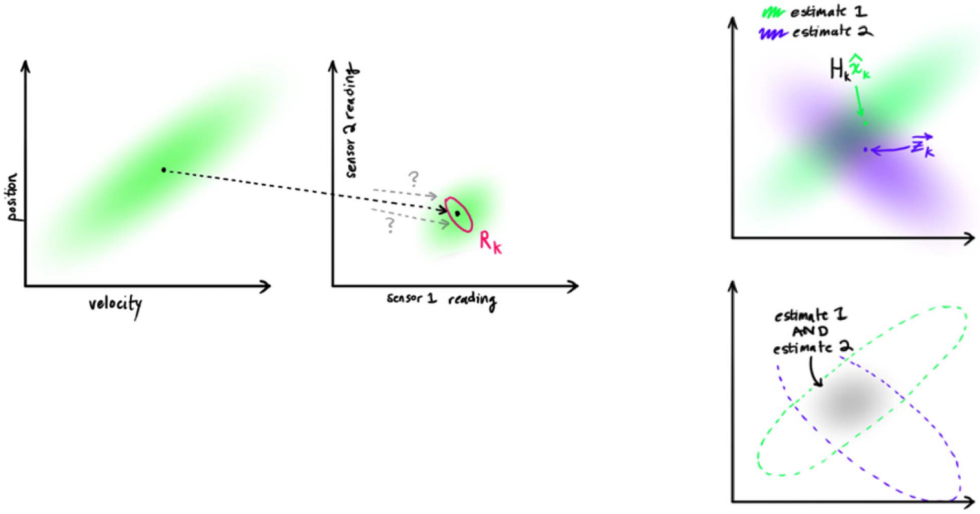

Figure 2.11: *Update factor evaluation, [33].*

Finally, the complete formulation is here reported:

$$\boldsymbol{x_k = F_k x_{k-1}} \tag{2.53}$$

$$\boldsymbol{P_k = F_k P_{k-1} F_k^T} \tag{2.54}$$

$$\boldsymbol{x'_k = x_k + K(z_k - H_k x_k)} \tag{2.55}$$

$$\boldsymbol{P'_k = P_k - K H_k P_k} \tag{2.56}$$

$$\boldsymbol{K = P_k H_k^T (H_k P_k H_k^T + R_k)^{-1}} \tag{2.57}$$

where $(\cdot)'$ indicates the variable estimated by the filter.
There are three main kinds of Kalman filters:

- *Linear Kalman filter*, as the one presented in the previous paragraph.
- *Extended Kalman filter* (EKF), used for non linear models and based on their linearisation.

- *Unscented Kalman filter* (UKF), used for non linear models.

The *extended kalman filter* has a similar formulation with respect to the linear one, [33]:

$$\boldsymbol{x_k} = \boldsymbol{f_k}(\boldsymbol{x_{k-1}}) \tag{2.58}$$

$$\boldsymbol{P_k} = \boldsymbol{F_k}\boldsymbol{P_{k-1}}\boldsymbol{F_k^T} + \boldsymbol{Q_k} \tag{2.59}$$

$$\boldsymbol{x'_k} = \boldsymbol{x_k} + \boldsymbol{K'}(\boldsymbol{z_k} - \boldsymbol{h_k}(\boldsymbol{x_k})) \tag{2.60}$$

$$\boldsymbol{P'_k} = \boldsymbol{P_k} - \boldsymbol{K'}\boldsymbol{H_k}\boldsymbol{P_k} \tag{2.61}$$

$$\boldsymbol{K'} = \boldsymbol{P_k}\boldsymbol{H_k^T}(\boldsymbol{H_k}\boldsymbol{P_k}\boldsymbol{H_k^T} + \boldsymbol{R_k})^{-1} \tag{2.62}$$

where $\boldsymbol{f_k}$ and $\boldsymbol{h_k}$ are the non linear models of the dynamics and measurements.

In this case $\boldsymbol{F_k}$ and $\boldsymbol{H_k}$ are the Jacobians of the models:

$$\boldsymbol{F_k} = \frac{\partial \boldsymbol{f_k}}{\partial \boldsymbol{x}} \tag{2.63}$$

$$\boldsymbol{H_k} = \frac{\partial \boldsymbol{h_k}}{\partial \boldsymbol{x}} \tag{2.64}$$

The limitation of this kind of filter is that they do not guarantee good accuracy if the system non linearities are severe, because it relies on linearisation for mean and covariance update.

For this reason the filter selected for the ADCS is the *unscented Kalman filter*, which is not based on linearisation.

2.8.4 Unscented Kalman filter

The *unscented kalman filter* is based on *unscented transformations*:

1. Sample points (*sigma points*) are used to approximate the state distribution.
2. They are propagated through the non linear dynamical model.
3. Their propagation can be used to reconstruct the posterior state mean and covariance.

In this kind of filter no Jacobian nor linearisation are required. In Figure 2.12 it is possible to graphically see the differences among the three kinds of Kalman filters.

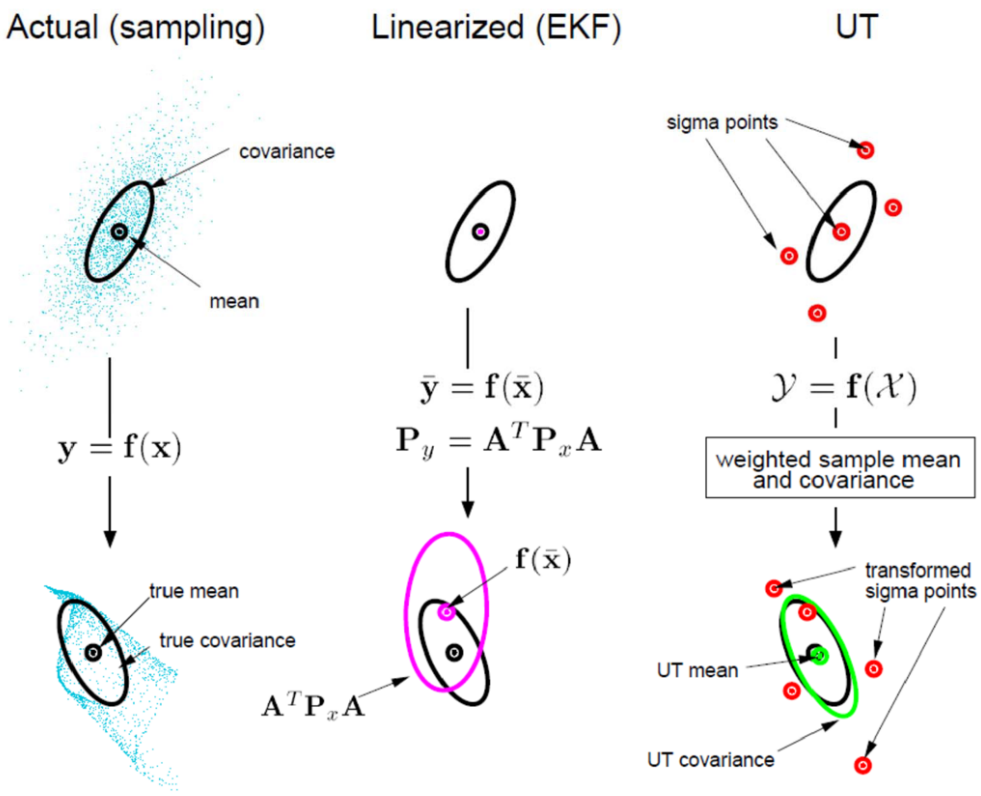

Figure 2.12: *Three main kinds of Kalman filters compared, [34].*

The inputs to the unscented kalman filter are:

- L, the number of states to estimate: 7 (3 angular velocities and 4 quaternion components).
- $\hat{m}$, the number of measurements available: 7 (3 angular velocities and 4 quaternion components).
- $\boldsymbol{f_k}$, the dynamical model.
- $\boldsymbol{h_k}$, the measurement model (it was decided to be just the output of the integration for simplicity).
- q, standard deviation of the process.
- r_m, standard deviation of the measurements.
- $\boldsymbol{P}$, the initial state error covariance matrix, commonly initialised as $\boldsymbol{P} = \boldsymbol{I}$.

$\boldsymbol{Q}$ and $\boldsymbol{R}$ are the covariance matrices respectively of process and measurements (diagonal matrices filled by the square of the standard deviations of the process and measurements). To find the proper value for the standard deviation of the process, some simulations were performed and after having compared the deter-

mination errors, the value selected was 1. Moreover, the covariance matrix of the process, representing the uncertainties on the model (equations), was defined as equal to the identity $\boldsymbol{I}$, also because in this way we are accounting for dynamics not modeled, "smearing" artificially the next-step normal distribution, increasing the uncertainty of the prediction and raising, as a consequence, the probabilities of finding a good estimation of the state vector.
The state and measurements are perturbed with a white noise with 0 mean value and standard deviation defined above, but, as explained before, no noises were implemented for the moment and, as a consequence, they are perturbed by a fixed value corresponding to the standard deviations (worst case).
According to [35], some parameters, useful for the mathematical development of the filter are here reported:

- $k = 0$
- $\hat{\alpha} = \sqrt{3}$
- $\beta = 2$
- $\hat{\lambda} = \alpha^2(L + k) - L$
- $\hat{c} = L + \hat{\lambda}$

At this point, the state *sigma points* are generated around the state, $\boldsymbol{x}$:

$$\boldsymbol{A_c} = \sqrt{\hat{c}}\ chol(\boldsymbol{P})^T \tag{2.65}$$

where "chol" means: Cholesky decomposition.

$$\boldsymbol{X} = \begin{bmatrix} \boldsymbol{x}\boldsymbol{A_c} + \boldsymbol{Y_{ones}} & \boldsymbol{Y_{ones}} - \boldsymbol{A_c} \end{bmatrix} \tag{2.66}$$

where $\boldsymbol{Y_{ones}}$ is an $L \times L$ matrix full of ones and $\boldsymbol{X}$ dimension is $L \times 2L + 1$, containing the 2L+1 *sigma points* of the state.

The state *sigma points*, are then propagated through the dynamical model by an unscented transformation performed on each column $\boldsymbol{Y}(:, k)$ of the*sigma points* matrix $\boldsymbol{Y}$:

$$\boldsymbol{Y}(:, k) = f(\boldsymbol{X}(:, k)) \qquad \text{with } k = 1, 2, ..., 2L + 1 \tag{2.67}$$

To obtain the mean value and the covariance unscented transformations, it is necessary a weighted sampling of the *sigma points*. As a consequence, the weights vectors (of length 2L + 1) are evaluated:

- $W_m = \left[\frac{\hat{\lambda_c}}{\hat{c}}, \left[\frac{0.5}{\hat{c}}, \frac{0.5}{\hat{c}}, ...\right]\right]$
- $W_{\hat{c}} = W_m$
- $W_{\hat{c}(1)} = W_{\hat{c}(1)} + (1 - \alpha^2 + \beta)$

and then exploited to compute the mean value vector, $\boldsymbol{y}$:

$$\boldsymbol{y} = \boldsymbol{W_m}(k)\boldsymbol{Y}(:,k) \qquad \text{with } k = 1, 2, ..., 2L+1 \tag{2.68}$$

providing finally the transformed deviation from the mean value, $\boldsymbol{Y_1}$, subtracting to each column k of $\boldsymbol{Y}$ the vector $\boldsymbol{y}$:

$$\boldsymbol{Y_1} = \boldsymbol{Y}(:,k) - \boldsymbol{y} \qquad \text{with } k = 1, 2, ..., 2L+1 \tag{2.69}$$

and the transformed covariance of the state error, $\boldsymbol{P_1}$:

$$\boldsymbol{P_1} = \boldsymbol{Y_1} \begin{bmatrix} W_{c,1} & 0 & 0 & 0 & ... & 0 \\ 0 & W_{c,2} & 0 & 0 & ... & 0 \\ 0 & 0 & W_{c,3} & 0 & ... & 0 \\ 0 & 0 & 0 & W_{c,4} & ... & 0 \\ ... & ... & ... & ... & ... & 0 \\ 0 & 0 & 0 & 0 & 0 & W_{c,2L+1} \end{bmatrix} \boldsymbol{Y_1}^T + \boldsymbol{R} \tag{2.70}$$

The same procedure must be followed for the measurements unscented transformation.

Then the transformation of the cross-covariance, $\boldsymbol{P_{12}}$ is performed:

$$\boldsymbol{P_{12}} = \boldsymbol{P_{1,s}} \begin{bmatrix} W_{c,1} & 0 & 0 & 0 & ... & 0 \\ 0 & W_{c,2} & 0 & 0 & ... & 0 \\ 0 & 0 & W_{c,3} & 0 & ... & 0 \\ 0 & 0 & 0 & W_{c,4} & ... & 0 \\ ... & ... & ... & ... & ... & 0 \\ 0 & 0 & 0 & 0 & 0 & W_{c,2L+1} \end{bmatrix} \boldsymbol{P_{1,m}}^T \tag{2.71}$$

where $\boldsymbol{P_{1,s}}$ is the covariance of the state transformed and $\boldsymbol{P_{1,m}}$ is the one of the measurements. At this point, the Kalman matrix $\boldsymbol{K}$ can be evaluated:

$$\boldsymbol{K} = \boldsymbol{P_{12}}\boldsymbol{Y_1}^{-1} \tag{2.72}$$

and the state updated, providing the estimated state:

$$\boldsymbol{x'} = \boldsymbol{y} + \boldsymbol{K}(\boldsymbol{z} - \tilde{\boldsymbol{v}}) \tag{2.73}$$

where $\tilde{\boldsymbol{v}}$ is the measurements mean value as $\boldsymbol{y}$ is the mean value of the state.

Finally also the covariance of state error is updated:

$$\boldsymbol{P} = \boldsymbol{Y_1} - \boldsymbol{K}(\boldsymbol{P_{12}^T}) \tag{2.74}$$

It is important to remark that, since the *unscented Kalman filter* is based on a weighted sum, it is not guaranteed that the estimated quaternion is unitary. As a consequence the quaternion must be normalised after each estimation.

Unfortunately, the addition of such a non linear determination algorithm makes the simulation time to slow dramatically down. As a result, it was decided to maintain the *unscented Kalman filter* only for the most delicate phase, the picture acquisition, while for all the other phases, an algebric algorithm was implemented, based on the star tracker characteristics.

2.8.5 Attitude determination algebric algorithm

The star tracker provides multiple vectors of observations in the *body-fixed frame*, $\boldsymbol{O_1}$, $\boldsymbol{O_2}$, $\boldsymbol{O_3}$, ..., $\boldsymbol{O_i}$, and has in its memory a star catalogue with stars position vectors in *inertial frame*, $\boldsymbol{S_1}$, $\boldsymbol{S_2}$, $\boldsymbol{S_3}$, ..., $\boldsymbol{S_i}$. From this informations it is possible to retrieve the body-fixed frame matrix, $\boldsymbol{A_{b/n}}$, using the following expression [32]:

$$\boldsymbol{O_i} = \boldsymbol{A_{b/n}}\boldsymbol{S_i} \tag{2.75}$$

If we consider the 6 stars observable by the star tracker ST-200, the equations will be:

$$[\boldsymbol{O_1}\ \boldsymbol{O_2}\ \boldsymbol{O_3}\ \boldsymbol{O_4}\ \boldsymbol{O_5}\ \boldsymbol{O_6}] = \boldsymbol{A_{b/n}}\,[\boldsymbol{S_1}\ \boldsymbol{S_2}\ \boldsymbol{S_3}\ \boldsymbol{S_4}\ \boldsymbol{S_5}\ \boldsymbol{S_6}] \tag{2.76}$$

$$\boldsymbol{A_{b/n}} = [\boldsymbol{O_1}\ \boldsymbol{O_2}\ \boldsymbol{O_3}\ \boldsymbol{O_4}\ \boldsymbol{O_5}\ \boldsymbol{O_6}]\,[\boldsymbol{S_1}\ \boldsymbol{S_2}\ \boldsymbol{S_3}\ \boldsymbol{S_4}\ \boldsymbol{S_5}\ \boldsymbol{S_6}]^* \tag{2.77}$$

where " * " indicates the *Moore-Penrose pseudo-inverse operation* (a generalisation of the inverse operator for rectangular matrices [36]), since the matrices are not square.

An example of star catalogue format, in particular the one used in these simulations, is the following, [37]:

BRIGHT STARS, J2017.5

Designation	BS=HR No.	Right Ascension	Declination	Notes	V	$U-B$	$B-V$	Spectral Type
		h m s	° ′ ″					
17 SS Lep	2148	06 05 46.0	−16 29 12	sb	4.92	+0.20	+0.21	Ap (shell)
	2180	06 09 42.0	−22 25 54		5.49	−0.01	+0.01	A0 V
5 γ Mon	2227	06 15 42.6	−06 16 53	d	3.99	+1.32	+1.27	K1 III Ba 0.5
7 Mon	2273	06 20 33.4	−07 49 53	db	5.27	−0.18	−0.18	B2.5 V
2 β CMa	2294	06 23 28.3	−17 57 57	svdb	1.98	−0.24	−0.24	B1 II−III
	2305	06 24 59.3	−11 32 26		5.21	+1.23	+1.18	K3 III
4 ξ^1 CMa	2387	06 32 35.1	−23 25 55	vdb	4.34	−0.25	−0.24	B1 III
	2392	06 33 36.1	−11 10 49	dsb	6.30	+1.10	+0.95	G9.5 III: Ba 3
5 ξ^2 CMa	2414	06 35 47.4	−22 58 47		4.54	−0.04	−0.01	A0 III
7 ν^2 CMa	2429	06 37 26.9	−19 16 19		3.95	+1.04	+1.02	K1.5 III−IV Fe 1
8 ν^3 CMa	2443	06 38 39.6	−18 15 13	dm	4.42	+1.14	+1.12	K0.5 III
9 α CMa	2491	06 45 54.8	−16 44 30	odbn18	−1.44	+0.01	−0.02	A0m A1 Va
v592 Mon	2534	06 51 32.9	−08 03 45	sv	6.31	+0.01	+0.03	A2p Sr Cr Eu
16 o^1 CMa	2580	06 54 51.6	−24 12 26	s	3.89	+1.74	+1.58	K2 Iab
14 θ CMa	2574	06 55 00.2	−12 03 42		4.08	+1.42	+1.49	K4 III
20 ι CMa	2596	06 56 55.1	−17 04 41		4.36	−0.06	+0.01	B3 II
24 o^2 CMa	2653	07 03 45.3	−23 51 36	vasb	3.02	−0.08	−0.03	B3 Ia
23 γ CMa	2657	07 04 33.0	−15 39 37		4.11	−0.11	−0.09	B8 II
25 δ CMa	2693	07 09 06.2	−26 25 19	dasb	1.83	+0.67	+0.67	F8 Ia
27 EW CMa	2745	07 14 58.0	−26 23 01	dbm	4.42	−0.17	−0.12	B3 IIIep
28 ω CMa	2749	07 15 31.3	−26 48 14		4.01	−0.15	−0.08	B2 IV−Ve
30 τ CMa	2782	07 19 26.1	−24 59 14	vdbm	4.37	−0.13	−0.10	O9 II

Figure 2.13: *Example of star catalogue format used in this thesis work, [37].*

Then, as explained in Subsection 2.8.2, an accuracy matrix, $\boldsymbol{A_\epsilon}$, is multiplied to the obtained body-fixed frame matrix, $\boldsymbol{A_{b/n}}$, in order to take into consideration also the star tracker accuracy.

$$\boldsymbol{A_{b/n,real}} = \boldsymbol{A_\epsilon A_{b/n}} \tag{2.78}$$

2.9 Actuators and control algorithm

The control law driving the attitude control block in the ADCS loop, Figure 2.14, is a Proportional and Derivative law (PD), whose parameters were numerically optimised. In Section 5.4, a complete description of the optimisation logic is reported. The Integrative term of a classic PID controller was discarded in order to speed up the code, since no beneficial effect from the controllability point of view was evidenced once implemented.

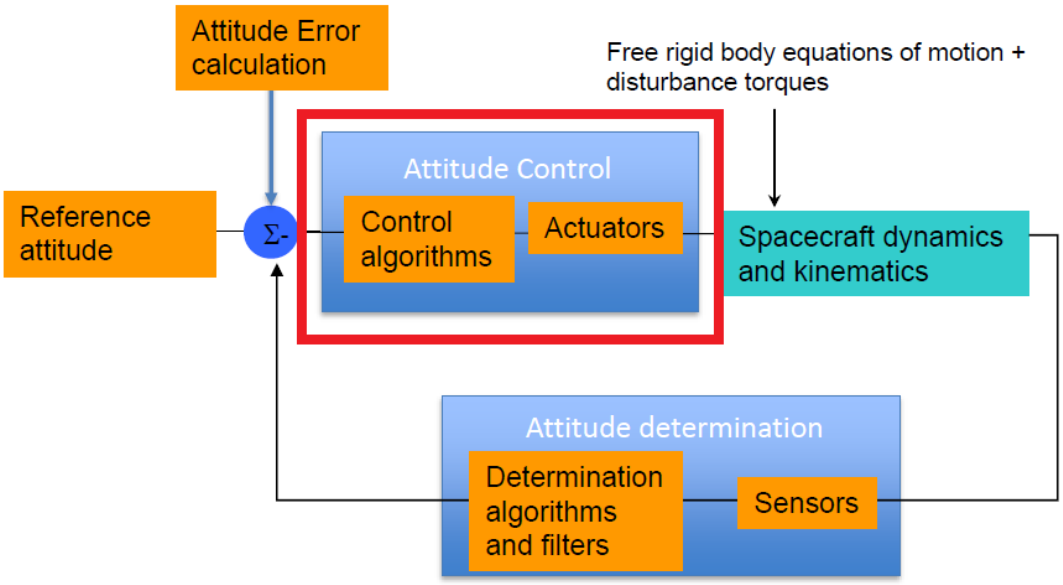

Figure 2.14: *ADCS feedback loop with* control *block highlighted.*

According to the stability theory of non linear systems [22], the control law of a PD controller shall be based on a Lyapunov function, $\Gamma(\boldsymbol{x})$, dependent on the state $\boldsymbol{x}$. In order to assure asymptotic stability the following relations have to be satisfied, [22]:

- $\Gamma(\boldsymbol{x}) > 0, \forall\ \boldsymbol{x} \neq \boldsymbol{x_{eq}}$
- $\Gamma(\boldsymbol{x}) = 0$, for $\boldsymbol{x} = \boldsymbol{x_{eq}}$
- $\dot{\Gamma}(\boldsymbol{x}) < 0$

and for Lyapunov stability:

- $\Gamma(\boldsymbol{x}) > 0, \forall\ \boldsymbol{x} \neq \boldsymbol{x_{eq}}$
- $\Gamma(\boldsymbol{x}) = 0$, for $\boldsymbol{x} = \boldsymbol{x_{eq}}$
- $\dot{\Gamma}(\boldsymbol{x}) \leq 0$

For the simulator implemented, the method to represent the reference frame are the quaternions and, as a consequence, it was selected a Lyapunov function based on the scalar number of the error quaternion, $q_{e,4}$:

$$\Gamma(q_{e,4}) = 1 - q_{e,4}^2 \tag{2.79}$$

where $\boldsymbol{q_e}$ represents the error between the actual quaternion and the target one. To evaluate it, the following steps are requested:

1. Transform the target attitude matrix $\boldsymbol{A_t}$ matrix in control quaternion: $\boldsymbol{q_c}$. $\boldsymbol{A_t}$ is mission phase dependent and, as a consequence, it will be presented in Chapter 5.

2. Compute the error between the actual quaternion $\boldsymbol{q}$ and the control one $\boldsymbol{q_c}$, exploiting the quaternion multiplication:

$$\boldsymbol{q_e} = (\boldsymbol{q_c})^{-1} \otimes \boldsymbol{q} \tag{2.80}$$

   Meaning, in matrix form:

$$\boldsymbol{q_e} = \begin{bmatrix} q_{4c} & q_{3c} & -q_{2c} & -q_{1c} \\ -q_{3c} & q_{4c} & q_{1c} & -q_{2c} \\ q_{2c} & -q_{1c} & q_{4c} & -q_{3c} \\ q_{1c} & q_{2c} & q_{3c} & q_{4c} \end{bmatrix} \boldsymbol{q} \tag{2.81}$$

   where, if $\boldsymbol{q_c} = [0\ 0\ 0\ 1]$, it means that $\boldsymbol{q_e} = \boldsymbol{q}$.

Eq. (2.79) was selected since it is immune to *unwinding*, which is a typical issue, when quaternions are exploited [22]. It is due to the not uncertainty about the scalar number sign while transforming the quaternion to direct cosine matrices and viceversa. The square in the law has the role to make the Lyapunov function independent from the sign of $q_{e,4}$

Once the control law is selected, the control torque will be:

$$\boldsymbol{u} = K_p \frac{\partial \Gamma}{\partial q_{e,4}} \boldsymbol{q(1,2,3)} + K_d(\boldsymbol{\omega_t} - \boldsymbol{\omega}) \tag{2.82}$$

$$\boldsymbol{u} = -2K_p \boldsymbol{q_{e,4}} \boldsymbol{q_e(1,2,3)} + K_d(\boldsymbol{\omega_t} - \boldsymbol{\omega}) \tag{2.83}$$

where:

- K_p and K_d are respectively the proportional and derivative constants, both positive. They will be obtained through single and double objective optimisations, depending on the mission and on the single phase. The description of optimisation logic will be presented in Section 5.4.
- $\boldsymbol{\omega_t}$ are the target angular velocities.
- $\boldsymbol{q_e}$ is the error quaternion between the actual attitude matrix, $\boldsymbol{A_{b/n}}$, and the target one, $\boldsymbol{A_t}$, transformed in quaternions.

The available for both the OUFTI-Next and the ZodiArt missions are *magnetic torquers* and *reaction wheels*. In this section their main characteristics will be described, as well as their implementation in the simulator.

2.9.1 Magnetic torquers

Magnetic torquers, are devices producing a dipole moment capable to interact with the Earth magnetic sphere and turn the spacecraft. In order to command them it is possible to change the input current flowing in the armatures to change the dipole moment. They will be used during de-tumbling phase with a control strategy that will be presented afterwards in Section 5.1. In order to model them, the ideal magnetic dipole requested is compared with the maximum available from the magnetic torquers and the output will be eventually saturated. The common configuration is based on 3 of them directed as the spacecraft axes of symmetry.

2.9.2 Reaction wheels

Reaction wheels (RW) are rotating devices with a fixed position inside the spacecraft, usually directed as the yaw, pitch and roll axis, as shown in Figure 2.15.

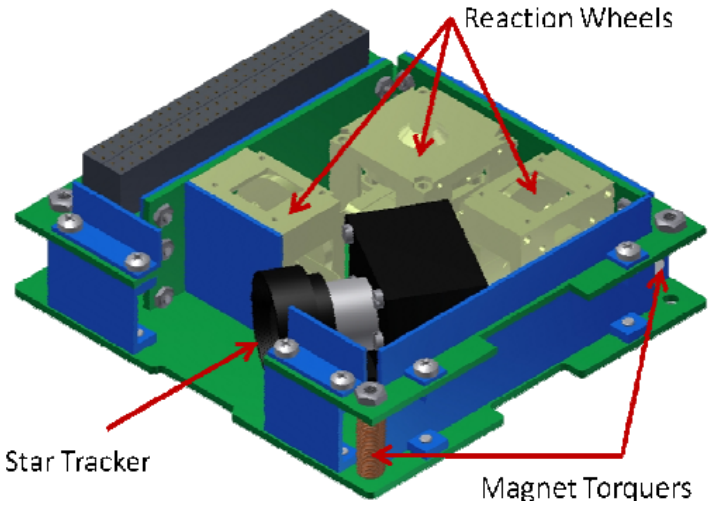

Figure 2.15: *Three reaction wheels common configuration [38].*

They are able to produce a variable torque on the satellite thanks to their angular acceleration. Their torque equation is:

$$\boldsymbol{u} = \boldsymbol{A}\boldsymbol{h}_r \times \boldsymbol{\omega} - \boldsymbol{A}\dot{\boldsymbol{h}}_r \tag{2.84}$$

where:

- $\boldsymbol{A}$ is the constant reaction wheels configuration matrix, in this case, the unit matrix $\boldsymbol{I}$.
- $\boldsymbol{h}_r$ is the reaction wheels momenta vector.

In order to model their dynamics, from the control required, $\boldsymbol{u_d}$, the required momentum, $\boldsymbol{h_{r,d}}$, is integrated, using the following differential equation:

$$\dot{\boldsymbol{h}}_{\boldsymbol{r,d}} = \boldsymbol{A}^{-1}(\boldsymbol{A}\boldsymbol{h}_{\boldsymbol{r,d}} \times \boldsymbol{\omega} - \boldsymbol{u_d}) \tag{2.85}$$

and then $\boldsymbol{h_{r,d}}$ and $\dot{\boldsymbol{h}}_{\boldsymbol{r,d}}$ are compared with the maximum and minimum ones provided by the wheels and eventually are saturated, if they are higher or lower. At this point the effective torque is evaluated:

$$\boldsymbol{u} = \boldsymbol{A}\boldsymbol{h_r} \times \boldsymbol{\omega} - \boldsymbol{A}\dot{\boldsymbol{h}}_{\boldsymbol{r}} \tag{2.86}$$

Reaction wheels are characterised by a peculiar issue: during long controlled phases, the wheels are continuously increasing their momentum in order to counteract the external disturbances. Once the maximum value of momentum is reached, the wheels can not accelerate and the control is lost. Once the maximum momentum storable is reached, a de-saturation phase is needed.

2.10 Solver choice and Numerical stability

Once the model is implemented, it is important to choose the right solver among the ones available on Matlab/Simulink^{TM}. The solver available are:

- *ODE45*: based on an explicit Runge-Kutta (4,5) formula, it is a one-step solver. [39][40]
- *ODE23*: an implementation of an explicit Runge-Kutta (2,3) pair of Bogacki and Shampine. It may be more efficient than ode45 at crude tolerances and in the presence of moderate stiffness. *Ode23* is a single-step solver. [41][40]
- *ODE 113*: a variable-step, variable-order Adams-Bashforth-Moulton PECE solver of orders 1 to 13. [42][40]
- *ODE15s*: a variable and multi-step, variable-order solver based on the numerical differentiation formulas of orders 1 to 5, used for stiff problems. [43][40]
- *ODE23s*: based on a modified Rosenbrock formula of order 2. Because it is a single-step solver, it may be more efficient than *ode15s* at solving problems that permit crude tolerances or problems with solutions that change rapidly. It can solve some kind of stiff problems for which *ode15s* is not effective. [40]

Eqs. (2.11)-2.12-2.85 were integrated with each of these solvers, providing the same results with different computational times.
The solver chosen is *ODE15s*, since it is the fastest among the previous ones. Here is reported a table comparing the times requested by each solvers to simulate a

Sun-pointing phase of 200 s with solver absolute and relative tolerances set to 10^{-6}, with a processor Intel®Core ^{TM}i7-7700HQ CPU at 2.80 GHz RAM 16GB.

Table 2.1: *Solvers computational velocity on the Sun-pointing phase.*

Solver	**CPU time** (s)
ODE45	651.89
ODE23	340.37
ODE113	365.14
ODE15s	8.42
ODE23s	48.87

In order to check for solver numerical stability, the method reported in [44] was adopted, based on the linearisation around one random initial condition

$$\boldsymbol{x_0} = [\boldsymbol{\omega_0};\ \boldsymbol{q_0};\ \boldsymbol{h_{r,0}}]$$

Table 2.2: *Initial condition.*

$\omega_{x,0}(rad/s)$	$\omega_{y,0}(rad/s)$	$\omega_{z,0}(rad/s)$	$q_{1,0}(-)$	$q_{2,0}(-)$
$9e^{-4}$	$9e^{-4}$	$9e^{-4}$	$1/\sqrt{(3)}$	$1/\sqrt{(3)}$
$q_{3,0}(-)$	$q_{4,0}(-)$	$h_{r1,0}(Nms)$	$h_{r2,0}(Nms)$	$h_{r3,0}(Nms)$
$1/\sqrt{(3)}$	0	0	0	0

The numerical stability analysis reported in this thesis is just local, but can be indicative for the choice of the solver.
Once having obtained the Jacobian of the model evaluated in the initial condition, the eigenvalues were computed and multiplied times the maximum and minimum discretized time interval taken by *ODE15s* and then plotted on the solver region of stability (*ODE15s* is a back-differentiation technique). The eigenvalues of the system are the ones reported in Table 2.3.

Table 2.3: *De-coupled linearised model eigenvalues real (Re) and imaginary (Im) parts.*

Re	Im
-0.4970	0
-0.4623	0.0054
-0.4623	-0.0054
$+0.0342$	0
-0.0004	0.0051
-0.0004	-0.0051
0	$+0.0015$
0	-0.0015
$6e^{-5}$	0
0	0

Figures 2.16–2.17 show the regions of stability, [45], differently zoomed, in the complex $\lambda \times \Delta t$ domain, where λ are the eigenvalues of the system and Δt the solver discretised time interval. The colored curves represent the different backward differentiation algorithm orders. Unfortunatelly, due to scaling issues, it is not possible to report all the eigenvalues positions, but, since the solver selected is characterised by a region of numerical stability spreading outside the colored curves, the stable eigenvalues are included in the regions of stability (providing, as a result, a stable dynamics) and the unstable ones are outside (providing, correctly, an unstable dynamics), proving the numerical stability in accordance with [44].

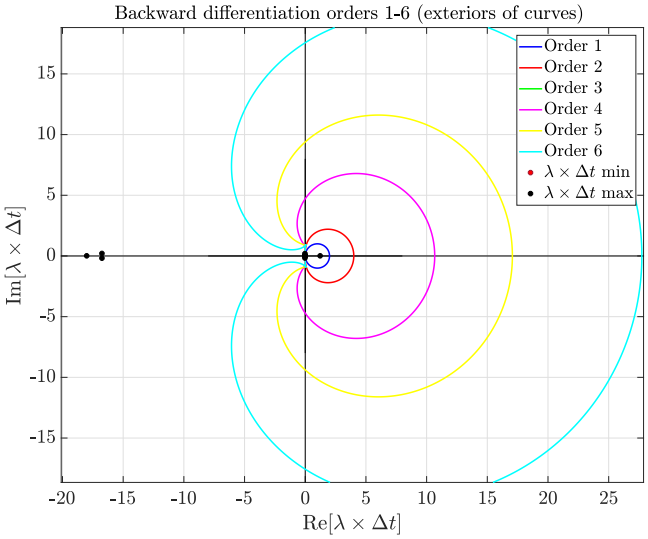

Figure 2.16: *De-coupled model numerical stability in $\lambda \times \Delta t$ domain.*

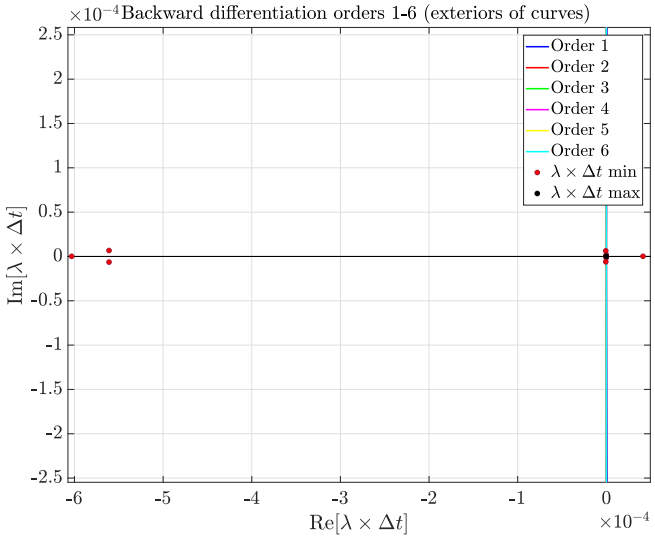

Figure 2.17: *De-coupled model numerical stability in $\lambda \times \Delta t$ domain, zoomed on the origin.*

CHAPTER 3

ORBITAL-ATTITUDE COUPLED SIMULATOR

In this chapter the whole set of differential equations are reported, coupling the attitude dynamics, with the orbital one, both presented in Chapter 2. In particular, the orbital dynamics was coupled through the perturbative acceleration induced by atmospheric drag, lift and SRP and not evaluated a priori and then interpolated, as shown for the decoupled model. The attitude dynamics is driven by the Euler equations, Eqs. (2.11), the quaternion integration, Eq. (2.12), and the reaction wheel momenta equation, Eq. (2.85), as reported in Chapter 2, providing 10 states:

$$\boldsymbol{\omega} = [\omega_1 \ \omega_2 \ \omega_3]^T \quad \boldsymbol{q} = [q_1 \ q_2 \ q_3 \ q_4]^T \quad \boldsymbol{h_r} = [h_{r,1} \ h_{r,2} \ h_{r,3}]^T$$

Then, Gauss planetary equations, Eq. (2.14) to 2.19, drive instead the orbital dynamics, providing 6 states: h_m, e, i, Ω, ω, θ. The overall coupled dynamics here collected from Eq. (3.1) to 3.11:

$$\dot{h}_m = r p_s \tag{3.1}$$

$$\dot{e} = \frac{h}{\mu} sin\theta p_r + \frac{1}{\mu h}[(h^2 + \mu r)cos\theta + \mu e r] p_s \tag{3.2}$$

$$\dot{\theta} = \frac{h}{r^2} + \frac{1}{eh}[\frac{h^2}{\mu} cos\theta p_r - (r + \frac{h^2}{\mu}) sin\theta p_s] \tag{3.3}$$

$$\dot{\Omega} = \frac{r}{h sin\, i} sin(\omega + \theta) p_w \tag{3.4}$$

$$\dot{i} = \frac{r}{h} cos(\omega + \theta) p_w \tag{3.5}$$

$$\dot{\omega} = -\frac{1}{eh}[\frac{h^2}{\mu} cos\theta p_r - (r + \frac{h^2}{\mu}) sin\theta p_s] - \frac{r sin(\omega + \theta)}{h tan\, i} p_w \tag{3.6}$$

$$\dot{\omega}_1 = \frac{I_2 - I_3}{I_1} \omega_2 \omega_3 + \frac{u_1 + d_1}{I_1} \tag{3.7}$$

$$\dot{\omega}_2 = \frac{I_3 - I_1}{I_2} \omega_1 \omega_3 + \frac{u_2 + d_2}{I_2} \tag{3.8}$$

$$\dot{\omega}_3 = \frac{I_1 - I_2}{I_3} \omega_2 \omega_1 + \frac{u_3 + d_3}{I_3} \tag{3.9}$$

$$\dot{\boldsymbol{q}} = \frac{1}{2} \begin{bmatrix} 0 & \omega_3 & -\omega_2 & \omega_1 \\ -\omega_3 & 0 & \omega_1 & \omega_2 \\ \omega_2 & -\omega_1 & 0 & \omega_3 \\ -\omega_1 & -\omega_2 & -\omega_3 & 0 \end{bmatrix} \boldsymbol{q} \tag{3.10}$$

$$\dot{\boldsymbol{h}}_{\boldsymbol{r}} = \boldsymbol{A}^{-1}(\boldsymbol{A}\boldsymbol{h}_{\boldsymbol{r}} \times \boldsymbol{\omega} - \boldsymbol{u}) \tag{3.11}$$

The perturbative vector $\boldsymbol{p}$ is the sum of the perturbative accelerations due to: Earth zonal harmonics, Moon and Sun third body perturbations, solar radiation pressure, drag and lift. The accelerations due to lift, drag and solar radiation pressure depend on the cross surfaces exposed to the atmospheric and solar wind, as shown in Chapter 2. In the coupled simulator, differently from before, this surfaces are now function of the spacecraft's attitude through the exposed surfaces normal unit vectors $\boldsymbol{n_i}$ and this new dependency couples the orbital dynamics with the attitude one. This is clearly visible in, Eqs. (3.12) to 3.14, where, in particular in the first two equations,

$$0 \leq \boldsymbol{n_i} \cdot \frac{\boldsymbol{v_{rel}}}{||\boldsymbol{v_{rel}}||} \leq 1$$

identifies the portion of cross surfaces exposed to the atmospheric wind, when multiplying the exposed surfaces $A_{d,i}$, while in the last one, the scaling factor for $A_{s,i}$ is $(\hat{\boldsymbol{S}} \cdot \boldsymbol{n_i})$. N is the spacecraft number of surfaces.

$$\boldsymbol{p_{drag}} = -\frac{1}{2}\rho(h)\frac{C_d}{m}\sum_i^N A_{d,i}\left(\boldsymbol{n_i}\cdot\frac{\boldsymbol{v_{rel}}}{||\boldsymbol{v_{rel}}||}\right)\boldsymbol{v_{rel}}||\boldsymbol{v_{rel}}|| \tag{3.12}$$

$$\boldsymbol{p_{lift}} = \frac{1}{2}\rho(h)\frac{C_l}{m}\sum_i^N A_{d,i}\left(\boldsymbol{n_i}\cdot\frac{\boldsymbol{v_{rel}}}{||\boldsymbol{v_{rel}}||}\right)\frac{\boldsymbol{v_{rel}}\times(\boldsymbol{v_{rel}}\times\boldsymbol{n_i})}{||\boldsymbol{v_{rel}}\times(\boldsymbol{v_{rel}}\times\boldsymbol{n_i})||}||\boldsymbol{v_{rel}}||^2 \tag{3.13}$$

$$\boldsymbol{p_{srp}} = \frac{P_{SR}}{m}\sum_i^N A_{s,i}\Big[\rho_a(\hat{\boldsymbol{S}}\cdot\boldsymbol{n_i}) + 2\rho_s(\hat{\boldsymbol{S}}\cdot\boldsymbol{n_i})^2\cdot\boldsymbol{n} + \frac{2}{3}\rho_d(\hat{\boldsymbol{S}}\cdot\boldsymbol{n_i})\Big] \tag{3.14}$$

The two dynamics are coupled since $\boldsymbol{u}$ and $\boldsymbol{d}$ in Euler equations, Eqs. (3.7) to Eq. (3.9), are function of the spacecraft position and velocity, provided by the integration of keplerian parameters, through Gauss planetary equations, Eq. (3.1) to 3.6, which depend on the perturbative accelerations, Eqs. (3.12) to 3.14, function of the attitude.
In conclusion, there are 16 first order differential equations and, as a consequence, 16 states to be integrated.

3.1 Numerical stability

In order to check for solver numerical stability [44], the model was linearised around the initial condition already exploited for the de-coupled model stability analysis, Table 2.2, with the addition of the ZodiArt orbit initial conditions, Table 9.1.

The eigenvalues of the Jacobian matrix are reported in Table 3.1.

Table 3.1: *Coupled linearised model eigenvalues real (Re) and imaginary (Im) parts.*

Re	**Im**
-0.4970	0
-0.4623	0.0054
-0.4623	-0.0054
$+0.0342$	0
-0.0004	0.0051
-0.0004	-0.0051
0	-0.0015
0	$+0.0015$
$2.37e^{-6}$	$-1.3e^{-3}$
$2.37e^{-6}$	$+1.3e^{-3}$
$8.749e^{-5}$	$4.056e^{-8}$
$6e^{-5}$	0
$-8.746e^{-5}$	$4.053e^{-8}$
$2.63e^{-9}$	0
0	0
0	0

Figure 3.1 represents the regions of stability zoomed on the origin of the coordinates reference system, in the $\lambda \times \Delta t$ domain, where λ are the eigenvalues of the system and Δt the solver discretised time interval. The orbital dynamics eigenvalues are characterised by sensibly smaller magnitudes and, as a result, it was decided to present just the focus on them, close to the origin, since the remaining eigenvalues are the same already shown in the de-coupled model numerical stability analysis. The colored curves represent the different backward differentiation algorithm orders. As for the decoupled simulator, it is not possible to report all the eigenvalues positions due to scaling issues, but, since the solver selected is characterised by a region of numerical stability spreading outside the colored curves, the stable eigenvalues are included in the regions of stability (providing, as a result, a stable dynamics) and the unstable ones are outside (providing, correctly, an unstable dynamics), proving the numerical stability in accordance to [44].

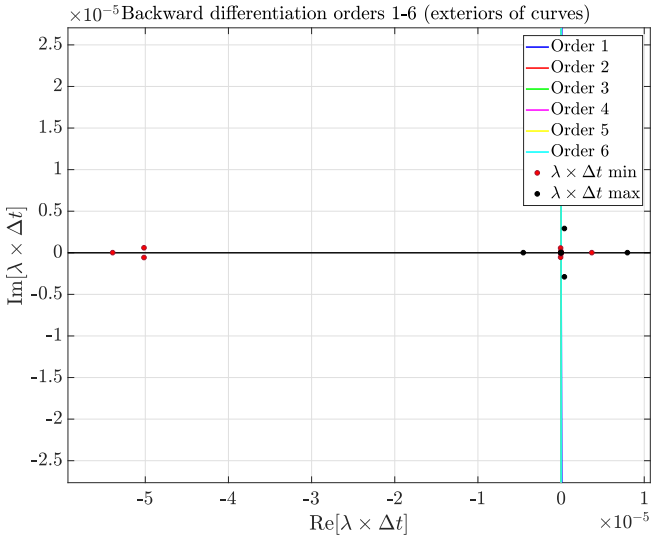

Figure 3.1: *Coupled model numerical stability in $\lambda \times \Delta t$ domain, zoomed on the origin.*

Part II

The OUFTI-Next Mission and the Attitude-Orbit Decoupled Simulator

CHAPTER 4

INTRODUCTION TO THE OUFTI-NEXT MISSION

THE OUFTI-Next project was born at University of Liége in November 2016, as a continuation of the first CubeSat ever launched in Belgium, OUFTI-1, Figure 4.1, in April 2016, when Bernard Tychon proposed to build a constellation of 3 Unit CubeSat capable to detect hydraulic stress in agricultural fields and to provide useful informations about their correct irrigation. Currently the team is working on the mission demonstrator and the *phase A* of the project has coming to its end: each subsystem, except for the ADCS, has been preliminary designed. The decoupled simulator implemented for this Thesis was exploited to size the OUFTI-Next actuators and sensors, selecting the best ADCS unit available on market, and to simulate the nominal mission profiles.

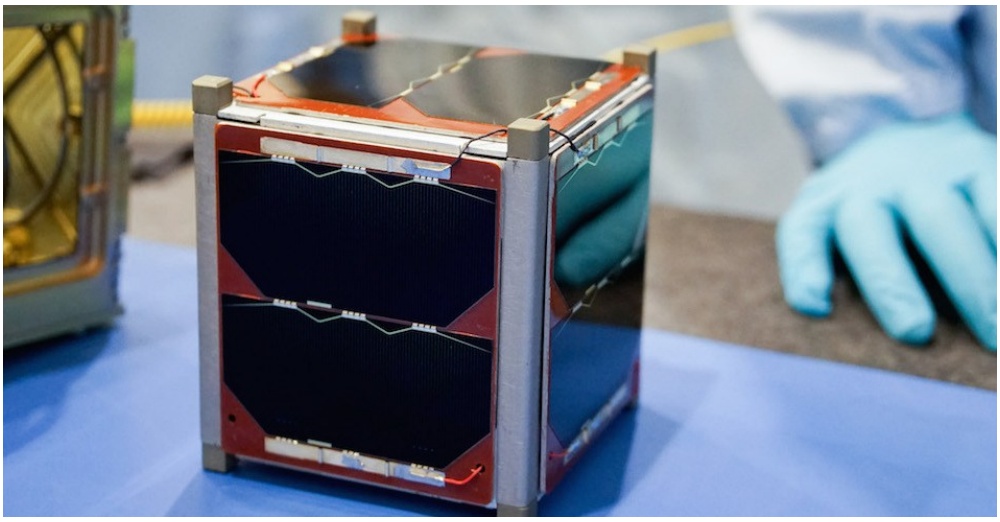

Figure 4.1: *OUFTI-1 CubeSat.*

The orbital dynamics is still not coupled with the attitude one, since the surfaces of the platform are not optimal to be subjected or to exploit the perturbative coupled dynamics, and, as a result, the OUFTI-Next ephemeris are provided as an input to the simulator, instead of integrated from the orbital dynamics equations. After the description of the ADCS requirements and previous mission deisgn steps reported in Section 4.1, Part II is divided in chapters describing the mission profiles selected for the simulations, the control parameters optimisation logic and the general results obtained for the mission profiles selected.

One of the peculiarities of the OUFTI-Next platform is the presence of a cryocooler on-board, needed to cool down the IR detector before picture acquisition phase. This device introduces vibrations which will be partially counteracted by mechanical dampers. The satisfaction of pointing requirements also in the presence of cryocooler vibrations was checked in Section 7.1. In Section 7.2 is instead reported the additional analysis about the trade-off between two suitable ADCS units available on market. Finally in Section 7.3 two emergency modes are presented, both in the case of one reaction wheel or the star sensor failures.

4.1 The OUFTI-Next mission requirements and previous design steps

In this section the high level requirements for the ADCS are presented and shown in Table 4.1, as well as preliminary considerations about the subsystem.

Table 4.1: *The OUFTI-Next project ADCS preliminary requirements. M is refered to Mandatory and NH to Nice to Have.*

REQ. ID	Importance	Requirement	Note
ON-P-F-ADCS-0010	M	The ADCS shall be able to detumble the spacecraft after detachment from the launcher	ON=OUFTI-Next, P=Platform, F=Functional
ON-P-F-ADCS-0020	M	The ADCS shall provide sun-pointing with the faces covered by solar panels, during "Charging Mode".	
ON-P-F-ADCS-0030	M	The ADCS shall provide ground station with the face where the S-band antenna is body-mounted, during "Downloading Mode".	
ON-P-F-ADCS-0040	M	The ADCS shall provide a target following slew maneuver, during "Acquisition Mode".	
ON-P-F-ADCS-0050	M	The ADCS shall be able to determine the attitude within ± 1 arcsec in each axis.	
ON-P-F-ADCS-0060	M	The ADCS shall provide a desaturation strategy.	
ON-P-F-ADCS-0070	M	The ADCS shall counteract environmental disturbances.	e.g.: SRP, Atmospheric Drag, etc.
ON-P-F-ADCS-0080	M	The ADCS shall counteract internal disturbances.	e.g. Cryocooler vibrations
ON-P-F-ADCS-0090	M	The ADCS pack shall be chosen among the ones available on the market.	e.g.: BCT, KUL, etc.
ON-P-F-ADCS-0100	NH	The ADCS pack shall be chosen among the ones available on the national (Belgium) market.	e.g.: KUL
ON-P-F-ADCS-0110	M	The ADCS shall be able to provide a pointing accuracy of $< 0.1°$ and a control stability of $< 0.01°$ (0.05 arcmin) during "Acquisition Mode".	

At the University of Liége a preliminary trade-off among the COTS models for GNSS units was done in [46] and reported in Table 4.2. In [46] also a preliminary ADCS unit selection was performed, providing as the best solution, especially for its reduced volume, the *iADCS100*, whose characteristics are presented in Table 4.3. However, a new unit, built in KULeuven was proposed and the trade-off between

Table 4.2: *GNSS COTS models, [46].*

Name Company	**GNSS200** Hyperion	**GPSRM 1** Pumpkin/Novatel	**piNAV-NG** SkyFox Labs	**SGR-05P** Surrey
Mass	1.5 g	109 g	24 g	60 g
Size	20x15x2 mm	96x90x16 mm	71.1x45.7x11 mm	103x64x11 mm
Position accuracy	8 m	1.5 m (RMS)	10 m (2σ)	10 m (2σ)
Velocity accuracy		0.03 m/s (RMS)	0.10 m/s (2σ)	0.15 m/s (2σ)
Time accuracy		20 ns (RMS)	100 ns (2σ)	500 ns (2σ)
Time-to-first-fix	120 s (passive antenna)	50 s	90 s	90 s
Typical operating voltage	3.3 V	5 V	3.3 V	3.3 V
Typical power consumption	157 mW	1.3 W	125 mW (passive antenna)	1 W (active antenna)
Operating temperature	−45 °C to 85 °C	−40 °C to 85 °C	−40 °C to 85 °C	−20 °C to 50 °C
Operating constellation	Multi constellation	GPS GLONASS	GPS	GPS
Cost		7980 $	6900 $	
Remarks	Integrates seamlessly with ADCS from Hyperion	GOMspace also proposes a model from Novatel		

these two devices will be presented in Section 7.2.

Table 4.3: *iADCS100 unit characteristics and performances, [46].*

Hyperion Berlin Space Technologies **iADCS100**	
Mass	470 g
Size	0.3 U
Pointing accuracy	30 arcsec
Pointing control/stability	$\leq 1°$
Slewing rate	$> 1.5°/s$
Sensors	- Magnetometers - Gyroscope - Star Tracker
Actuators	- Reaction wheels - Magnetometers
Operating temperature	−45 °C to 40 °C
Power	1.4 W
Cost	75000 $

4.1.1 Body-frame reference frame

The OUFTI-Next *body-frame reference frame* is characterised by the X-axis directed in the opposite direction with respect to the detector pointing vector, while the Z and Y-axis are oriented in directed towards the surfaces with solar panels, as shown in Figure 4.2. The S-band antenna is considered to be oriented along the -Z-axis.

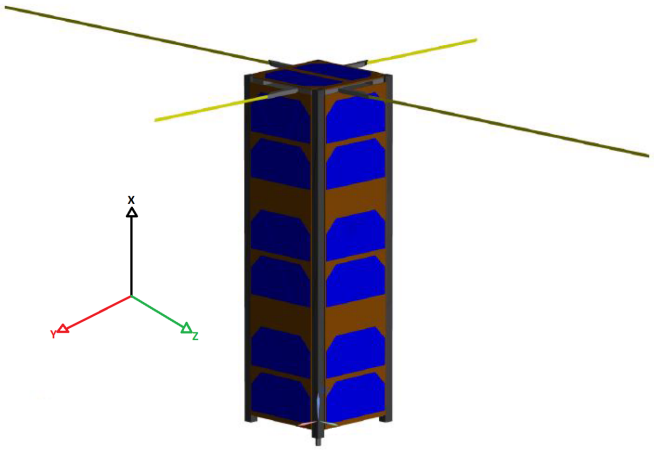

Figure 4.2: *The reference frame used for the design of the OUFTI-Next ADCS, [46].*

In this chapter also previous important design steps about the other subsystems are reported, which are relevant from the ADCS point of view: *Mission Analysis, Telemetry & Telecommunication, Electric Power, Configuration* and *Payload*. All the results presented were obtained in [46].

4.1.2 Mission Analysis

The most important design choice was to shoot pictures while being over the area of interest between 12:00 and 14:00 in solar time. It is also known as the Local Mean Time (LMT). In order to satisfy this constraint, two orbits were investigated: ISS (400km) and SSO (650km). Each orbit will be studied with its relative attitude.

4.1.2.1 ISS orbit

The orbital parameters are provided in Table 4.4.

Table 4.4: *ISS orbital parameters*

Semi-major axis (km)	about 400
Eccentricity (-)	0.0003830
Inclination (deg)	51.6416
RAAN (deg)	321, 9140 or user defined
Argument of perigee (deg)	239.4439 or user defined
True anomaly (deg)	user defined

The ground tracks repetition is about 59.5 days, meaning that the Local Mean Time LMT repeats at the equator each 59.5 days. It is remarkable that for 1-3 days the satellite will see mostly oceans in the southern hemisphere, independently from epoch, RAAN, argument of perigee and true anomaly, since the passages are cyclic. The lifetime on this orbit is about 5.5 months. Similar results were obtained also for the SSO at 650 km altitude. Nevertheless this solution can increase the lifetime of about 2 years.

4.1.2.2 SSO orbit

The SSO, whose Keplerian parameters are reporte in Table 4.5, will not be maintained Sun-Synchronous, since no propulsion is provided in the OUFTI-Next platform.

Table 4.5: *SSO (655 km) with* $\tau_{AN} = 13:30$. *Epoch: January 1, 2019, [46].*

Date	a [km]	h [km]	i [deg]	e [-]	Ω [deg]	ω [deg]	M [deg]
2019-01-01 00:00:00	7033.4	655	98.01	0	124.71	0	0

Then, in order to define a Sun-Synchronous orbit, it is fundamental to provide the LMT at the ascending node, τ_{AN}, since it will remain constant due to the orbit properties. In [46], it was decided to have a $\tau_{AN} = 13:30$, in order to provide between 12:00 and 14:00 LMT a quite wide range of altitudes, as shown in Figure 4.3.
It seems that an even higher in altitude SSO is the best solution for the OUFTI-Next mission, but the problem is the necessity to de-orbit without propulsion, since the lifetime will be longer than 25 years, as requested by the Orbit Disposal Guideline, [47]. Moreover, it is important to notice that, if images are acquired close to 12:00 LMT, Sun glint could be a problem.
As stated before, all the orbits will be analysed from the point of view of the ADCS subsystem. Anyway some important conclusions can be listed:

- On the one hand, ISS orbit has too long and variable (due to drag) repeated ground tracks and, as a result, it cannot be exploited for smart irrigation

experiments. On the other hand it provides a life-time compatible with the IADC Space Debris Mitigation Guidelines, [47].

- SSO orbits provide instead almost constant (low perturbation level) recursions of even 10 days, but the disposal phase remains irresolvable without propulsion.

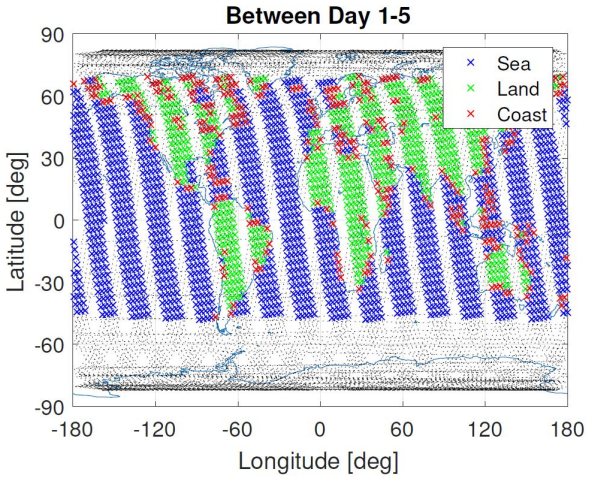

Figure 4.3: *SSO (600 km) with $\tau_{AN} = 13:30$. Epoch: January 1, 2019, [46].*

4.1.3 Telemetry & Telecommunication subsystem

From the Telemetry & Telecommunication subsystem (TMTC or COM) equipment point of view, there is a S-band antenna body-mounted on one of the lateral surfaces not covered by solar panels. Being the platform symmetric, it was decided to place the antenna on the -Z face. It was demonstrated that the visibility time during a passage above Liége is on the average (among the 3 orbits studied) about 6 min, meaning that, simply Nadir pointing with the -Z surface, it is possible to download more than one image per passage, being the time requested to download an image, as shown in Table 4.6.

Table 4.6: *Time to download 1 image in S-band, depending on the bit depth, [46].*

	Bit depth			
S-band (1 Mbps)	8 bits	10 bits	12 bits	14 bits
	2.6 s	3.3 s	3.9 s	4.6 s

In order to receive the signal, a passive antenna was considered to be sufficient.

4.1.4 Electric Power Subsystem

Concerning the Electric Power Subsystem EPS, the optimal configuration for solar panels is the following: 2 X 3U panels on a long face as well as on 1U panel on +Z. Indeed, this configuration can increase the power generated up to 10 W, but the satellite needs to be oriented correctly to the sun. The optimum is a rotation of $-13°$ around X or Y to see the top face and 45° around Z to present the corner between two long faces, [46]. In Figure 4.4 the OUFTI-Next platform is shown from the point of view of the Sun.

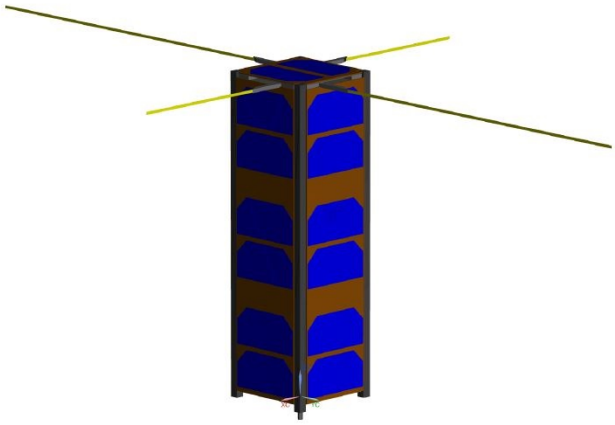

Figure 4.4: *Optimum orientation of the platform for the EPS subsystem. View from the sun to the satellite, [46]. The reference frame indicated is different from the one used in this Thesis.*

Nevertheless, the Sun-sensors integrated inside the solar panels are quite course in accuracy: $\approx$ 10 deg. Some companies integrates finer Sun-sensors inside the ADCS unit, but this is not the case for *iADCS100*. Since the ADCS unit has not been selected yet, both the 1 X 3U and 2 X 3U + 1 X 1U strategies will be studied. In Table 4.7, the power budget in the case of 1 X 3U strategy is presented, [46]:

Table 4.7: *1 x 3U power budget, [46].*

Sun pointing		Nadir pointing	
ISS (400 km)	SSO (600 km)	ISS (400 km)	SSO (600 km)
4.2 W	4.5 W	1.4 W	1.5 W

These data were compared with the power consumption levels, as shown in Table 4.8, where OBC is refered to the On-Board Computer.

Table 4.8: *Power consumption levels, [46].*

Sub-Systems		Sun Pointing		Acquisition		Communication	
		Nominal	20% Margin	Nominal	20% Margin	Nominal	20% Margin
ADCS							
iADCS100 (Hyperion)	mW	1400	1680	1400	1680	1400	1680
GNSS (Hyperion)	mW	157	188	157	188	157	188
COM							
COM Rx (UHF)	mW	240	288	240	288	240	288
COM Tx (VHF)	mW	0	0	0	0	1740	2088
S-Band Tx	mW	0	0	0	0	2500	3000
BNC (Beacon)	mW	250	300	250	300	250	300
EPS							
Picasso S/C (Clydespace)	mW	200	240	200	240	200	240
OBC							
iOBC (ISIS)	mW	400	480	400	480	400	480
PAYLOAD							
Cooling system (cryocooler)	mW	0	0	9750	11700	0	0
MWIR detector	mW	1	1.2	100	120	1	1.2
VIS detector	mW	1	1.2	244	292.8	1	1.2
Total Power	mW	2649	3179	12741	15289	6889	8267

4 scenarios are reported in Table 4.9: case 1 is not an interesting one since nothing happens in contrary to case 2. For this one, the margin is almost 15%. Moreover, a 20% margin was already considered for the consumption. It means that one image per orbit is clearly feasible. One orbit can be fully dedicated to download data but it can also be done on the same orbit (case 3).

Table 4.9: *Power budget (cryocooler) on two orbits (mean power and 20% margin on the consumption). Two orbits considered: SSO at 600 km with $\tau_{AN} = 13 : 30$ and the ISS orbit. Scenarios: 1: Sun pointing during full illumination and idle in eclipse. Scenario 2: Sun pointing + acquisition (4 min) during full illumination and idle in eclipse. Scenario 3: Sun pointing + acquisition (4 min) + communication (8 min) during full illumination and idle in eclipse. Scenario 4: Sun pointing + acquisition (4 min) during full illumination and idle + communication (8 min) in eclipse, [46].*

Case	ISS (400 km)				SSO (600 km)			
	Production	Consumption	Margin		Production	Consumption	Margin	
1	4.2 W	3.1 W	1.1 W	26.2 %	4.5 W	3.1 W	1.4 W	31.1 %
2	4.2 W	3.6 W	0.6 W	14.3 %	4.5 W	3.6 W	0.9 W	20 %
3	4.2 W	4.0 W	0.2 W	4.7 %	4.5 W	4.0 W	0.5 W	11.1 %
4	4.2 W	4.1 W	0.1 W	2.4 %	4.5 W	4.0 W	0.5 W	11.1 %

4.1.5 Configuration

The CubeSat is made by 3 standard units, each of them is typically 10 cm x 10 cm x 10 cm. Nevertheless a 3U CubeSat is usually a little bit bigger; for simplicity

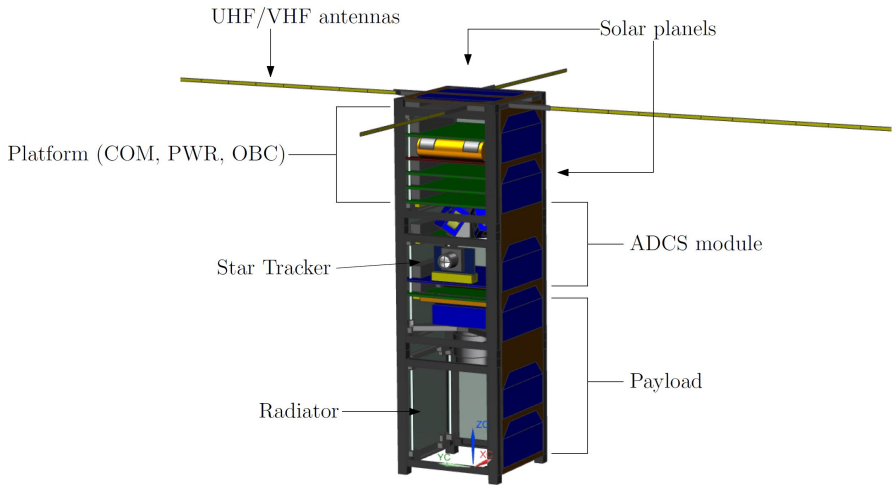

Figure 4.5: *The OUFTI-Next platform CAD model, [46], where PWR is refered to the Power Generation Subsystem and OBC to the On-Board COmputer. The reference frame indicated is different from the one used in this Thesis.*

the overall volume will be kept 10 cm x 10 cm x 30 cm.

Table 4.10: *ADCS subsystem inputs*

Mass (kg)	2-4
Platform dimension (CubeSat Units)	3
Payload volume (CubeSat Units)	1.5

A CAD drawing is presented in Figure 4.5. The center of mass is estimated to be +1.6 cm from the geometric center of the CubeSat. A preliminary mass budget is instead reported in Table 4.11, where PAY is refered to the Payload.

Table 4.11: *Preliminary mass budget, [46].*

Subsystem	Weight
ADCS	426.5 g
COM	295 g
EPS	686 g
OBC	94 g
STR	303 g
PAY	975 g
Total	2780.5 g

4.1.6 Payload

The payload is an Infrared camera, seen as a "black box" of 1.5U with the optics oriented in the -X face and located on the bottom of the platform. The remaining

part of the CubeSat is dedicated to the other subsystems, in particular the ADCS unit will be located almost in the middle of the platform. From the point of view of the pointing budget, a preliminary estimation was carried out in [46], Table 4.12, based on the work of other two master Thesis, [48] and [49].

Table 4.12: *Preliminary pointing budget*

Accuracy	0.1 deg (6 arcmin)
Stability	0.01 deg (0.5 arcmin)

4.1.7 Modes definition

The mission modes designed in in [46] can be summarized in Figure 4.6.

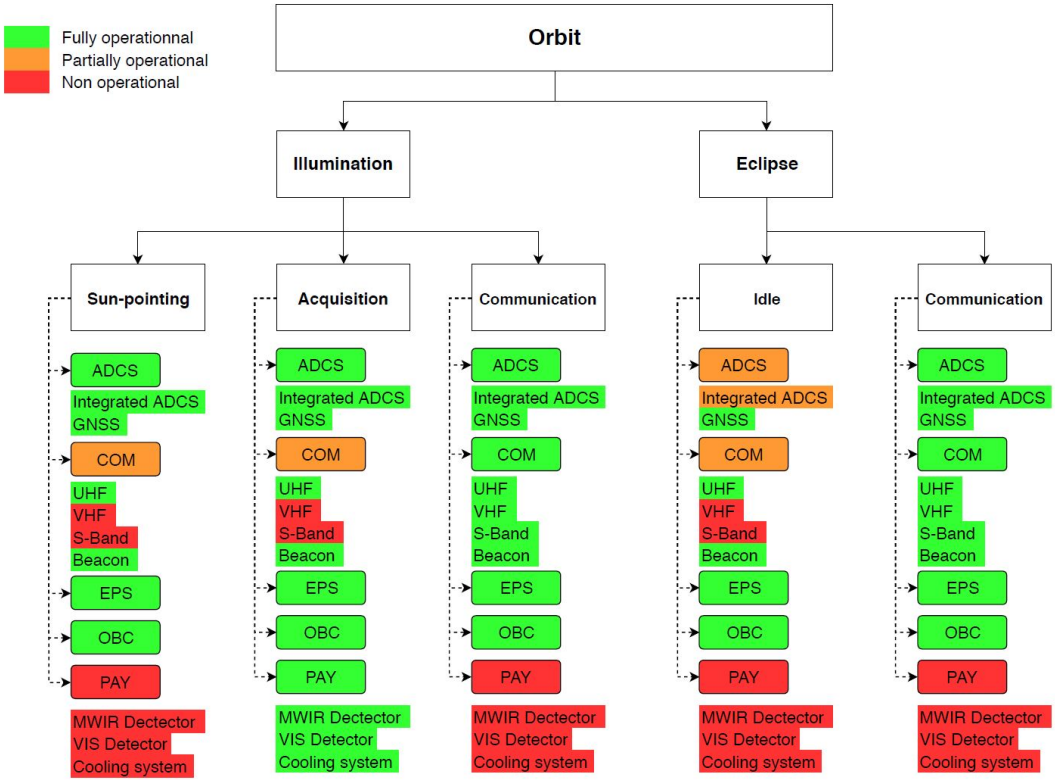

Figure 4.6: *The OUFTI-Next mission modes, [46]*

4.2 ADCS main input data

The decoupled ADCS simulator design is based on real actuators and sensors data, based on the *Hyperion iADCS100* unit characteristics [50]. This choice was done, since a preliminary trade-off among the ADCS units available on market was performed at University of Lieége [46], and it will be presented in Section 7.2. Here

the fundamental data obtained from *iADCS100* datasheet [50], and contacts with *Hyperion*, the company supplying this device, are reported:

- Maximum/minimum dipole moment of magnetic torquers: ± 0.4 Am^2.
- Maximum/minimum reaction wheels torque: ± 0.1 mNm.
- Maximum/minimum reaction wheels momentum storable: ± 6 mNms.
- Gyroscopes drift ramp: ≈ 18.5 deg/h.
- Gyroscopes standard deviation of the measurements: according to *Hyperion*, $\sigma_\epsilon \approx 10^{-4}$, while the drift rate ramp is equal to $\approx 9 \times 10^{-5}$ rad/s.
- Gyroscopes sampling time $\frac{1}{400 \text{ Hz}} = 0.0025$ s.
- The standard deviation of the star tracker measurements is 1.5×10^{-4} for the star tracker, according to its accuracy, and 10^{-4} for the gyroscopes according to *Hyperion*.

According to *Hyperion*, the accuracy of the gyroscopes is higher to the one characterizing the star tracker, which is the highest among sensors for the ADCS, and for this reason no multiplication times the accuracy matrix, $\boldsymbol{A_\epsilon}$ (Eq. (2.43)), is requested.

Then the remaining parameters were obtained from literature:

- ρ_a, the solar panels surface absorption coefficient, assumed ≈ 0.9203, [51].
- ρ_d, the solar panels surface diffusive coefficient, assumed ≈ 0.03, [51].
- ρ_s, the solar panels surface scattering coefficient, assumed ≈ 0.0727, [51].
- $\boldsymbol{m} = [5e^{-4},\ 5e^{-4},\ 5e^{-4}]$ Am^2, the residual dipole moment, from [52].

It is important to remark that Eq. (4.1) must be respected when selecting the proper optical coefficients for the platform surfaces:

$$\rho_a + \rho_s + \rho_d = 1 \tag{4.1}$$

It was assumed to have the coefficient referred to the solar panels also referred to all the faces of the satellite, since both the platforms that will be analysed are characterised by surfaces mostly covered by solar arrays and the optical properties of the remaining parts are not known yet. The star tracker used in *iADCS100* is the *ST-200*, Figure 4.7, whose characteristics are the following:

- Number of observable stars: 6.
- Accuracy: 30 arcsec.
- Update frequency: 5 Hz.

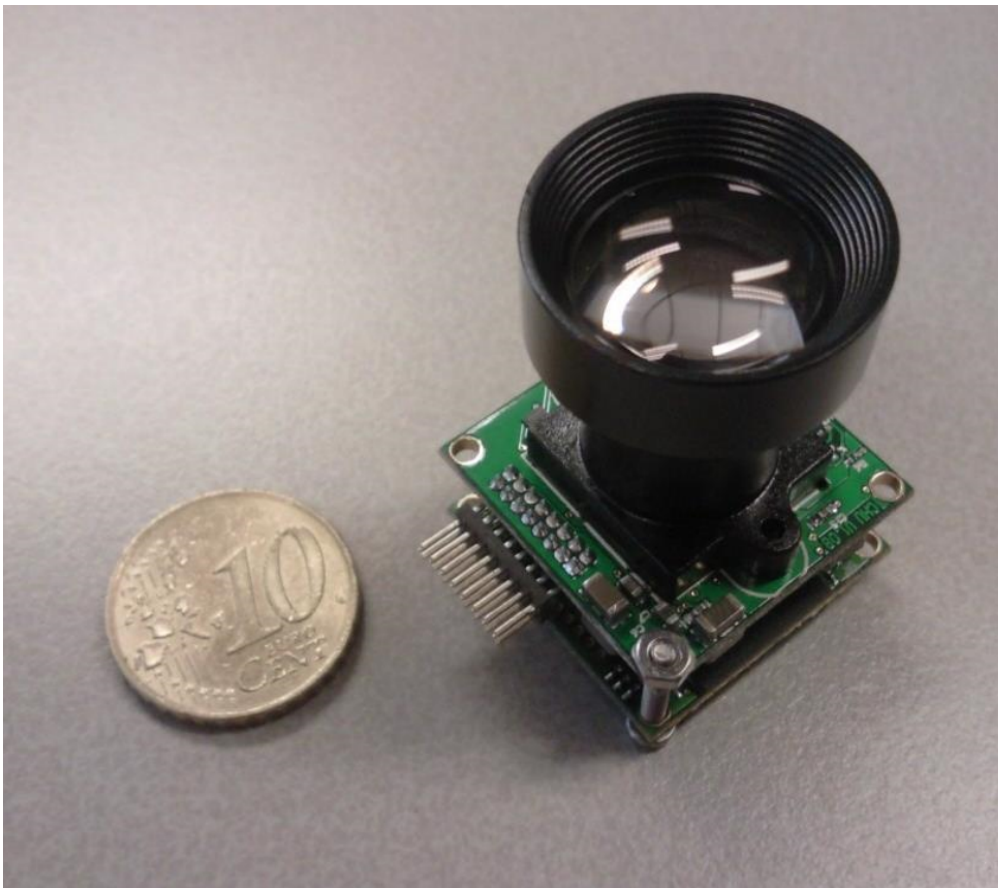

Figure 4.7: ST-200 *star tracker by* iADCS100*, [53].*

Usually a star tracker is not equally accurate along each axis: it is less accurate around the optical axis (when the star field rotates) and it is more accurate along the two axes perpendicular to it (when the star field translates). Nevertheless, according to *Hyperion* flyer [50], the accuracy declared is equal along the 3 axes. Other inputs for the subsystem are:

- $C_r = 1.6$, assuming solar panels surfaces almost always in Sun pointing [26].
- $C_d = 2.2$ [20]

4.3 Initial conditions

The initial velocities in rad/s depend on the mission phase:

- De-tumbling will be initiated with random initial conditions distribution centered in 0.5 rad/s
- If a simulation starts with a phase different from de-tumbling (like during nominal phases of the mission after having de-tumbled the spacecraft),

it will be initialised with random initial condition distribution centered in 10^{-3} rad/s.

- All the other phases will start after a previous one and, as a result, their initial conditions will be the final state of the previous phase.
- Quaternion initial condition: $\boldsymbol{q_0} = [1/\sqrt{3},\ 1/\sqrt{3},\ 1/\sqrt{3},\ 0]$ (unit quaternion).

CHAPTER 5

MISSION PROFILES IMPLEMENTATION

The following three representative missions profiles were implemented both for ISS orbit and SSO, with Nadir and target following picture acquisition strategies. All of them has as initial epoch: 01/01/2019 at 12:00:00 GMT+0.

Mission 1:

1. De-Tumbling.
2. Sun-Pointing for 24 hours.
3. Sun-Pointing till 30° from target.
4. De-Saturation phase.
5. Picture acquisition phase.
6. Sun-Pointing phase till 10° from Liége.
7. De-saturation phase.
8. Downloading phase (Nadir).

Mission 2:

1. Sun-Pointing for 24 hours.
2. Sun-Pointing till 30° from target.
3. De-Saturation phase.
4. Picture acquisition phase.
5. Sun-Pointing phase till 10° from Liége.
6. De-saturation phase.
7. Downloading phase (Nadir).

Mission 3:

1. De-Tumbling.
2. Sun-Pointing till saturation of the reaction wheels.
3. De-Saturation phase for 1 day.

Mission 1 was proposed in order to simulate a typical first operative mission after de-tumbling, while, instead, mission 2 was aimed to replicate a nominal mission scenario some time after the de-tumbling phase. Finally, mission 3 was intended to be exploited in order to obtain the maximum time in Sun-pointing before saturating the wheels and then to simulate what would happen during longer de-saturation phase, in terms of angular velocities: the behavior of the CubeSat can be useful to understand more in detail how much energy can be acquired by the solar panels even during de-saturation. Nevertheless, this topic will be investigated in future design steps of the OUFTI-Next project.

5.1 De-tumbling

Right after being released by the launcher, the CubeSat is *tumbling*, meaning that it is spinning very fast around its axes. The first phase of a spacecraft operational life is the *de-tumbling phase*. During this phase the only actuators exploited are the magnetic torquers commanded by a control law, function of the Earth magnetic field.
The most common and Lyapunov stable law is called *B-dot law*, since it is based on the derivative of the magnetic field experienced by the CubeSat in body-frame, $\boldsymbol{B_b}$, [54]:

$$\boldsymbol{m} = -k_{DeT}\dot{\boldsymbol{B}}_{\boldsymbol{b}} \tag{5.1}$$

$$\boldsymbol{u} = \boldsymbol{m} \times \boldsymbol{B_b} \tag{5.2}$$

where k_{DeT} is a positive constant and $\boldsymbol{m}$ the dipole moment requested, which will be compared to the available one and eventually saturated if it will exceed it.

Nevertheless, this law is based on the derivative of the magnetic field in body frame, $\dot{\boldsymbol{B}}_{\boldsymbol{b}}$, which is a quite expensive quantity to be evaluated from the computational point of view. In order to obtain it, the previous step $\boldsymbol{A}_{\boldsymbol{b/n}}$ is requested, in order to find an approximate value of $\dot{\boldsymbol{B}}_{\boldsymbol{b}}$, using *finite differences* [55]:

$$\boldsymbol{B}_{\boldsymbol{b}} = \boldsymbol{A}_{\boldsymbol{b/n}} \boldsymbol{B}_{\boldsymbol{n}} \tag{5.3}$$

$$\dot{\boldsymbol{B}}_{\boldsymbol{b}} = \frac{\boldsymbol{B}_{\boldsymbol{b}}(t) - \boldsymbol{B}_{\boldsymbol{b}}(t-\tau)}{\tau} \tag{5.4}$$

This procedure is really difficult to be implemented in Matlab$^{\text{TM}}$without increasing dramatically the computational time. For this reason it was decided to implement the de-tumbling phase in Simulink$^{\text{TM}}$, where it is possible to exploit *delay blocks* in order to retrieve previous values of $\boldsymbol{B}_{\boldsymbol{b}}$.

The constant k_{DeT} can be changed in order to modify the de-tumbling behavior and it can be also optimised in order to minimise the de-tumbling time. Nevertheless, the computational time requested to perform an optimisation procedure is too long and a possible development of this work could be the simplification of the algorithm, allowing the constant to be optimised in reasonable time. All the simulations presented in this Thesis were performed with $k_{DeT} = 10^5$.
For what concerns the de-tumbled condition, fundamental to stop this phase and start the following one, initially it was thought to use an angular velocity threshold: if the OUFTI-Next platform maximum angular rate was below this value for a certain amount of time, the CubeSat was supposed to be de-tumbled. Then, looking at different de-tumbling simulations, it appeared clear that the spacecraft could in any case de-tumble in less than 5000 s and then maintains an almost periodic behavior, independently from initial tumbling conditions. For this reason, all the de-tumbling simulations will end after 1 h40 min.

During this phase no determination algorithm nor sensors models were implemented, relaying only on the integrated state, since the spacecraft would rotate too fast for the star tracker to be used and the magnetometers/gyroscopes models would slow down the simulation time too much. The results are quite robust with respect to the initial tumbling velocity, since the simulation was initiated with random initial condition distribution centered in 0.5 rad/s. Nevertheless, this phase is also deeply dependent on:

- Residual dipole moment.

- Atmosphere condition at launch epoch.
- Solar activity at launch epoch.
- Season at launch epoch.

For this reason all the results presented about this phase are to be intended qualitatively more than quantitatively.

5.1.1 Magnetic field approximated model

In order to reduce the computational time of this simulation, an approximated model for the Earth magnetic field was implemented, based on the Schmidt quasi-normalized associated Legendre Polynomial [31]:

$$\boldsymbol{B} = -\boldsymbol{\nabla} V \tag{5.5}$$

with:

$$V(r, \tilde{\theta}, \tilde{\phi}) = R_e \sum_{n=1}^{k} \left(\frac{R_e}{r} \right)^{n+1} \sum_{m=0}^{n} (g_n^m cos(m\tilde{\phi}) + h_n^m sin(m\tilde{\phi})) P_n^m(\tilde{\theta}) \tag{5.6}$$

$$B_r = \sum_{n=1}^{k} \left(\frac{R_e}{r} \right)^{n+2} (n+1) \sum_{m=0}^{n} (g_n^m cos(m\tilde{\phi}) + h_n^m sin(m\tilde{\phi})) \frac{\partial P_n^m(\tilde{\theta})}{\partial \tilde{\theta}} \tag{5.7}$$

$$B_{\tilde{\theta}} = -\sum_{n=1}^{k} \left(\frac{R_e}{r} \right)^{n+2} \sum_{m=0}^{n} (g_n^m cos(m\tilde{\phi}) + h_n^m sin(m\tilde{\phi})) P_n^m(\tilde{\theta}) \tag{5.8}$$

$$B_{\tilde{\phi}} = -\frac{1}{sin(\tilde{\theta})} \sum_{n=1}^{k} \left(\frac{R_e}{r} \right)^{n+2} (n+1) \sum_{m=0}^{n} (-g_n^m sin(m\tilde{\phi}) + h_n^m cos(m\tilde{\phi})) P_n^m(\tilde{\theta}) \tag{5.9}$$

where:

- R_e is the Earth mean radius.
- r is the CubeSat position vector.
- $\tilde{\theta}$ is the latitude measured in degrees positive from the equator (input from orbit model).

- $\tilde{\phi}$ is the Earth fixed longitude measured in degrees positive from the equator (input from orbit model).
- g_n^m and h_n^m are the tabulated Gaussian coefficients in Tesla (T).
- P_n^m is the Schmidt quasi-normalized associated Legendre Polynomial.
- The model is expanded till order 9 ($n,\ m = 1, \dots 9$).

Once obtained $B_r, B_{\tilde{\theta}}$ and $B_{\tilde{\phi}}$, $\boldsymbol{B_n}$ in inertial frame can be evaluated:

$$B_{n1} = (B_r cos(\tilde{\theta}) + B_{\tilde{\theta}} sin(\tilde{\theta}))cos(\tilde{\alpha}) - B_{\tilde{\phi}} sin(\tilde{\alpha}) \tag{5.10}$$

$$B_{n2} = (B_r cos(\tilde{\theta}) + B_{\tilde{\theta}} sin(\tilde{\theta}))sin(\tilde{\alpha}) + B_{\tilde{\phi}} cos(\tilde{\alpha}) \tag{5.11}$$

$$B_{n3} = (B_r sin(\tilde{\theta}) - B_{\tilde{\theta}} cos(\tilde{\theta})) \tag{5.12}$$

where $\tilde{\alpha}$ is the longitude measured in degrees positive from the equator. Finally the Earth magnetic field vector must be transported in body frame:

$$\boldsymbol{B_b} = \boldsymbol{A_{b/n}} \boldsymbol{B_n} \tag{5.13}$$

5.2 Pointing phases

Every pointing phase is characterised by the evaluation of a target reference frame matrix, $\boldsymbol{A_t}$, which is different in each phase.
Since no precise target has been identified yet, it was decided to simulate picture acquisition of the Brasilia National Park, because it is near to the possible zone of interest and is characterised by similar environmental characteristics.

5.2.1 Sun-pointing

During Sun-pointing phase it was decided to take the CubeSat at 45° inclination with respect to the Sun with the two surfaces covered by solar panels (Z and Y, according to the ADCS reference frame, Figure 4.2) and not also tilted as reported in [46], because it was preferred to maintain the target attitude simple. The actuators used during this phase are only the 3 reaction wheels, with the

following target attitude matrix:

$$\boldsymbol{A_t} = \begin{bmatrix} \hat{\boldsymbol{x}}_{\boldsymbol{p}} \\ \hat{\boldsymbol{y}}_{\boldsymbol{p}} \\ \hat{\boldsymbol{z}}_{\boldsymbol{p}} \end{bmatrix} = \begin{bmatrix} \hat{\boldsymbol{y}}_{\boldsymbol{p}} \times \hat{\boldsymbol{r}}_{\boldsymbol{Sun}} \\ \boldsymbol{R_r}\hat{\boldsymbol{r}}_{\boldsymbol{Sun}} \\ \hat{\boldsymbol{x}}_{\boldsymbol{p}} \times \hat{\boldsymbol{y}}_{\boldsymbol{p}} \end{bmatrix} \tag{5.14}$$

where $\boldsymbol{r_{Sun}}$ is the platform-Sun direction and $\boldsymbol{R_r}$ is a rotational matrix:

$$\boldsymbol{R_r} = \begin{bmatrix} cos(-\frac{\pi}{4}) & -sin(-\frac{\pi}{4}) & 0 \\ sin(-\frac{\pi}{4}) & cos(-\frac{\pi}{4}) & 0 \\ 0 & 0 & 1 \end{bmatrix} \tag{5.15}$$

In this way the Sun direction is rotated of 45° around the X-axis, allowing both the surfaces covered by solar cells to be in light.

The target angular velocity, $\boldsymbol{\omega_t}$, is null, since the CubeSat-Sun direction is almost fixed for the time intervals considered in these simulations.

As it will be shown in Chapter 6, the pointing accuracy reached during this phase is less than 0.1°. Nevertheless, the Sun direction unit vector is assumed to be known from ephemeris, previously evaluated; in a real scenario, this datum would be obtained from the Sun sensors. According to *Hyperion*, their unit (*iADCS100*) is not equipped with any of them, but it has interfaces for up to six of these devices. As a result, in the case it will be decided to use their unit, there will be two options: Sun sensors should be bought separately from the ADCS unit, or the ADCS will have to relay on the coarser Sun sensors integrated on the solar panels. In this last case, the accuracy is approximately ±10°, meaning that the final pointing error will be less than 1°, which is an acceptable value during Sun-pointing phase.

Nadir pointing picture acquisition The easiest way to shoot pictures to the target is to pass over it pointing the Nadir direction. This is not the best option, since it is mandatory to have the orbital plane normal almost orthogonal to the target location in ECI frame, meaning that the spacecraft is actually orbiting right above the spot to be observed. This limits the number of pictures it is possible to shoot over the same place per unit time, especially for the ISS orbit, which has a long revisit time.
The actuators used during this phase are only the 3 reaction wheels, with the

following target attitude matrix:

$$\boldsymbol{A_t} = \begin{bmatrix} \hat{\boldsymbol{x}}_{\boldsymbol{p}} \\ \hat{\boldsymbol{y}}_{\boldsymbol{p}} \\ \hat{\boldsymbol{z}}_{\boldsymbol{p}} \end{bmatrix} = \begin{bmatrix} \hat{\boldsymbol{r}} \\ \hat{\boldsymbol{h}}_{\boldsymbol{m}} \times \hat{\boldsymbol{x}}_{\boldsymbol{p}} \\ \hat{\boldsymbol{x}}_{\boldsymbol{p}} \times \hat{\boldsymbol{y}}_{\boldsymbol{p}} \end{bmatrix} \tag{5.16}$$

where: $\hat{\boldsymbol{r}}$ is the position unit vector and $\hat{\boldsymbol{h}}_{\boldsymbol{m}}$ the angular momentum unit vector. In this way the spacecraft is pointing with the $-X$-axis to the ground, while the Y-axis is pointed in the same direction of the velocity vector.

The target angular velocity is $\boldsymbol{\omega_t} = [0 \;\; 0 \;\; \omega_{orbit}]$ since the CubeSat rotates around its Z-axis with the angular rate it has on orbit.

Target following picture acquisition The most peculiar phase is the target following picture acquisition, based on a slew manoeuvre performed in order to follow the target during the passage, to increase the exposition time and allow the orbital momentum vector to be slightly less or more 90° inclined with respect to the target position in ECI reference frame. This decreases the revisit time, even if for the ISS orbit, the effect is almost negligible, [46].
The actuators used during this phase are only the three reaction wheels, with the following target attitude matrix:

$$\boldsymbol{A_t} = \begin{bmatrix} \hat{\boldsymbol{x}}_{\boldsymbol{p}} \\ \hat{\boldsymbol{y}}_{\boldsymbol{p}} \\ \hat{\boldsymbol{z}}_{\boldsymbol{p}} \end{bmatrix} = \begin{bmatrix} \hat{\boldsymbol{r}}_{\boldsymbol{diff}} \\ \hat{\boldsymbol{z}}_{\boldsymbol{p}} \times \hat{\boldsymbol{x}}_{\boldsymbol{p}} \\ \hat{\boldsymbol{x}}_{\boldsymbol{p}} \times \hat{\boldsymbol{v}} \end{bmatrix} \tag{5.17}$$

where: $\hat{\boldsymbol{v}}$ is the velocity unit vector and $\hat{\boldsymbol{r}}_{\boldsymbol{diff}}$ the unit vector obtained from the difference between the position unit vector and the target location unit vector in ECI reference frame:

$$\hat{\boldsymbol{r}}_{\boldsymbol{diff}} = \frac{\boldsymbol{r} - \boldsymbol{r}_{\boldsymbol{l,ECI}}}{||\boldsymbol{r} - \boldsymbol{r}_{\boldsymbol{l,ECI}}||} \tag{5.18}$$

The target angular velocity is obtained solving the expression of the target reference frame dynamics with respect to $\boldsymbol{\omega_t}$:

$$\dot{\boldsymbol{A}}_{\boldsymbol{t}} = \boldsymbol{S}(\boldsymbol{\omega}_t)\boldsymbol{A}_{\boldsymbol{t}} \tag{5.19}$$

In order to differentiate $\dot{\boldsymbol{A}}_{\boldsymbol{d}}$, the finite difference technique was exploited:

$$\dot{\boldsymbol{A}}_{\boldsymbol{t}} = \frac{\boldsymbol{A_t}(t) - \boldsymbol{A_t}(t-\tau)}{\tau} \tag{5.20}$$

with $\tau = 0.001$ s.

5.2.2 Downloading

This phase is very similar to the Nadir pointing picture acquisition one, since it is based on Nadir pointing, as well. The only difference is that the surface Nadir pointing is the one with normal $-Z$. The S-band antenna field of view has not been selected yet, but it is supposed to be reasonably large enough to be compatible with a nadir pointing downloading strategy.
The actuators used during this phase are only the three reaction wheels, with the following target attitude matrix:

$$\boldsymbol{A_t} = \begin{bmatrix} \hat{\boldsymbol{x}}_{\boldsymbol{p}} \\ \hat{\boldsymbol{y}}_{\boldsymbol{p}} \\ \hat{\boldsymbol{z}}_{\boldsymbol{p}} \end{bmatrix} = \begin{bmatrix} \hat{\boldsymbol{y}}_{\boldsymbol{p}} \times \hat{\boldsymbol{z}}_{\boldsymbol{p}} \\ \hat{\boldsymbol{z}}_{\boldsymbol{p}} \times \hat{\boldsymbol{h}} \\ \hat{\boldsymbol{r}} \end{bmatrix} \tag{5.21}$$

In this way the spacecraft is pointing with the -Z-axis to the ground, while the Y-axis is oriented along the velocity vector.
The target angular velocity is $\boldsymbol{\omega_t} = [\omega_{orbit} \;\; 0 \;\; 0]$ since the CubeSat rotates around its X-axis with the angular rate it has on orbit.

5.3 De-saturation

De-saturation phase is required when the reaction wheels have reached their maximum momentum storable. During this phase they are switched off and the magnetic torquers are activated with a less precise and computationally demanding law with respect to the de-tumbling one, whose Lyapunov stability is proven in [54]:

$$\boldsymbol{m} = -\frac{1}{||\boldsymbol{B_b}||^2}\boldsymbol{S}(\boldsymbol{B_b})\boldsymbol{\omega} \tag{5.22}$$

$$\boldsymbol{u} = \boldsymbol{m} \times \boldsymbol{B_b} \tag{5.23}$$

where $\boldsymbol{m}$ is the dipole moment requested, function of the cross product between $\boldsymbol{B_b}$ and $\boldsymbol{\omega}$, which will be compared to the available one and eventually saturated if it will exceed it.
In this way the evaluation of $\dot{\boldsymbol{B}}_{\boldsymbol{b}}$ is avoided and the law assumes a less complex expression.

5.4 Control parameters optimization

The decision to implement the simulator mostly in Matlab™ was based on the fact that it is easier to optimize each phase (but the de-tumbling one, due to high computational time) using a global optimisator, such as *ga.m*, the genetic algorithm, and exploiting the build-in Parallel Computing Toolbox™.
The optimised parameters are the 2 constants of the PD controller, K_p and K_d. The first step is to separate between picture acquisition phases and the other ones, since the cost functions are based on different logics:

5.4.1 Picture acquisition phases

During this phases the pointing error shall be minimised, without taking care about the momentum stored inside the wheels. For this reason a single objective global optimisation, using *ga.m*, was performed, with the following cost function:

$$J = \int_{t_0}^{t_f} (pointing\ error - 0.1)^2 \, \mathrm{d}t. \tag{5.24}$$

which is based on the pointing accuracy requested, 0.1° and squared to smooth the function. It is important to remark that only the last 30% of the period between t_0 and t_f was considered inside J, in order not to consider the transient phase.
The optimisation tolerance was set to 10^{-3}, while the absolute and relative tolerances of the model were set to 10^{-6} and the initial conditions are generated with a random distribution around 10^{-3} rad/s, in order to increase the generality.

All the optimisation algorithms were run in parallel on 4 physical cores of the CPU and the optimisation time is strictly related to the integration initial condition (random, with Gaussian distribution). For this reason the values reported in the following tables, concerning the computational time, can vary depending on them.

In Table 5.1 the results obtained for picture acquisition phases are summarized:

Table 5.1: *Optimised control parameters for all picture acquisition phases.*

Processor used: Intel™Core ™i7-7700HQ CPU @2.80 GHz RAM 16GB

Orbit	K_p	K_d	**CPU time (hours)**
-ISS- Nadir pointing	0.0601	0.4986	0.67
-ISS- Target following	0.0429	0.4963	9.8
-SSO- Nadir pointing	0.1420	0.9221	0.5
-SSO- Target following	0.0443	0.3561	12

5.4.2 Sun-pointing and downloading phases

The remaining phases are characterised by the necessity to reduce the momentum stored by the reaction wheel, maintaining the pointing error less than 1°. For this reason a multi-objective optimisation is requested. In order to perform it, the Matlab™ algorithm *gamultiobj.m*, based on a Pareto front optimisation, was exploited. The output of this function is the Pareto front, a set of optima, plotted on a graph with x-axis and y-axis characterised respectively by the first and the second cost functions. For what concerns them, two sets of two cost functions were used and then the solutions obtained were compared to establish which one provides the best dynamics:
The first set provides only one optimum:

$$\begin{cases} J1 = \int_{t_0}^{t_f} (pointing\ error - 0.1)^2 \, \mathrm{d}t. \\ J2 = \int_{t_0}^{t_f} (momentum\ stored)^2 \, \mathrm{d}t. \end{cases} \tag{5.25}$$

While the second set, based on the final value of the stored momentum instead of its integral, provides a classical Pareto front:

$$\begin{cases} J1 = \int_{t_0}^{t_f} (pointing\ error - 0.1)^2 \, \mathrm{d}t. \\ J2 = \frac{(|momentum\ \ stored_{f,1}| + |momentum\ \ stored_{f,2}| + |momentum\ \ stored_{f,3}|)}{||momentum\ \ stored_f||} \end{cases} \tag{5.26}$$

Once the solutions are obtained, the one closest to the bisector of the Pareto front plot is selected as the best one, minimising almost equally both cost functions.
Finally this solution is compared to the one of the first set and the best one will be inserted inside the model.
The results obtained for the Sun-pointing phase are reported in Table 5.2 and 5.3 respectively.

Table 5.2: *optimised control parameters for all the Sun-pointing phases.*

Orbit	K_p	K_d
ISS	0.0593	0.3410
SSO	0.0319	0.3517

Table 5.3: *Optimised control parameters for all the downloading phases.*

Orbit	K_p	K_d
ISS	0.0319	0.3517
SSO	0.0319	0.3517

CHAPTER 6

SIMULATIONS RESULTS

In this chapter the main results, subdivided per mission and phase are presented and commented. Mission 2 results are not reported, since they are almost equal to the ones of mission 1. Moreover, the results on SSO are described in Appendix B, since they are quite similar to the ones on ISS orbit, with the exception of the disturbances order of magnitude.
It was decided to report the majority of the results, instead of selecting only some phases, just to let the reader and who will carry on this project to have a collection of results representing the nominal behavior for complete missions, both in ISS and SSO (in Appendix B), which can be used as benchmark or for comparison with future results. Moreover, in this chapter and the correspondent Appendix, the symbol e indicates the pointing error and not the orbital eccentricity.

6.1 Mission 1 with Nadir pointing

Computational time usually requested: around 3 minutes, depending on the initial conditions.

De-tumbling After the de-tumbling phase, the angular velocities reached are:

$$\begin{cases} \omega_{b/n,1}(5000) = 7.189 \times 10^{-3} \text{ rad/s} \\ \omega_{b/n,2}(5000) = 2.150 \times 10^{-3} \text{ rad/s} \\ \omega_{b/n,3}(5000) = -5.367 \times 10^{-3} \text{ rad/s} \end{cases} \tag{6.1}$$

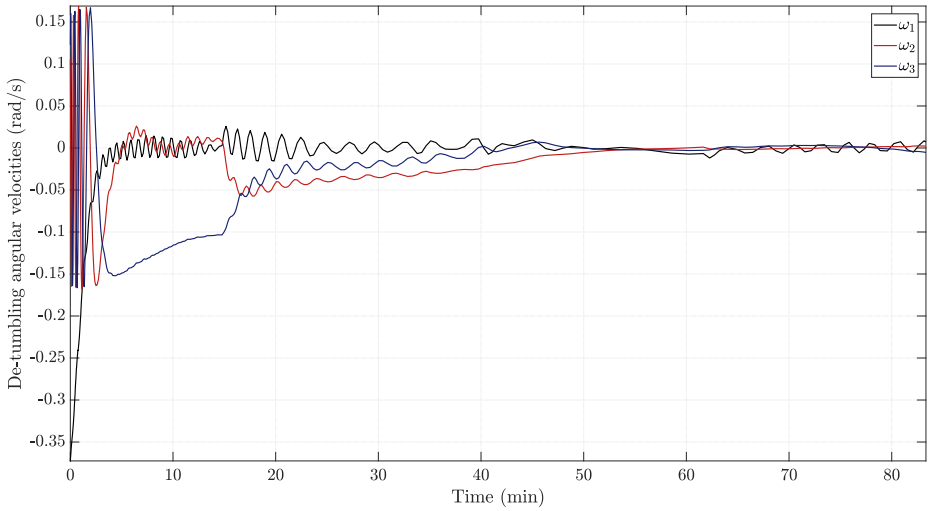

Figure 6.1: *Angular velocities reduction during de-tumbling phase, in mission 1, on ISS orbit.*

The disturbances experienced by the OUFTI-Next CubeSat are instead represented in Figure 6.2.

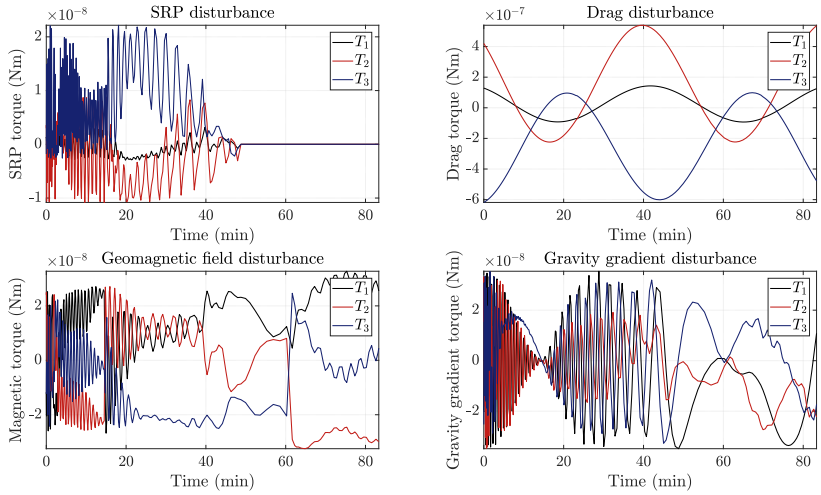

Figure 6.2: *Main disturbances during de-tumbling phase, in mission 1, on ISS orbit. T_i are the torques components in body-fixed reference frame.*

The solver relative tolerances was set to 10^{-3} just to speed up the simulation, since no lack of accuracy in the solution was evidenced.

Sun-pointing 1 From Figure 6.3 it possible to appreciate that the star tracker based algebric determination algorithm works very well in estimating the attitude. The phase lasts around 74 hours, 24 hours plus the time spent in orbit before arriving 30° from the National Park of Brasilia, and the solver absolute and relative tolerances were set to 10^{-6} both. The steady state is reached after around 100 seconds. Quaternions plots, shown in Figure 6.3, evidences a peculiar behavior: the estimated quaternions by the determination algorithm are the opposite of the actual ones. This is due to the quaternion normalization procedure, during state estimation, providing in some simulations the opposite of the integrated quaternion, but this is not altering the dynamics, since quaternions are not unique and even if they are the opposite, they represent the same rotation in space. Moreover, using the square control law, Eq. (2.83) reported in Section 2.9, it does not affect at all the control action. This behavior is present also in following simulations. From Figure 6.3 it is also possible to notice that the control executed

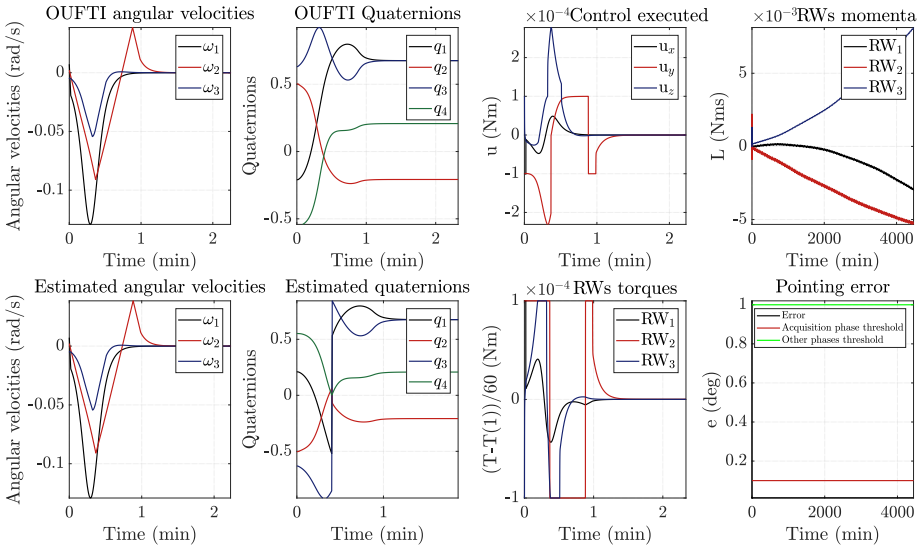

Figure 6.3: *Most important results during Sun-pointing phase 1, in mission 1, on ISS orbit. The plots are zoomed in order to catch the most interesting behaviors.*

and the torque provided by the reaction wheels is not the same and the behavior is almost the opposite. This is due to the fact that the actual control is provided only partially by the derivative of the reaction wheel momentum, $\dot{\boldsymbol{h}}_{\boldsymbol{r}}$, represented in Figure 6.3. The complete formulation, Eq. (2.84), is here recalled:

$$\boldsymbol{u} = \boldsymbol{A}\boldsymbol{h}_{\boldsymbol{r}} \times \boldsymbol{\omega} - \boldsymbol{A}\dot{\boldsymbol{h}}_{\boldsymbol{r}} \tag{6.2}$$

and, as a consequence of the minus sign, the two behaviors are the opposite. In Figure 6.4 is possible to observe that the results in terms of disturbances are consistent with respect to the one obtained with Simulink^{TM}, shown in Figure 6.2.

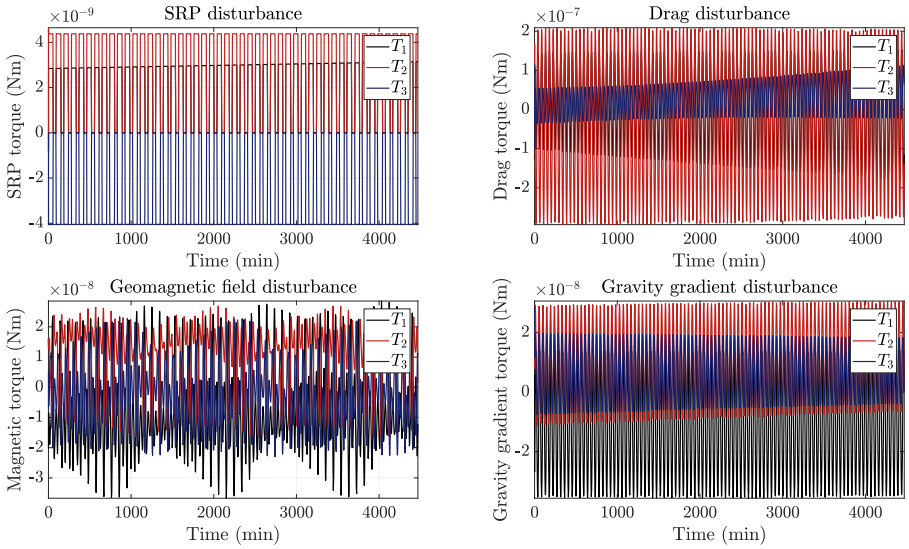

Figure 6.4: *Main disturbances torques during Sun-pointing phase 1, in mission 1, on ISS orbit. T_i are the torques components in body-fixed reference frame.*

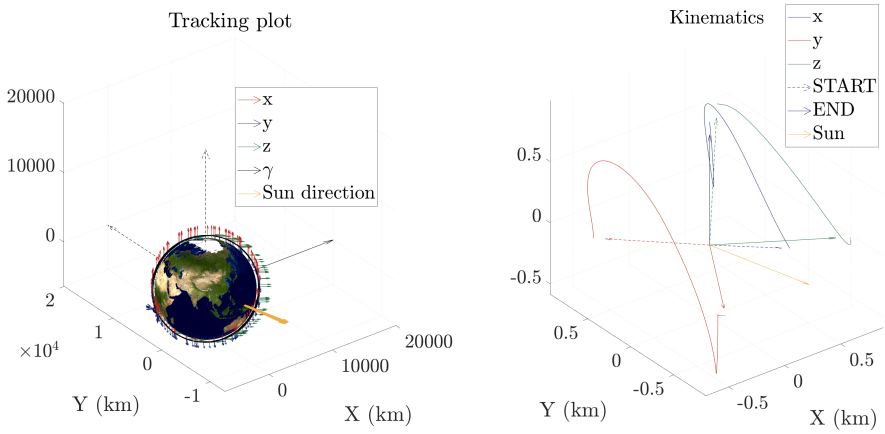

Figure 6.5: *Body-fixed frame while orbiting around the earth during Sun-pointing phase 1, in mission 1, on ISS orbit.*

De-saturation 1 From Figure 6.6 it is clear that the angular velocities during de-saturation phase do not spread so much, making the spacecraft rotate very slowly.

The phase lasts 1 minute and the solver absolute and relative tolerances were set to 10^{-6} both.

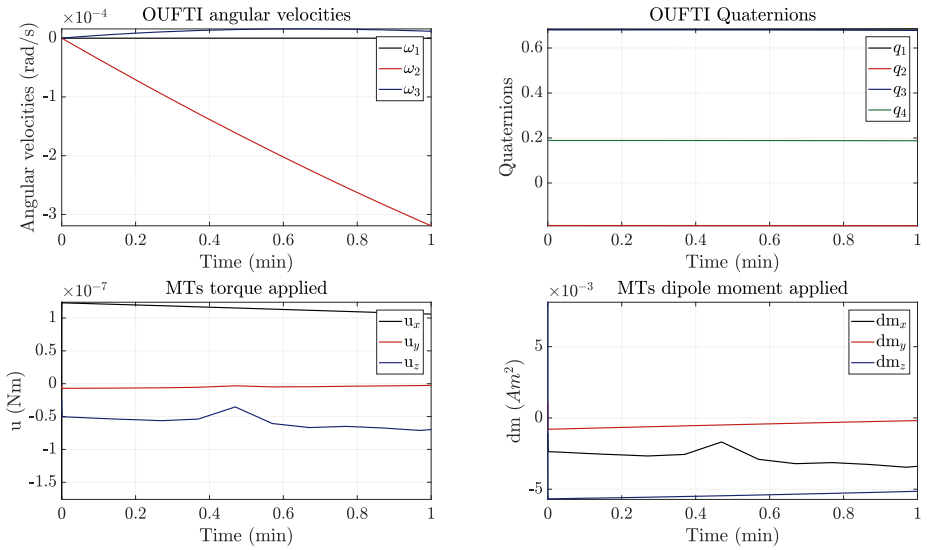

Figure 6.6: *Most important results during de-saturation phase 1, in mission 1, on ISS orbit.*

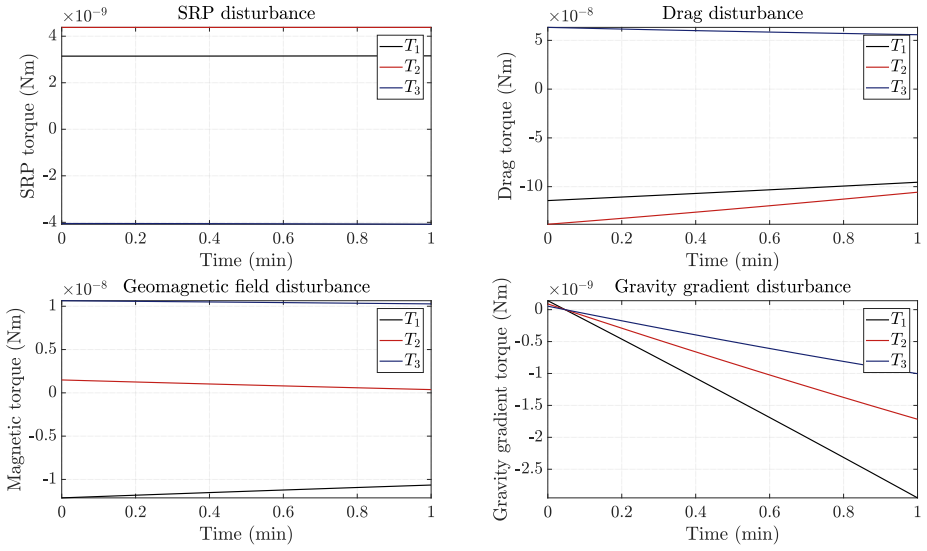

Figure 6.7: *Main disturbances torques during de-saturation phase 1, in mission 1, on ISS orbit. T_i are the torques components in body-fixed reference frame.*

Picture acquisition The picture acquisition phase is the one with most stringent pointing requirements, but, as shown in Figure 6.8, the control action is able to maintain the pointing error below the 0.1° threshold, thanks to the optimisation of control parameters.

The phase lasts around 15 minutes and the solver absolute and relative tolerances were set to 10^{-6} both. The steady state is reached in less than 100 s.

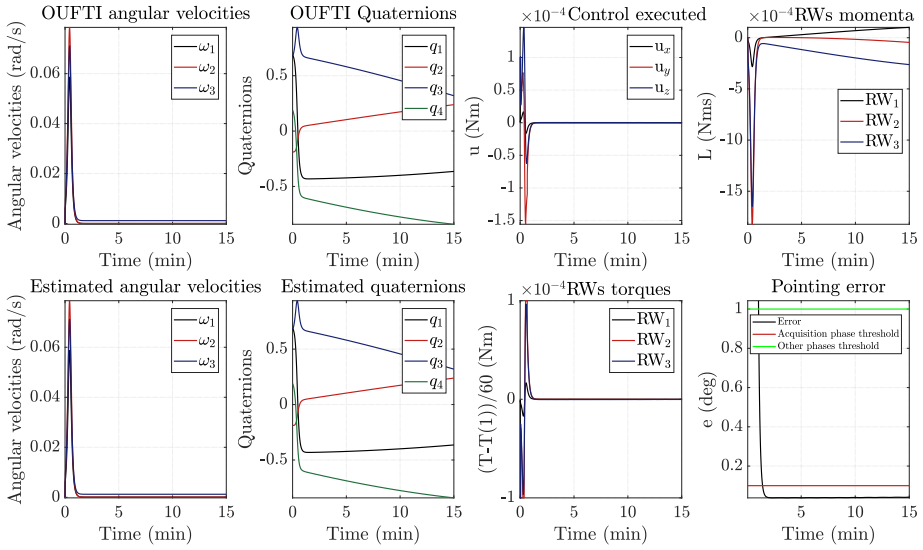

Figure 6.8: *Most important results during Nadir pointing picture acquisition phase, in mission 1, on ISS orbit. The plots are zoomed in order to catch the most interesting behaviors.*

From Figure 6.8 it is also possible to appreciate how well *the unscented Kalman filter* estimates the state, comparing the integrated angular velocities and quaternion plots with the ones provided by the gyroscopes/star trackers and estimated by the filter.

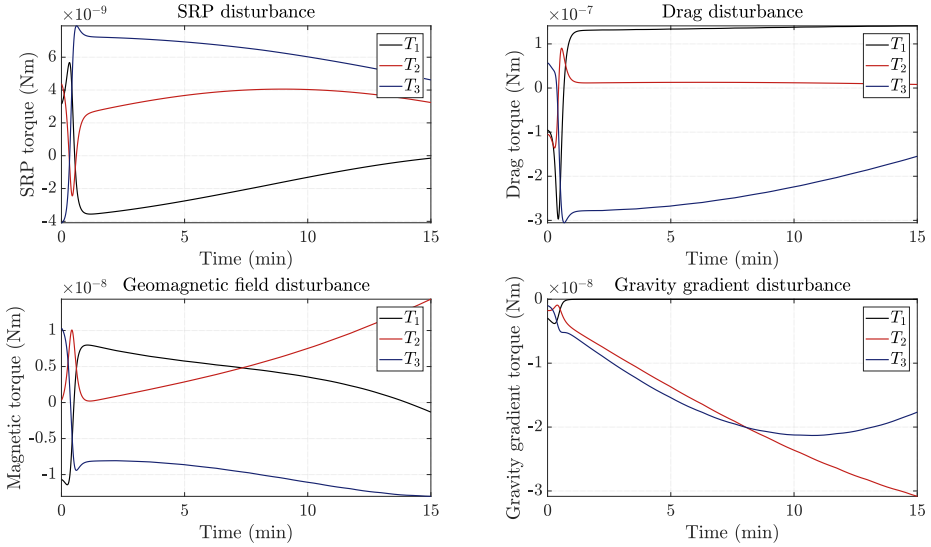

Figure 6.9: *Main disturbances torques during Nadir pointing picture acquisition phase, in mission 1, on ISS orbit. T_i are the torques components in body-fixed reference frame.*

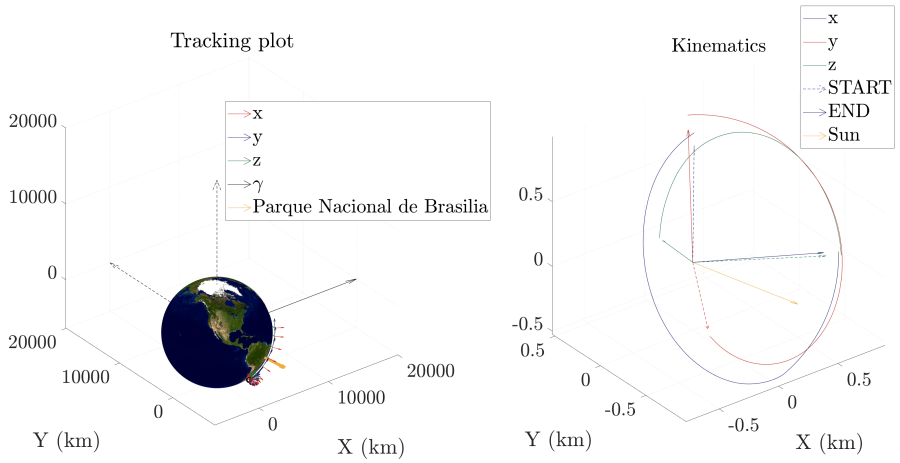

Figure 6.10: *Body-fixed frame while orbiting around the earth during Nadir pointing picture acquisition phase, in mission 1, on ISS orbit.*

Sun-pointing 2 This phase is quite similar to the previous one in Sun-pointing. The phase lasts less than 2 hours, the time needed to reach 10° from Liége, and the solver absolute and relative tolerances were set to 10^{-6} both. The steady state is reached after around 100 seconds.

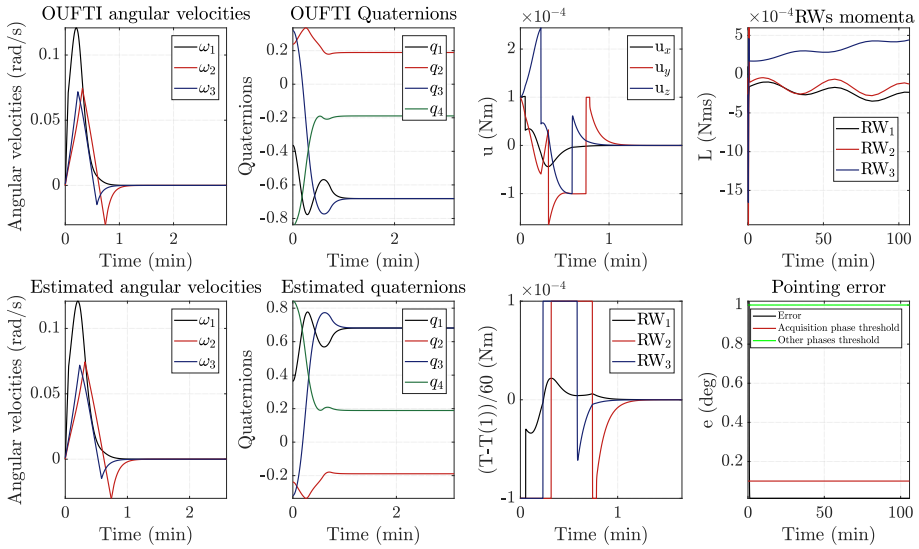

Figure 6.11: *Most important results during Sun-pointing phase 2, in mission 1, on ISS orbit. The plots are zoomed in order to catch the most interesting behaviors.*

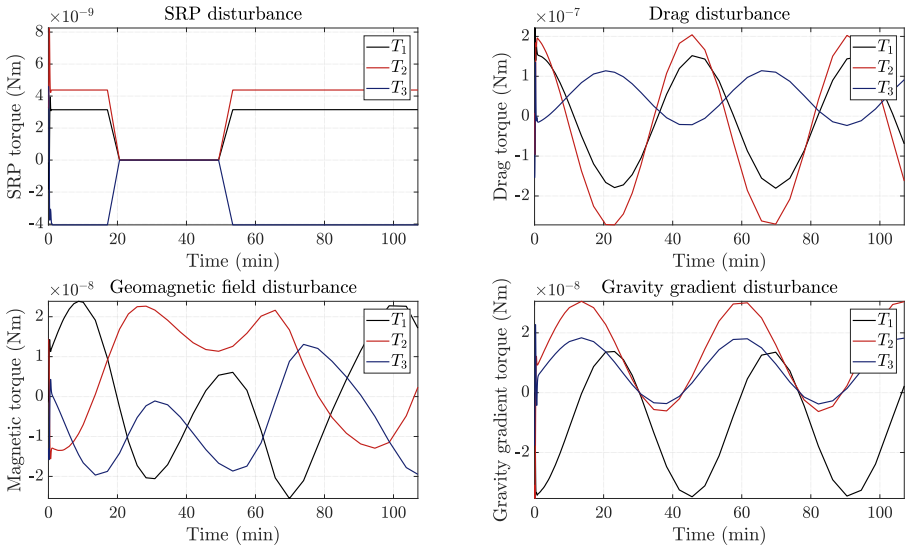

Figure 6.12: *Main disturbances torques during Sun-pointing phase 2, in mission 1, on ISS orbit. T_i are the torques components in body-fixed reference frame.*

De-saturation 2 This results are quite similar to the ones of the previous de-saturation phase and confirm that the spacecraft rotates very slowly and does not tumble. The phase lasts 1 minute and the solver absolute and relative tolerances were set to 10^{-6} both.

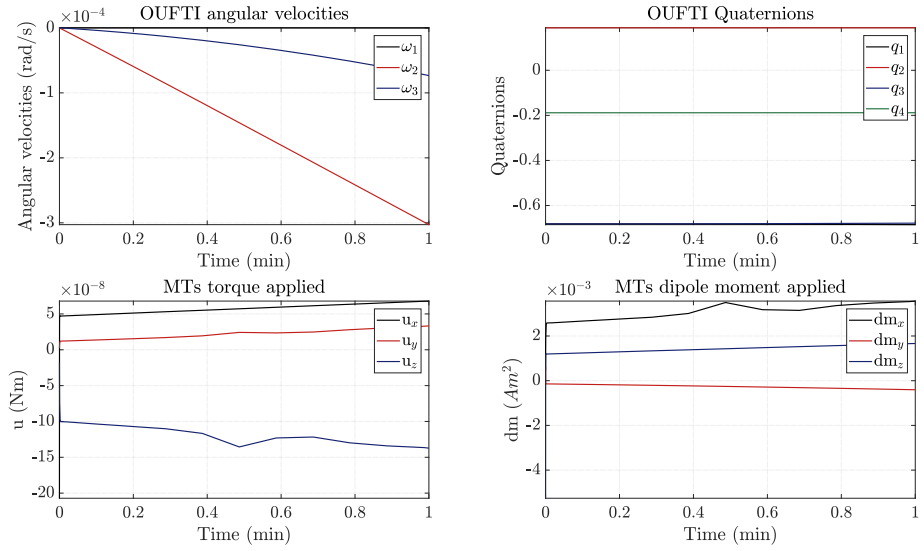

Figure 6.13: *Most important results during de-saturation phase 2, in mission 1, on ISS orbit.*

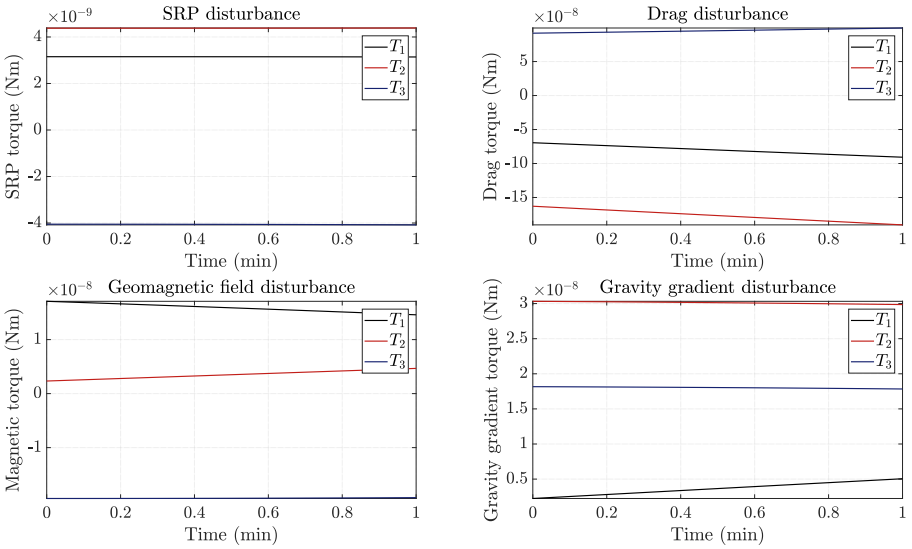

Figure 6.14: *Main disturbances torques during de-saturation phase 2, in mission 1, on ISS orbit. T_i are the torques components in body-fixed reference frame.*

Downloading Downloading phase above Liége lasts 5 minutes and the solver absolute and relative tolerances were set to 10^{-6} both. The steady state is reached after around 2 minutes.
From Figure 6.15 it is evident the peculiar behavior of the estimated quaternions, already mentioned in Sun-pointing phase 1.

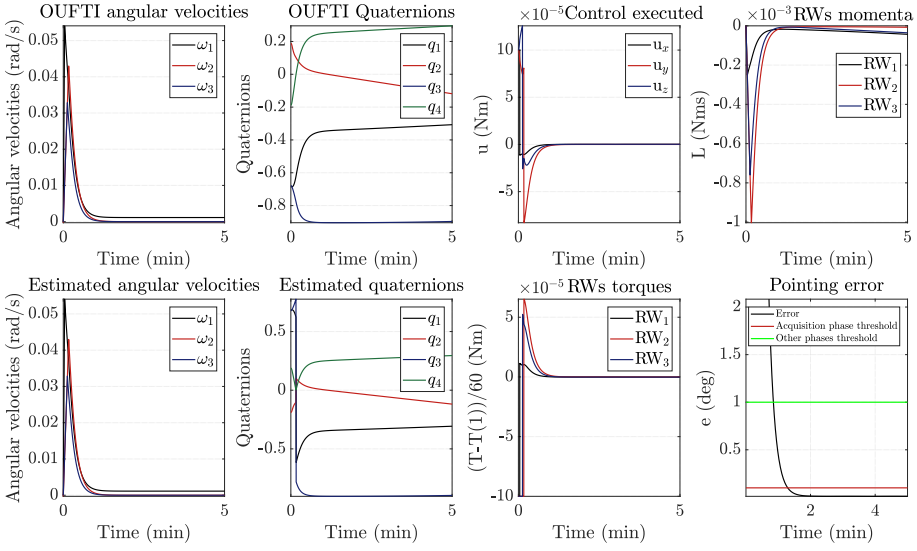

Figure 6.15: *Most important results during downloading phase, in mission 1, on ISS orbit. The plots are zoomed in order to catch the most interesting behaviors.*

In the middle of downloading phase, the CubeSat enters in eclipse, as can be seen

from solar radiation plot in Figure 6.16.

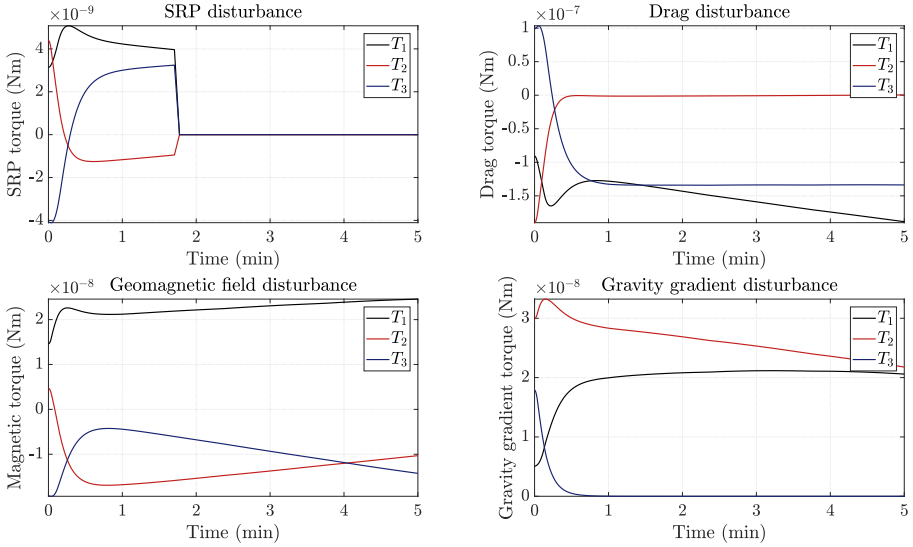

Figure 6.16: *Main disturbances torques during downloading phase, in mission 1, on ISS orbit. T_i are the torques components in body-fixed reference frame.*

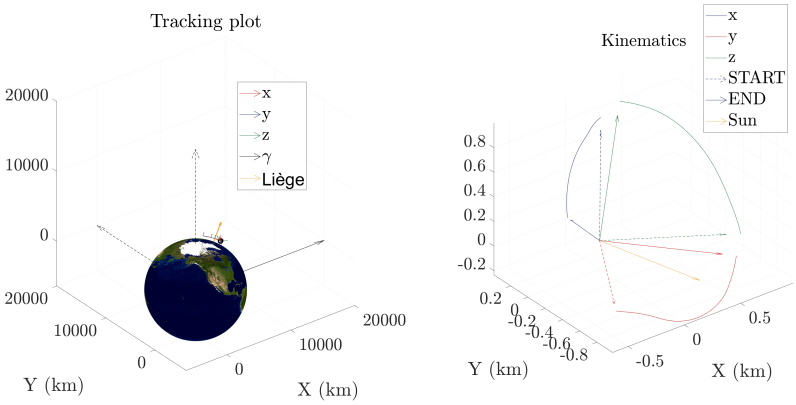

Figure 6.17: *Body-fixed frame while orbiting around the earth during downloading phase, in mission 1, on ISS orbit.*

6.2 Mission 3

Computational time usually requested: around 1 hour, depending on the initial conditions. De-tumbling phase is not reported since it is almost equal to the one presented in Mission 1 results.

Sun-pointing The Sun-pointing phase was set to last till the momentum stored by the wheels will reach the maximum value available. The simulation lasts around 62 hours and 40 minutes, the maximum time before saturation, with solver absolute and relative tolerances set to 10^{-6} both. The steady state is reached after around 100 seconds.

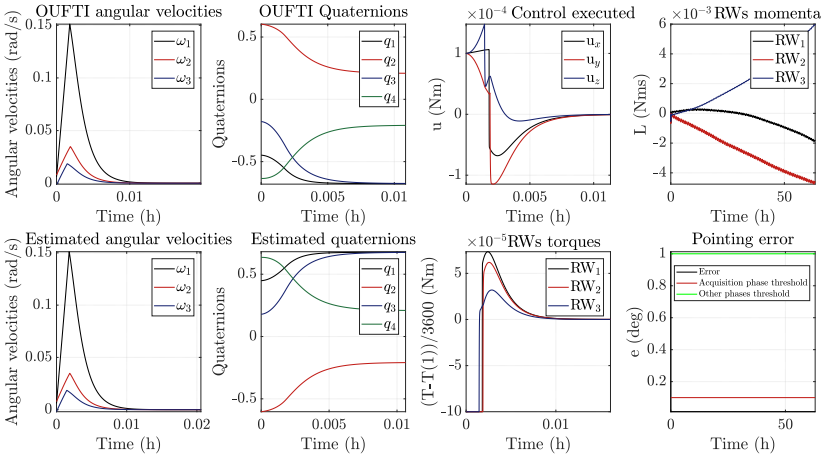

Figure 6.18: *Most important results during Sun-pointing phase in mission 3, on ISS orbit. The plots are zoomed in order to catch the most interesting behaviors.*

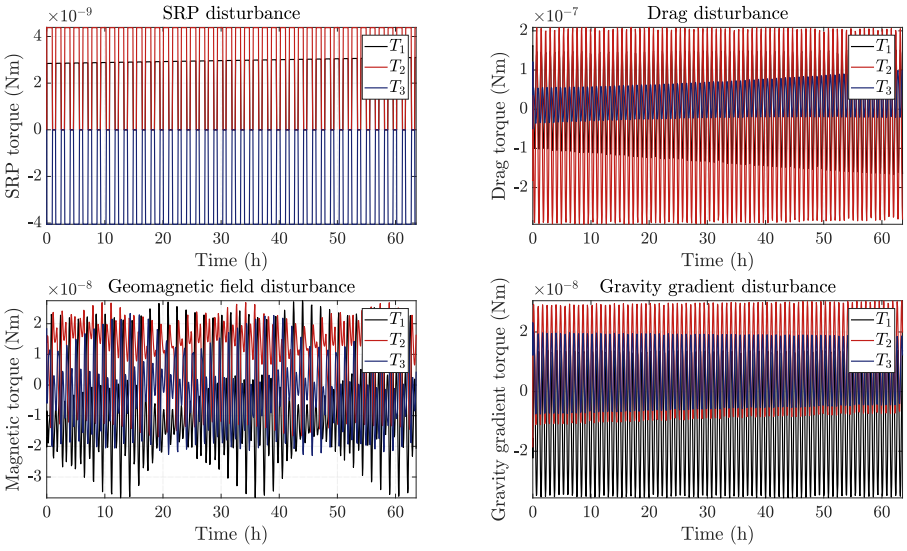

Figure 6.19: *Main disturbances torques during Sun-pointing phase in mission 3, on ISS orbit. T_i are the torques components in body-fixed reference frame.*

De-saturation De-saturation phase lasts 1 day, just to show the behavior of the spacecraft during a longer de-saturation phase.

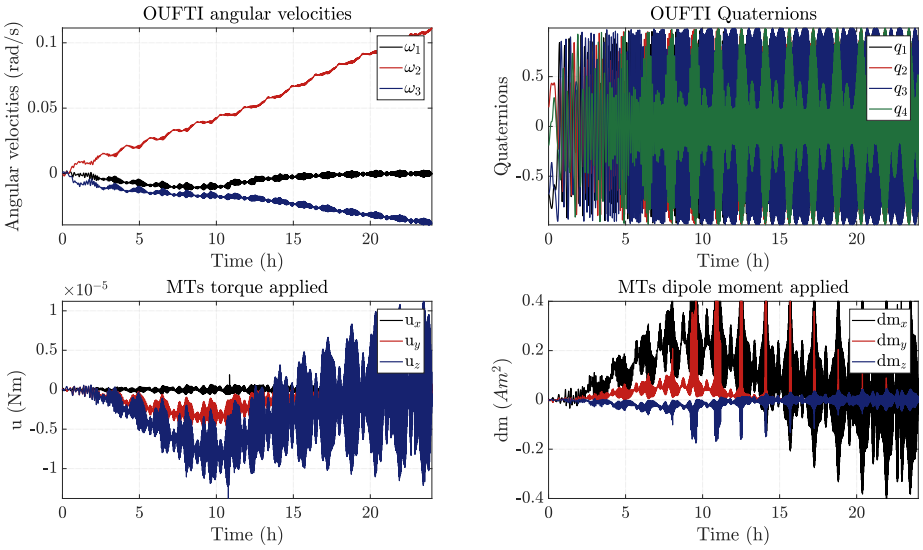

Figure 6.20: *Most important results during de-saturation phase in mission 3, on ISS orbit.*

From Figure 6.20 it can be shown that the angular velocities of the platform increase very slowly, meaning that it is still possible to store solar energy during a de-saturation phase lasting less than a day.

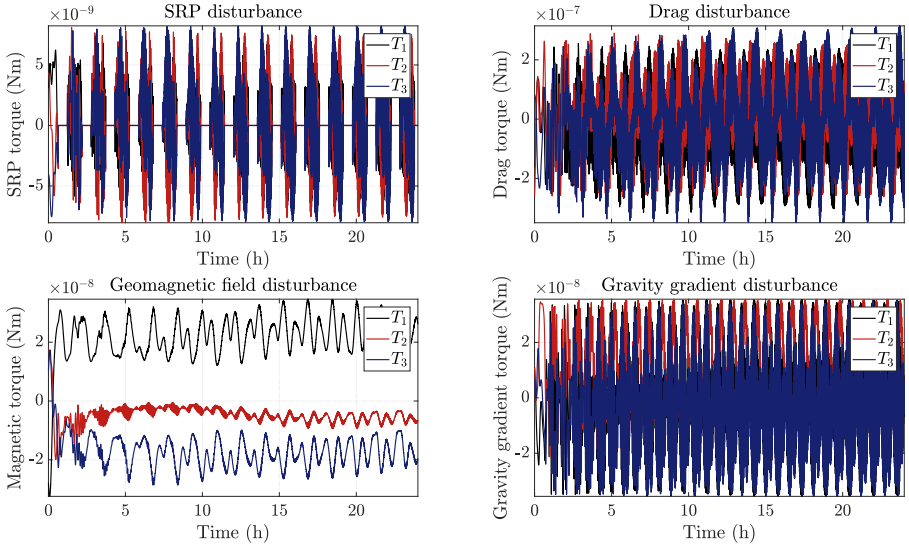

Figure 6.21: *Main disturbances torques during de-saturation phase, in mission 3, on ISS orbit. T_i are the torques components in body-fixed reference frame.*

6.3 Mission 1 with target following pointing

For what concerns mission 1 performed with target following pointing, it was thought to be tedious to present the results of all the phases, since they are similar to the ones already presented in mission 1 for Nadir pointing. As a result only the picture acquisition phase will be presented.
The computational time requested to simulate the whole mission is usually around 10 minutes, depending on the initial conditions. From Figure 6.22 it is possible to appreciate the angular velocity around Z-axis increasing and decreasing while the OUFTI-Next platform is passing over the target, rotating in order to follow the National Park of Brasilia. A similar behavior is shown in the control torque and reaction wheels torque plots. The solver absolute and relative tolerances were set to 10^{-6}.

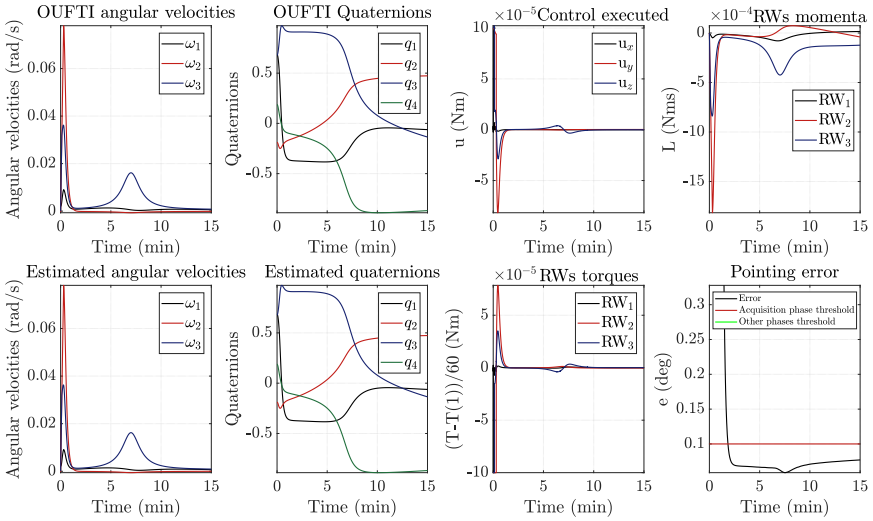

Figure 6.22: *Most important results during target following picture acquisition phase, in mission 1, on ISS orbit. The plots are zoomed in order to catch the most interesting behaviors.*

Another peculiar trend is the one evidenced in Figure 6.22, where the pointing error drops smoothly in almost 1 minute, exactly when the OUFTI-Next platform is passing above the Brazilian National Park. This behavior can be explained looking at Figure 6.23, representing the disturbances level during the acquisition phase: when the CubeSat is approaching the nadir position with respect to the target, the disturbances torques are increasing in magnitude, reaching their maximum when the CubeSat is right above the Brazilian National Park and then start decreasing, following exactly the behavior of the pointing error plot.

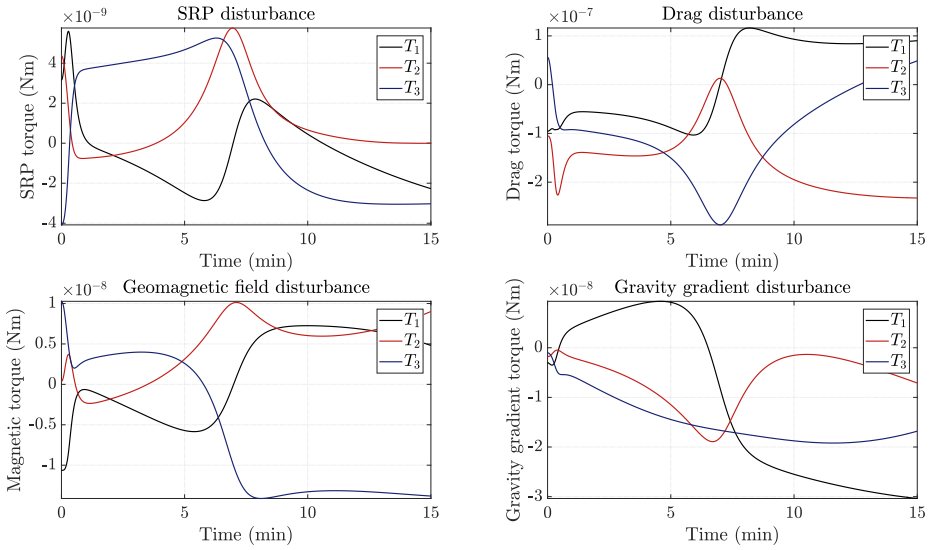

Figure 6.23: *Main disturbances torques during target following picture acquisition phase, in mission 1, on ISS orbit. T_i are the torques components in body-fixed reference frame.*

From Figure 6.24 instead, it is possible to see the red vector (the X-axis of the *body-fixed reference frame*) following the National Park of Brasilia.

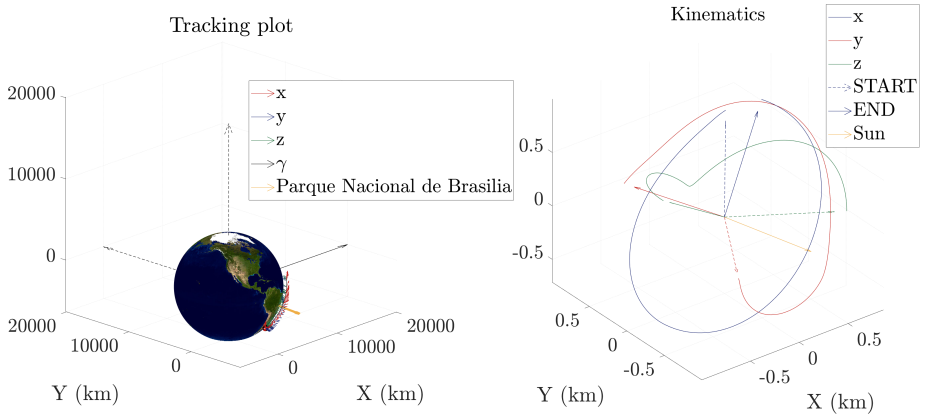

Figure 6.24: *Body-fixed frame while orbiting around the earth during target following picture acquisition phase, in mission 1, on ISS orbit.*

6.4 Noises and update rates

In order to check the effect of noises and sensors update rates on the model, they were added to a nominal Sun-pointing phase lasting 150 s on ISS orbit, the most

challenging one in terms of disturbances level. The simulation is very slow (almost 17 min), so, in order to speed it up, the absolute and relative tolerances of the solvers were relaxed till 10^{-4} and the output reduced to only the estimated and integrated state. The results are here presented in Figure 6.25 and demonstrate that the presence of noises and measurements update rates are not affecting the determination provided by the unscented Kalman filter.
An interesting effect of adding the unscented Kalman filter algorithm and the measurements noises to the model is the numerical instability of *ODE15s*. For this reason this simulation was performed with a different solver: *ODE113*. Usually, on the ADCS units, the main determination algorithm is a Kalman filter, exactly as for the KULeuven one, [56], but since in this Thesis the majority of the simulations were performed with an algebric algorithm based on the star tracker measurements, it could be useful to check, also in this case, the effects of measurements uncertainties. The simulation is equal to the previous one, but performed with the algebric algorithm previously presented and, as a consequence, the computational time is reduced: less than 3 min. The results demonstrate that the algebric algorithm is able to estimate the state maintaining the pointing requirements, as shown in Figure 6.26. Also in the case of the simulation with the algebric algorithm, the addition of noise makes the *ODE15s* numerically instable and, for this reason, the solver used was *ODE113*, as in the previous case.

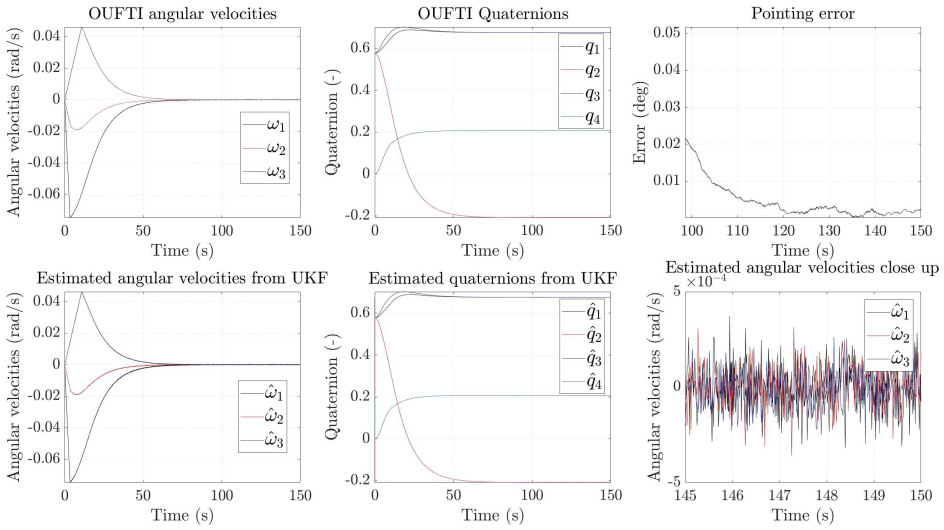

Figure 6.25: *Unscented Kalman filter estimated state compared with the actual one.*

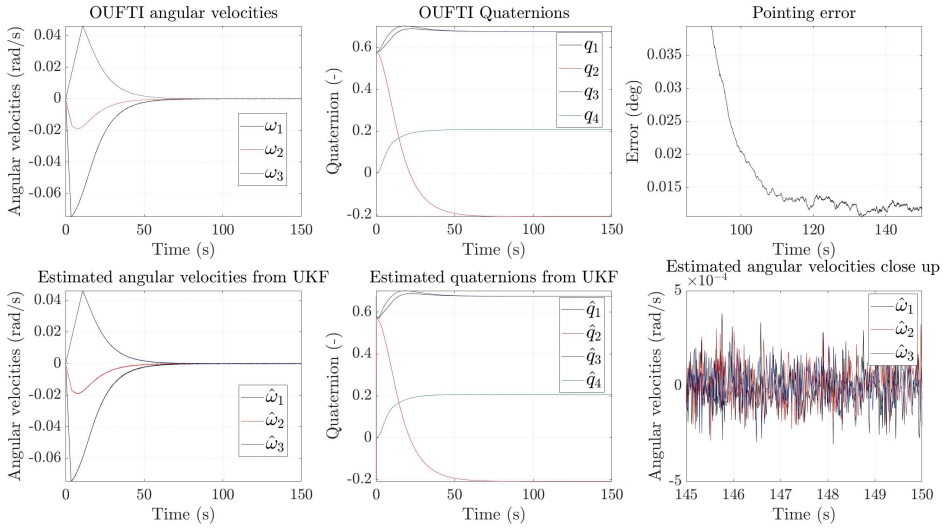

Figure 6.26: *Algebric algorithm estimated state compared with the actual one.*

CHAPTER 7

MISSION PECULIARITIES AND EMERGENCY MODES

7.1 Cryocooler internal disturbance

The OUFTI-Next platform will have a cryocooler on-board, used to cool down the detector before picture acquisition phase. The device will be turned on during the last minutes of Sun-pointing or just at the beginning of picture acquisition phase. In this Thesis it was supposed to be switched on when the picture acquisition starts, because it is the most important phase of the mission and it is fundamental to analyse the stabilization of the platform in this case. The details about the actual performances of this element are still not well defined, but the *SRI401* by *LE-TEHNIKA* was selected as suitable device, Figure 7.1. Thanks to recent structural tests on the cryocooler, the supplier provided the dynamic forces Root Mean Square (RMS) values of the first harmonics, Figure 7.2. According to *LE-TEHNIKA*, the cryocooler usually runs with rotation frequency between $1000 - 1500$ rpm (typical application, ambient/room temperature), highlighted in Figure 7.2.

Figure 7.1: SRI401, *courtesy of* LE-TEHNIKA.

Basic harmonic [1/min]	Fx [N]	Fy [N]	Fz [N]
900	0.012	0.007	0.003
1200	0.014	0.008	0.004
1500	0.022	0.015	0.006
1800	0.025	0.014	0.005
2100	0.026	0.013	0.007
2400	0.033	0.015	0.015
2700	0.041	0.024	0.021
3000	0.049	0.032	0.026
3300	0.059	0.044	0.032
3600	0.074	0.054	0.040

Figure 7.2: *Dynamic forces RMS values of the first harmonics. The X, Y and Z axis are different from the ones used in this Thesis.*

In order to model the internal disturbances due to this device, it was supposed to place it 0.075 m beneath the geometric center of the CubeSat, in the top quarter of the space dedicated to the payload (1.5 U), and shifted in Z and Y direction of 0.0707 m, as shown in Figure 7.3.

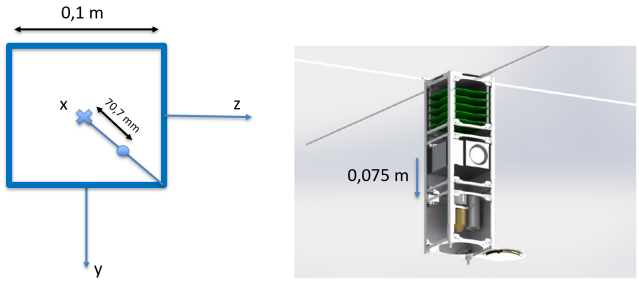

Figure 7.3: *Position of the cryocooler inside of the* ***OUFTI-Next platform!****.*

Once the position was identified, the disturbance torque in Nm acting on the spacecraft, $\boldsymbol{d_{int}}$, can be evaluated with respect to the *body-fixed reference frame* and added to the disturbances model presented in Chapter 2:

$$\boldsymbol{d_{int}} = \begin{bmatrix} -0.0354cos(\frac{\pi}{4})sin(2\pi 25t)F_x + 0.0354cos(\frac{\pi}{4})sin(2\pi 25t)F_y \\ 0.0354cos(\frac{\pi}{4})sin(2\pi 25t)F_z + 0.075sin(2\pi 25t)F_y \\ -0.075sin(2\pi 25t)F_x - 0.0354cos(\frac{\pi}{4})sin(2\pi 25t)F_z \end{bmatrix} \tag{7.1}$$

The introduction of such an high frequency disturbance, with respect to the external ones, affects the computational time, reducing it dramatically. It was decided to simulate just the two most important and interesting phases: the target following picture acquisition, both in ISS orbit and SSO.

7.1.1 Results

On ISS orbit the pointing accuracy is obtained without changing the control parameters used for the simulation in which no cryocooler disturbance was considered. In Figure 7.4 it is possible to notice that, when the OUFTI-Next platform passes above the target, the pointing error will decrease almost smoothly of around 0.01 deg in 1 minute. This behavior is similar to the one observed without the cryocooler disturbance and can be explained looking at Figure 7.7, representing the disturbances level during the acquisition phase: when the CubeSat is approaching the nadir position with respect to the target, the disturbances torques are increasing, reaching their maximum when the OUFTI-Next platform is right above the Brazilian National Park and then start decreasing, exactly as the behavior of the pointing error plot.
In Figure 7.5 the pointing error oscillations introduced by the cryocooler are shown, proving that they are not affecting the pointing accuracy at all. The momentum stored is not saturating the reaction wheels, as it is shown in Figure 7.6. The simulation lasts 550 s and the computational time required is 6.3

hours, with a solver absolute and relative tolerance of 10^{-6}.

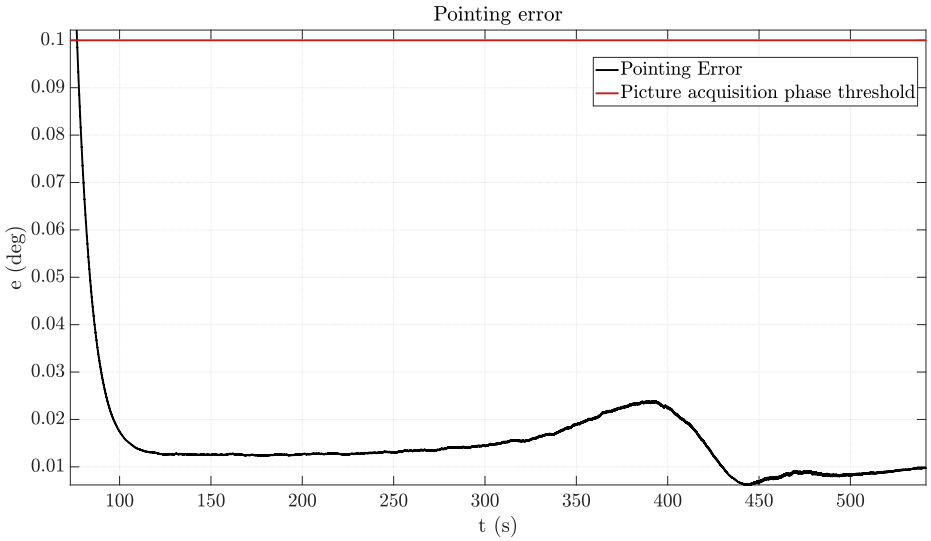

Figure 7.4: *Zoomed pointing error plot, considering also the cryocooler internal disturbance, during target following picture acquisition phase on ISS orbit.*

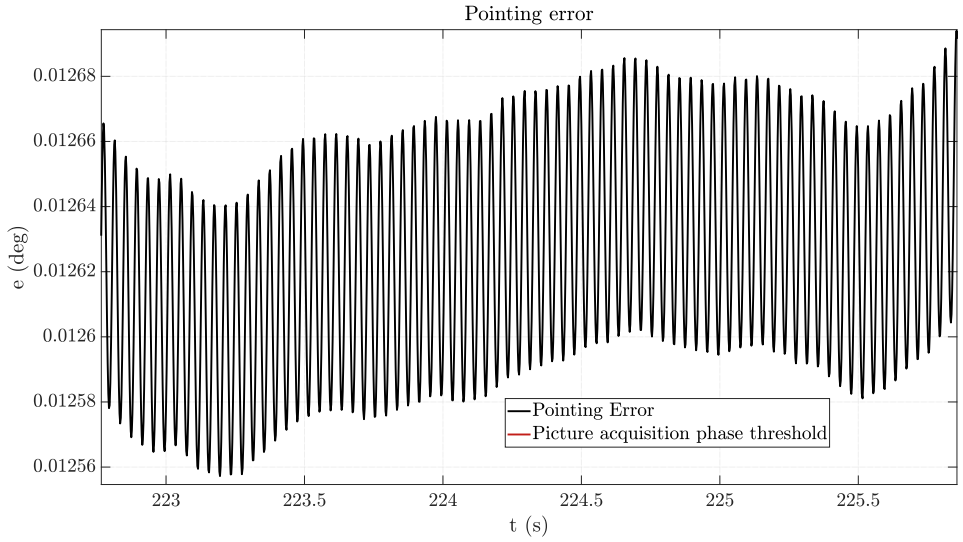

Figure 7.5: *Pointing error oscillations (zoomed plot), considering also the cryocooler internal disturbance, during target following picture acquisition phase on ISS orbit.*

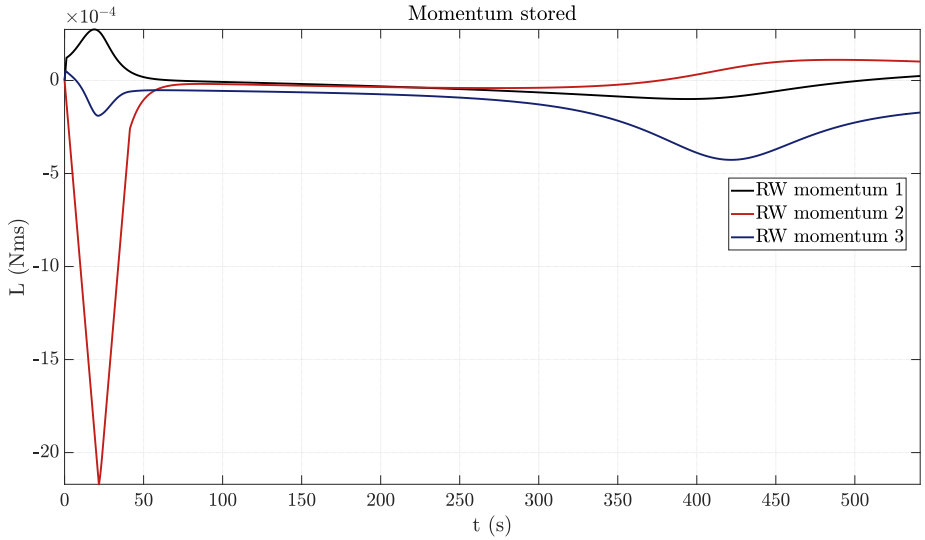

Figure 7.6: *Momentum stored by the reaction wheels during target following picture acquisition phase on ISS.*

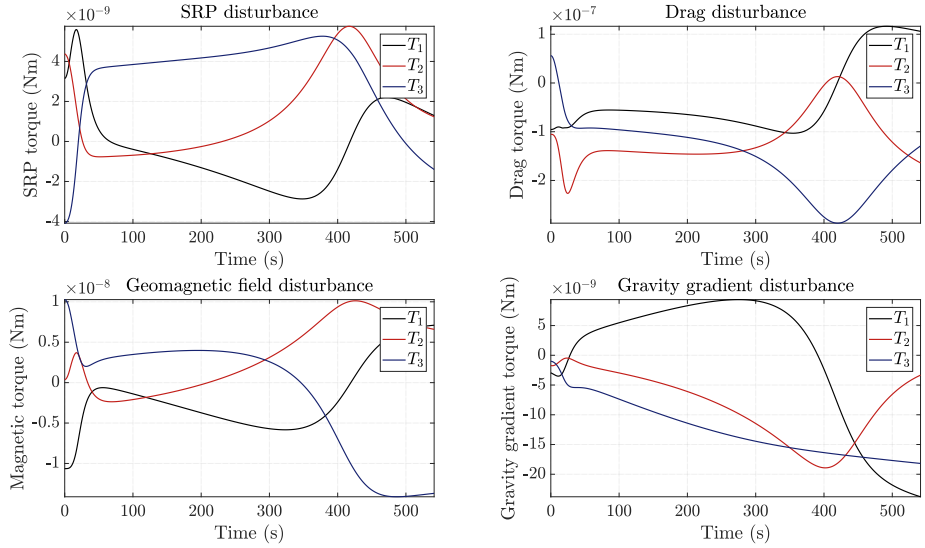

Figure 7.7: *Disturbances torques in ISS orbit during pointing acquisition with cryocooler on.*

On SSO the pointing accuracy is obtained without changing the control parameters, as for ISS orbit and the pointing error trend is almost identical, Figure 7.8. The momentum stored is not saturating the reaction wheels, as it is shown in Figure 7.9. The simulation lasts 550 seconds and the computational time required is 7.45 hours, with a solver absolute and relative tolerance of 10^{-6}.

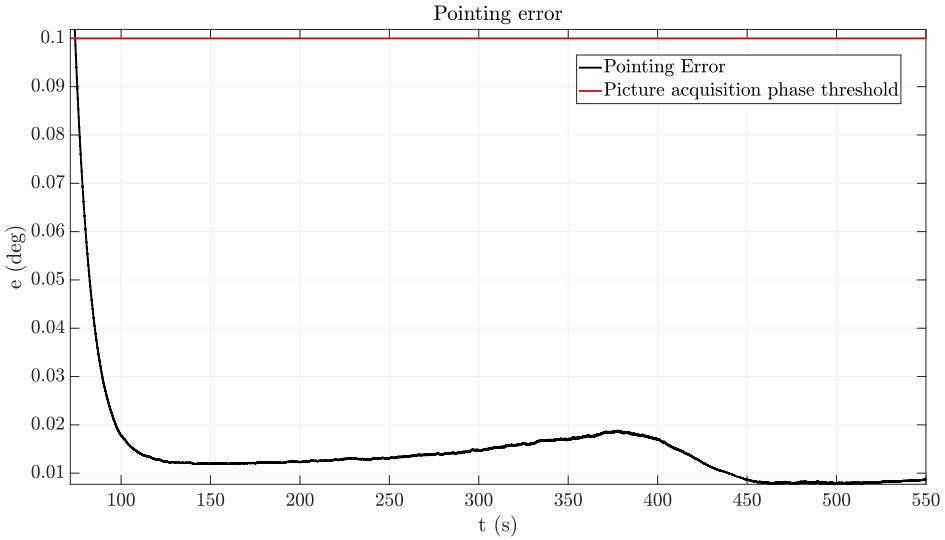

Figure 7.8: *Zoomed pointing error plot, considering also the cryocooler internal disturbance, during target following picture acquisition phase on SSO.*

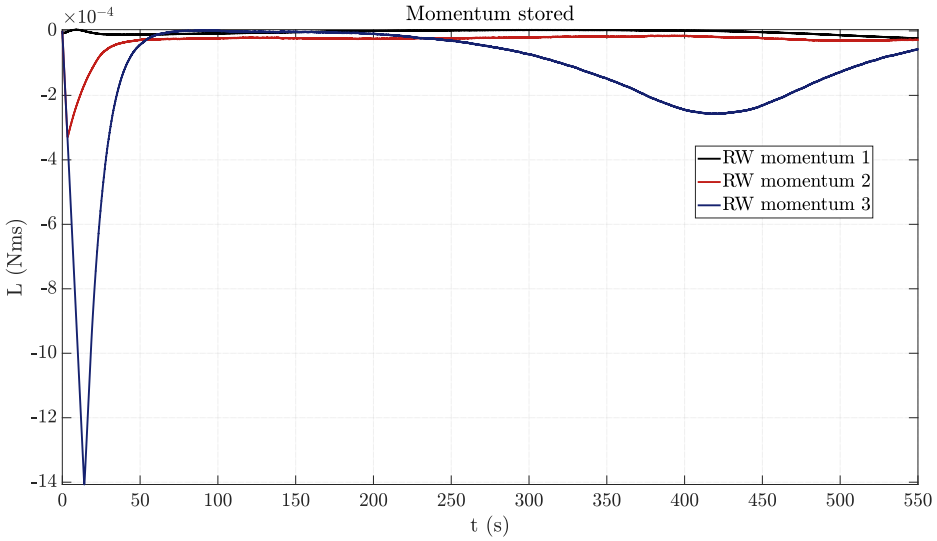

Figure 7.9: *Momentum stored by the reaction wheels during target following picture acquisition phase on SSO.*

7.1.2 Conclusions

The performed simulations about the internal disturbance due to the cryocooler evidenced that the presence of this source of vibrations inside the platform will not affect the pointing accuracy, thanks to the control strategy adopted in this Thesis. Nevertheless, it is important to remark that the position of the cryocooler was just reasonably guessed and, as a result, it is advisable to perform again this

kind of simulations, once the details about the cryocooler will be acquired. Moreover, from the analysis results, it is also possible to state that the stability requirement of 0.01° can be achieved in time intervals lasting less than 1 minute.

7.2 Trade-off between *iADCS100* and *KULeuven units*

So far, all the simulations were carried out using the data of *iADCS100* by *Hyperion*. Nevertheless, it is interesting to compare (also through dedicated simulations) the performances with the ones of the *KULeuven* ADCS unit[56], in order to understand which one is the most suitable for the OUFTI-Next project. In this Chapter, different characteristics of the two units will be reported, but no deeper comparisons between the determination algorithms, since *Hyperion* does not declares which one is used in *iADCS100* on his flyer, [50]. According to KULeuven instead, their unit exploits an *extended Kalman filter*, which is quite similar to the *unscented Kalman filter* implemented in this Thesis.

7.2.1 Equipments

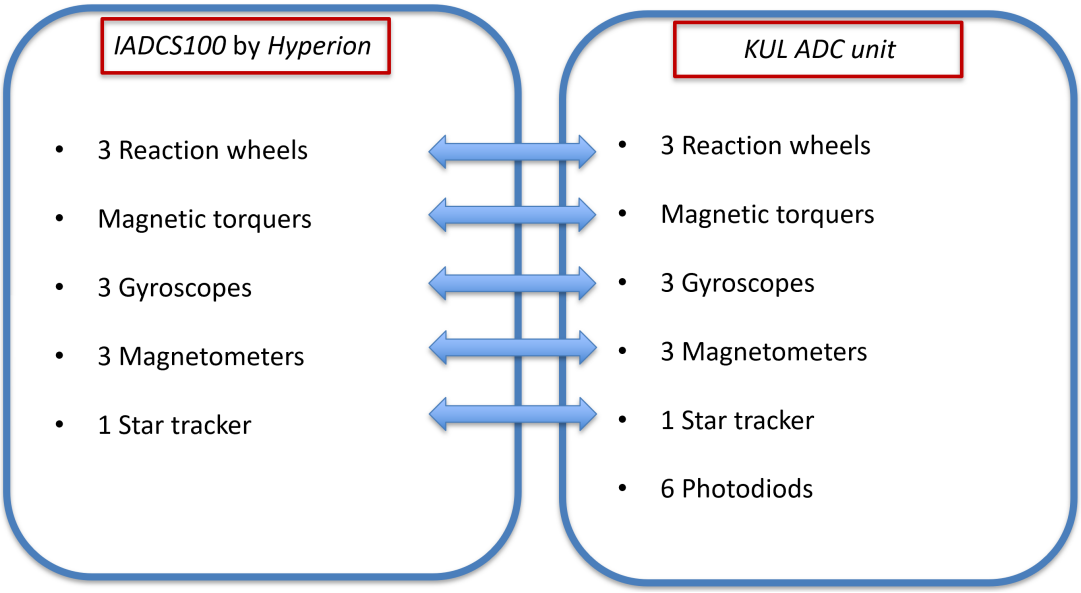

Figure 7.10: *Comparison between the main equipments of both* iADCS100 *and* KULeuven unit.

As it is shown in Figure 7.10, the *KULeuven unit* provides also 6 photodiods, while the *iADCS100* does not explicitly mention them. This sensors are fundamental to retrieve the direction of the Sun (provided by the ephemeris in the simulator coded in this Thesis). According to [50], the *iADCS100* has the interface to be

couple with up to 6 Sun-sensors. This means that these devices would be bought independently from the ADCS unit, increasing the cost of the entire subsystem. Nevertheless, the solar panels usually used for CubeSats have already integrated Sun-sensors, which could be exploited, even if their performances are worst with respect to the ones of dedicated devices. In conclusion, from the equipment point of view, the two units are almost identical.

7.2.2 Performances

From the performances point of view, here are reported the main differences between the two units:

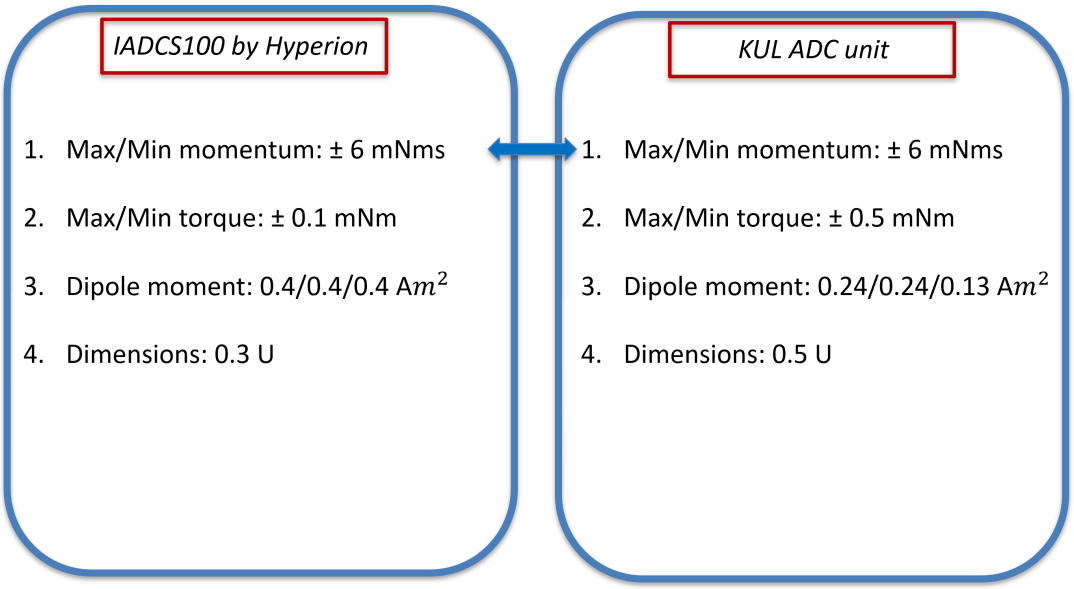

Figure 7.11: *Comparison between the performances of both* iADCS100 *and* KULeuven unit *components.*

As it is remarked in Figure 7.11, both of the units provide the same amount of maximum/minimum momentum storable by the wheels, which is one of the most important parameter for the ADCS, since it drives the saturation time. The highest torque that reaction wheels can produce is provided by the *KULeuven* unit and this is important, because this parameter drives the control torque saturation, really important during transient phases, driving the stabilization time of the platform. Changing the maximum torque from 0.1 mNm to 0.5 mNm, the time to get a steady state response decreases from 100 s to 50 s.
The magnetic torquers of *iADCS100* produce an higher dipole moment per axis, but this is not a fundamental performance, since it drives only slightly the detumbling time, decreasing/increasing it of almost 15 min.
The most critical aspect for the OUFTI-Next project is the dimension of the ADCS,

since half of the space available is occupied by the payload and the volume dedicated to the ADCS is reduced. As a result, the volume of *iADCS100*, 0.3 U, is much more suitable with respect to the one of the *KULeuven* unit, 0.5 U, and this could be one of the most important drivers for choosing the unit by *Hyperion*.

7.2.3 Accuracy

After a meeting with the person in charge of the *KULeuven ADCS unit*, the data about their sensors accuracy were obtained and a set of simulations, similar to the ones reported in Chapter 6 on ISS orbit in Sun-pointing, were performed to check for the pointing budget in presence of noises and measurements uncertainties. Here the data used are reported:

- gyroscopes angular rate noise: 1.4×10^{-4} $\frac{\text{rad}}{\sqrt{\text{s}}}$.
- gyroscopes random rate noise: 5.24×10^{-6} $\frac{\text{deg}}{\sqrt{\text{s}^3}}$.
- Star tracker cross boresight error: 40 arcsec (real sky tests show that it is much smaller, down to around 2 arcsec, but KULeuven declares 40 arcsec as more conservative value).
- Star tracker boresight error: 300 arcsec (real values show almost 10 arcsec).
- Magnetometers error: 3°.
- Photodiods error: 5°.

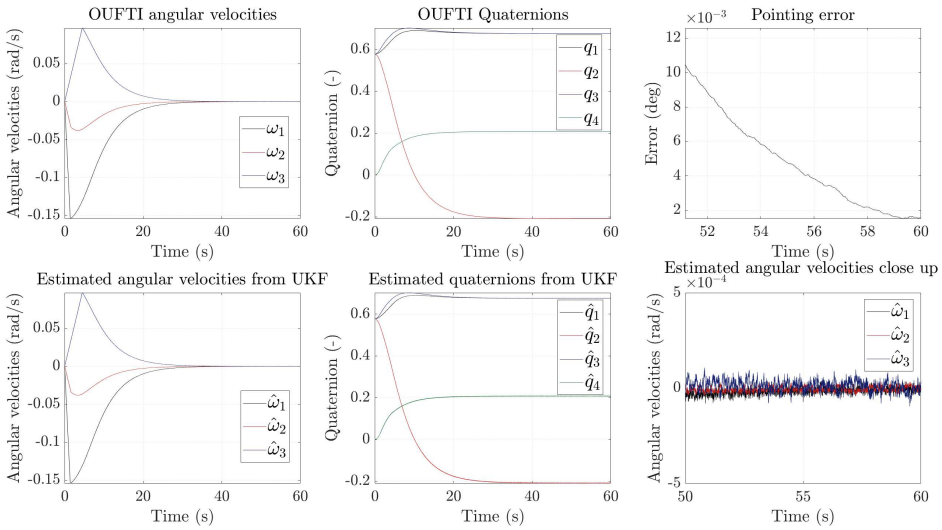

Figure 7.12: *Simulation results concerning the pointing budget and estimation quality of KULeuven unit.*

From Figure 7.12, it s possible to appreciate that the pointing accuracy require-

ments are satisfied. Nevertheless, KULeuven declares in his flyer [56], that the best accuracy possible during fine pointing is 0.11°. This is due to the fact that their simulator is based on a much more accurate typical noises generator, PEET by ESA [7], which decreases the resulting pointing accuracy of the device. To build such a complex model is beyond the aim of this Thesis and, once the supplier for the ADCS will be chosen, it will provide deeper simulations considering its unit and the OUFTI-Next platoform integrated.

7.2.4 Conclusions

The two ADCS units here presented are very similar from the equipment/performances point of view and according to their flyers, they can reach pointing budgets in accordance with the project requirements ones. For this reason the driving parameter is not related to the ADCS, but to the configuration subsystem, since the unit should be the one with the smallest volume. As a result, *iADCS100* by *Hyperion* is the best choice at the moment.

7.3 Emergency modes

In this section some ADCS failures mitigation strategies are investigated. For what concerns the operational requirements, the mission is considered failed when the OUFTI-Next platform experiences more than one failure on-board. As a result, it could be interesting to understand how to maintain the control of the spacecraft, when the star tracker or one reaction wheel stops working.

7.3.1 One reaction wheel failure

If one of the wheels fails, it is usually possible to switch the control logic to a mixed strategy: one magnetic torquer and two reaction wheels. In order to do that, the quaternion control law remains the same, but only two components of the requested control torque will be provided by the wheels, while the remaining one will be provided by one magnetic torquer. Also the integration of the two reaction wheels momenta is the same as before; what changes is the magnetic torquers control strategy. The steps for the design are the following, based on the case in which the broken reaction wheel is the one with its gyroscopic axis oriented as the Y-axis:

1. Evaluate the desired control torque, $\boldsymbol{u}$, exactly as in nominal mode.
2. Integrate just the first and third components of reaction wheels momentum and then check for saturation both the values obtained and the first and third

components of the reaction wheels torque. At the end of this point, two of the three components of the real control torque are known: $u_{r,x}$ and $u_{r,z}$.

3. The second component is obtained from magnetic torquers active control law, Eq. (7.2), selecting only the y-component of the control $\boldsymbol{u}$ vector:

$$\boldsymbol{u} = \begin{bmatrix} 0 & -B_z & B_y \\ B_z & 0 & -B_x \\ -B_y & B_x & 0 \end{bmatrix} \boldsymbol{m} \tag{7.2}$$

where B_i are the components of the magnetic field vector in *body-fixed reference frame*, B_b, and $\boldsymbol{m}$ is the requested dipole moment. Unfortunately, since matrix $\boldsymbol{B_b}$ is skew-symmetric, it is not invertible and, as a consequence, no informations about the requested dipole moment can be retrieved from this expression. In the case in which two reaction wheels stop working, it is possible to obtain an invertible expression, but this is not the case. As a result, the only way to solve the problem is to use a coarser pointing law, coming from:

$$\boldsymbol{u_r} = \boldsymbol{m} \times \boldsymbol{B_b} \tag{7.3}$$

$$\boldsymbol{B_b} \times \boldsymbol{u_r} = \boldsymbol{B_b} \times \boldsymbol{m} \times \boldsymbol{B_b} \tag{7.4}$$

recalling the following vectorial identity [32], expressed in Eq. (7.5), and assuming that the moment is perpendicular to the magnetic field.

$$\boldsymbol{a} \times (\boldsymbol{b} \times \boldsymbol{c}) = \boldsymbol{b}(\boldsymbol{a} \cdot \boldsymbol{c}) - \boldsymbol{c}(\boldsymbol{a} \cdot \boldsymbol{b}) \tag{7.5}$$

$$\boldsymbol{B_b} \times \boldsymbol{u_r} = (\boldsymbol{B_b} \cdot \boldsymbol{B_b})\boldsymbol{m} \tag{7.6}$$

$$\boldsymbol{m} = \frac{\boldsymbol{B_b} \times \boldsymbol{u_r}}{(\boldsymbol{B_b} \cdot \boldsymbol{B_b})} \tag{7.7}$$

This control strategy was checked on target following picture acquisition phase on ISS orbit, providing the following results:

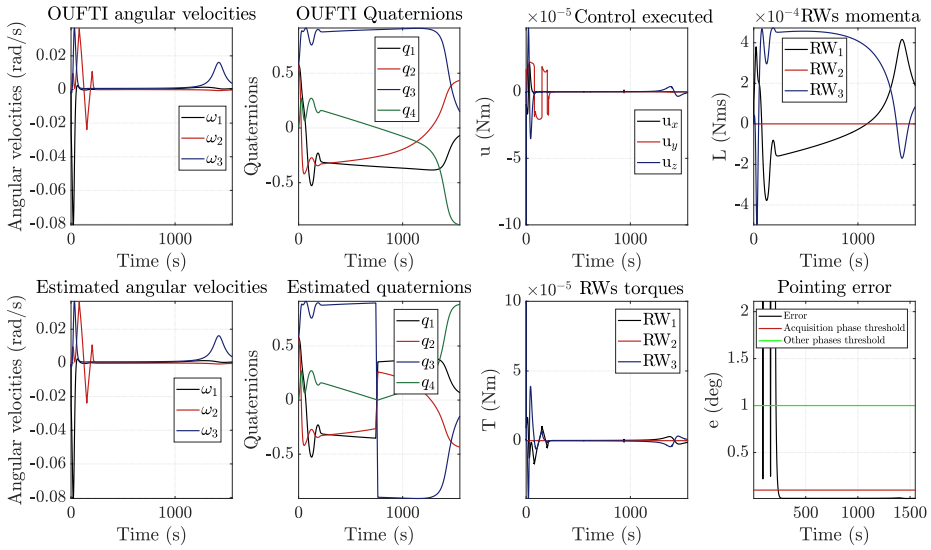

Figure 7.13: *Emergency control strategy results with one magnetic torquer and two reaction wheels.*

As it can be shown in Figure 7.13, the control law satisfies the pointing accuracy requirement. An important remark is about which reaction wheel breaks: if the one whose gyroscopic axis is oriented along the pointing axis stops working, the pointing stabilization is reached in the same time of the nominal scenario, while the spacecraft will rotate for some seconds more along the pointing axis. In the two remaining cases, the spacecraft will need more time to stabilize, exactly as for the case analysed in this chapter, in which the stabilization time doubles.

7.3.2 Star tracker failure

If the star tracker fails, one of the less computational demanding determination techniques which can be used is the *Triad method* [57]. In order to use it, two vectorial measurements are needed and, in the case of the OUFTI-Next mission, they are provided by the magnetometers and photodiods. The CubeSat has onboard the Sun ephemeris, $\boldsymbol{S_n}$, and the Earth magnetic field vector from an onboard model, $\boldsymbol{B_n}$, both of them in *inertial reference frame*; from the sensors it can obtain the Sun direction and the magnetic field vector in *body-fixed reference frame*, $\boldsymbol{S_b}$ and $\boldsymbol{B_b}$. Once all of them are known, it is possible to achieve the attitude matrix following these steps:

$$\boldsymbol{V_b} = \left[\boldsymbol{B_b} \quad \frac{\boldsymbol{B_b}\times\boldsymbol{S_b}}{|\boldsymbol{B_b}\times\boldsymbol{S_b}|} \quad \boldsymbol{B_b}\times\frac{\boldsymbol{B_b}\times\boldsymbol{S_b}}{|\boldsymbol{B_b}\times\boldsymbol{S_b}|}\right] \tag{7.8}$$

$$\boldsymbol{V_n} = \left[\boldsymbol{B_n} \quad \frac{\boldsymbol{B_n}\times\boldsymbol{S_n}}{|\boldsymbol{B_n}\times\boldsymbol{S_n}|} \quad \boldsymbol{B_n}\times\frac{\boldsymbol{B_n}\times\boldsymbol{S_n}}{|\boldsymbol{B_n}\times\boldsymbol{S_n}|}\right] \tag{7.9}$$

$$\boldsymbol{V_b} = \boldsymbol{A_{b/n}} \boldsymbol{V_n} \rightarrow \boldsymbol{A_{b/n}} = \boldsymbol{V_b} \boldsymbol{V_n^T} \tag{7.10}$$

with

$$\boldsymbol{B_b} = \boldsymbol{A_{\epsilon,B}} \boldsymbol{A_{b/n}} \boldsymbol{B_n} \tag{7.11}$$

$$\boldsymbol{S_b} = \boldsymbol{A_{\epsilon,S}} \boldsymbol{A_{b/n}} \boldsymbol{S_n} \tag{7.12}$$

$\boldsymbol{A_{\epsilon,B}}$ and $\boldsymbol{A_{\epsilon,S}}$ are respectively the accuracy matrices of the magnetometers and photodiods, based on Eq. (2.43),where the argument of trigonometric functions are the sensors accuracy on each axis in radians. According to KULeuven, the accuracy of the magnetometers and photodiods are respectively 3° and 5°. This determination strategy was checked during Sun-pointing phase on ISS orbit, providing the following results:

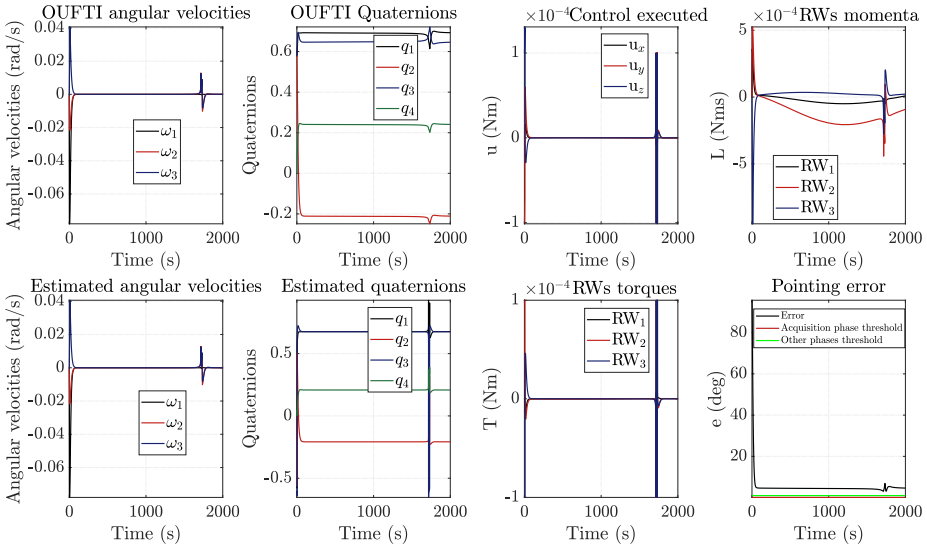

Figure 7.14: *Emergency determination strategy results based on* Triad method.

As expected from the low accuracy of the sensors, the pointing accuracy is not enough to fulfill the requirements during picture acquisition, but the CubeSat can still point to the Sun and store energy on-board. Finally it can be interesting to remark the presence of some peaks in the quaternion estimation plots, affecting slightly the dynamics, Figure 7.14. It can be supposed that the issue is due to the lack in sensors accuracy, since the estimated and the integrated quaternions differ close to the peak and no numerical instabilities or noises are evidenced (the simulation was run also with different solvers, providing the same results).

CHAPTER 8

THE OUFTI-NEXT MISSION CONCLUSIONS

8.1 Results achieved

THANKS to this Thesis it was possible to simulate the control and determination action of the OUFTI-Next platform ADCS, providing three mission profiles which represent the dynamics of the 3 Units CubeSat during its life time, both in ISS orbit and SSO.
In Chapter 4 the main design steps, previously obtained from the team about the other subsystems, are presented, as well as the nominal mission profiles implementation. The same chapter was dedicated to explain the logic behind control parameters optimisation and then in Chapter 6 the majority of the results were listed and commented. Additional analyses were performed in Chapter 7, about the cryocooler disturbances effects, the trade-off between the *Hyperion* and the KULeuven ADCS units and finally the emergency strategies in case of one reaction wheel or the star tracker failure.
No power budget was reported, since the power requested by the ADCS unit is almost constant during all the mission phases and a preliminary analysis on the peak power requested (20% margined) was already performed in [46].

From the results obtained, the most important remarks are here reported:

- The de-tumbling phase will last approximately 1 hour and 40 minutes.
- The saturation of the reaction wheels can be managed with de-saturation phases tested in this Thesis. The maximum time the spacecraft can remain in Sun-pointing before saturating is around 64 hours and 40 minutes on ISS orbit and around 89 hours on SSO.
- The pointing budget of 0.1° is perfectly achieved in all the picture acquisition phases, even the ones with target following slew manoeuvres. Also the pointing stability is guaranteed under the value requested, 0.01°.
- The ADCS unit should be located the closest to the actual center of mass of the platform, which should be as close as possible to the geometric center. Changes in its position will not affect dramatically the results obtained in this Thesis, but more refined simulations should be performed in order to guarantee the pointing accuracy and stability.
- The cryocooler disturbance seems not to increase the pointing error till exceeding the admissible value, 0.1° and the pointing stability is maintained guaranteed as well.
- The introduction of noises and sensors update rates, with the actual level of detail, is not altering the determination error, maintaining the pointing error below the previously stated threshold.
- From the trade-off analysis it is clear that both the *iADCS100* and the *KULeuven unit* are able to satisfy all the OUFTI-Next ADCS requirements with similar performances. The driving parameter that will probably affect the choice between them is the size.
- If one reaction wheel fails, the pointing stability and accuracy can be in any case maintained, doubling the stabilization time.
- If the star tracker fails the determination algorithm implemented, based on *Triad method*, is able to guarantee a pointing error of around 9°, meaning that no picture acquisition is possible, but Sun-pointing can be maintained, as well as power generation on-board.

The aim of the work done at the University of Liége was to demonstrate that the pointing requirements needed by the detector can be achieved using ADCS units of reduced size, such as the ones provided by *Hyperion* and KULeuven. Once the ADCS unit supplier will be chosen, it will provide deeper analysis about the specific unit performances using a professional simulator.

8.2 Future developments

Here are reported future developments that can be accomplished in future design steps of the OUFTI-NextADCS:

- To provide a deeper analysis on the de-tumbling phase, which is the most unpredictable one, with magnetometers measurements and noises as well. Also a Montecarlo analysis or just a sensitivity analysis varying the residual dipole moment would be advisable.
- To optimize the control constant k_{DeT}, used in de-tumbling phase.
- All the phases should be simulated with the exact inertia matrix and with the exact location of all the subsystems and the payload, benchmarking the results with the ones of this Thesis.
- To implement a more complex Kalman filter, capable of estimating also the gyroscopescopes and star tracker bias.
- To perform a deeper analysis with PEET by ESA [7] to refine the analysis performed with noises.

Finally the tool provided with this Thesis can be optimised and improved in order to simulate more realistically the attitude on orbit, once all the other subsystems will be completely sized and located inside the CubeSat.

Part III

The ZodiArt iSEE Mission and the Attitude-Orbit Coupled Simulator

CHAPTER 9

INTRODUCTION TO THE ZODIART ISEE PROJECT

The Global Sustainable Development Goals [58] are 17 objectives addressing the global challenges such as poverty, inequality, climate, environmental degradation, prosperity, peace and justice, as shown in Figure 9.1, and they are the focus of the ZodiArt iSEE project. This mission is characterised by a set of MicroSat flying in formation and constituting an artificial constellation in the sky, easily recognisable from ground. This is possible thanks to high reflective balloons embarked on the top of platforms, similar to the render shown in Figure 9.2. People can interact with the system using a mobile app to prove the fulfilment of the Global Sustainable Development Goals, obtaining from the constellation a picture of the surroundings, when the formation will pass above the user. The orbit was identified after a trade-off analysis presented in [1] and [17], providing good visibility from the most important cities of the world during the twilight.The constellation will generally point the Nadir direction, performing Earth observation.

Figure 9.1: *Global Sustainable Development Goals, [58].*

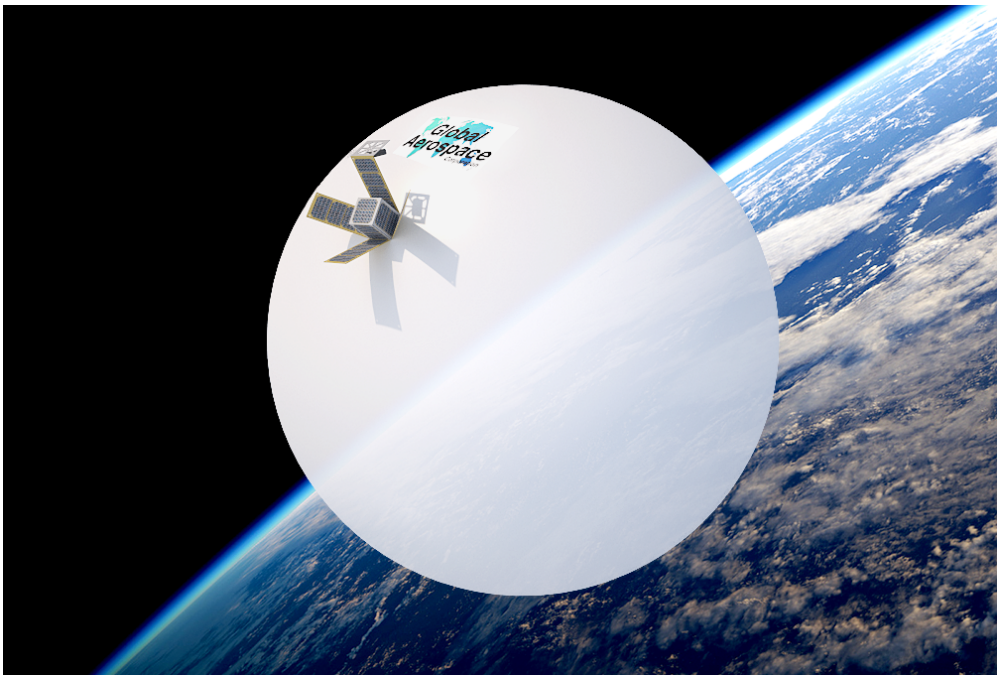

Figure 9.2: *Example of inflatable balloon, [59].*

9.1 The ZodiArt mission requirements and and previous design steps

Before this work, a preliminar mission design was performed in [1] and [17], providing the keplerian parameters of a suitable orbit, optimising the visibility during twilights and downs, guaranteeing repetitivity each day after 14 revolutions and

remaining Sun-Synchronous exploiting the Earth J_2 effect. The selected orbital elements are reported in Table 9.1.

Table 9.1: *Nominal orbit Keplerian parameters.*

$a(km)$	$e(-)$	$i(^\circ)$	$\Omega(^\circ)$	$\omega(^\circ)$	$\theta(^\circ)$
7266,5	0.001	99	285	0	0

Moreover the preliminary design of the structure and the balloon resulted into a $1 \times 1 \times 1$ m bus with a global weight of 122 kg (20% margined) and a 10 m diameter balloon weighting 4.4 kg. According to this baseline, the platform matrix of inertia was assumed to be diagonal, neglecting the contribution of the balloon mass and assuming the center of mass to be in the geometric center of the bus, referring to the reference system shown in Figure 9.3.

$$\boldsymbol{I_z} = \begin{bmatrix} I_1 & 0 & 0 \\ 0 & I_2 & 0 \\ 0 & 0 & I_3 \end{bmatrix} = \begin{bmatrix} \frac{1}{12}m2l^2 & 0 & 0 \\ 0 & \frac{1}{12}m2l^2 & 0 \\ 0 & 0 & \frac{1}{12}m2l^2 \end{bmatrix} = \begin{bmatrix} 20.33 & 0 & 0 \\ 0 & 20.33 & 0 \\ 0 & 0 & 20.33 \end{bmatrix} kgm^2 \tag{9.1}$$

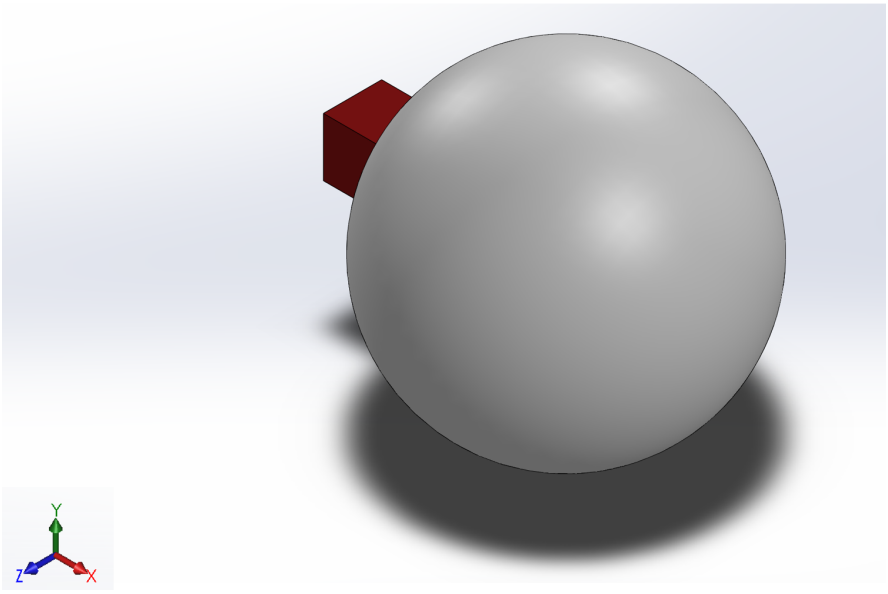

Figure 9.3: *The ZodiArt iSEE mission platform CAD, performed in SolidWorks^{TM}.*

In [17] also a preliminary ADCS design was performed and in the Thesis, exploiting the simulator implemented, the previous results will be enriched by the ones provided by the simulations.

The mission is still at its early design stages and, for this reason, no informations about the Earth observation payload are available at the moment, but in [17] a 1° accuracy was considered as requirement for the mission. In Table 9.2 all the requirements related to the ADCS are reported:

Table 9.2: *ZodiArt iSEE ADCS requirements. M is refered to Mandatory.*

REQ. ID	Importance	Requirement	Note
Z-P-F-ADCS-0010	M	The ADCS shall be able to detumble the spacecraft after detachment from the launcher.	Z = ZodiArt, P = Platform, F = Functional
Z-P-F-ADCS-0020	M	The ADCS shall provide Nadir pointing.	
Z-P-F-ADCS-0030	M	The ADCS shall be able to determine the attitude within ±1 arcsec in each axis.	
Z-P-F-ADCS-0040	M	The ADCS shall provide a de-saturation strategy.	
Z-P-F-ADCS-0050	M	The ADCS shall counteract environmental disturbances.	e.g.: SRP, Atmospheric Drag, etc.
Z-P-F-ADCS-0080	M	The ADCS shall be able to provide a pointing accuracy of $< 1°$ and a control stability of $< 0.1°$ during Nadir Pointing.	
Z-P-O.0010	M	The platform shall be maintained on the initial orbit selected.	O = Operational

The set of actuators used in the simulations are the same of the ones considered for the OUFTI-Next mission, but with different characteristics that will be presented in Chapter 10:

- 3 Reaction wheels.
- 3 Magnetic torquers.

Instead, for what concerns attitude determination, the very same sensors embarked in the OUFTI-Next platforms were considered, since their dimension, weight and accuracy are optimal also for the ZodiArt iSEE mission.

In Part III a complete analysis on the orbit propagation, as well as the determination of a quasi-frozen orbit with respect to J_2 and SRP can be found in Chpater 10. In the same chapter, the nominal mission profile attitude-orbit decoupled simulations are reported. After having performed these preliminary analysis, the fine coupling between attitude and orbital dynamics due to the atmospheric drag/lift and solar radiation pressure is discussed in Chapter 11. Usually, this effect is neglected, since the balloon attitude, being the most relavant surface of the spacecraft, does not affect the orbital shape. However, the platform can exploit the bus position to increase or decrease the surface exposed to the relative and solar wind, inducing a fine coupling.

CHAPTER 10

ORBIT PROPAGATION AND NOMINAL MISSION PROFILE SIMULATION

In Section 10.1 the orbit propagation under the effects of the orbit perturbations is presented, while in Section 10.2 the analysis to found a quasi-frozen orbit with respect to J_2 and SRP is reported. Finally, in Section 10.3 the nominal mission profile orbit-attitude decoupled simulations are described.

10.1 Orbit propagation

Since in [17] the orbit propagation was characterised only by the J_2 effect, the complete analysis involving also the SRP, atmospheric drag and lift, as well as the Earth zonal harmonic and the Moon/Sun third body perturbations was performed.

10.1.1 Solar radiation pressure

The only coupling introduced by SRP is very low and due to the reflectivity of the bus surface. Indeed, the inflatable balloon is the largest surface of the satel-

lite and the most reflective, but, since all attitude positions with respect to the Sun provides the same illumination condition, the coupling effect is almost null. From the attitude point of view instead, the net torque due to the solar radiation pressure is the highest among the disturbances, since the arm, consisting in the geometric distance between the center of pressure and the center of mass, is significally longer with respect to common spacecrafts.
For what concerns the optical properties of the bus surface, they were considered equal to the ones of the OUFTI-Next mission, while the aluminized Mylar balloon is characterised by the following optical coefficients:

- C_r, the reflectivity coefficient, equal to 1 [24].

- ρ_s, the surface scattering coefficient, assumed 0.8, from [17], also coherent with the Mylar reflectance used in Echo and PAGEOS I balloons.

- ρ_a, the surface absorption coefficient, assumed ≈ 0.03, assuming opposite optical characteristics with respect to [51].

- ρ_d, the surface diffusive coefficient, assumed ≈ 0.17, obtained as difference from Eq. (10.1).

$$\rho_d + \rho_s + \rho_a = 1 \rightarrow \rho_d = 1 - \rho_a - \rho_s \tag{10.1}$$

Finally it is worth mentioning that the model used for the solar radiation acting on the bus is the same of the OUFTI-Next mission, based on the flat surfaces formulation, Eq. (2.34). The balloon was instead modeled using the cannonball formulation, Eq. (2.26). In order to obtain the perturbative acceleration, both equations were divided by the spacecraft mass.

The attitude-orbit decoupled effect of solar radiation pressure on the orbit evolution is evaluated and the resulting osculating Keplerian parameters are represented in Figure 10.1 and Figure 10.2.

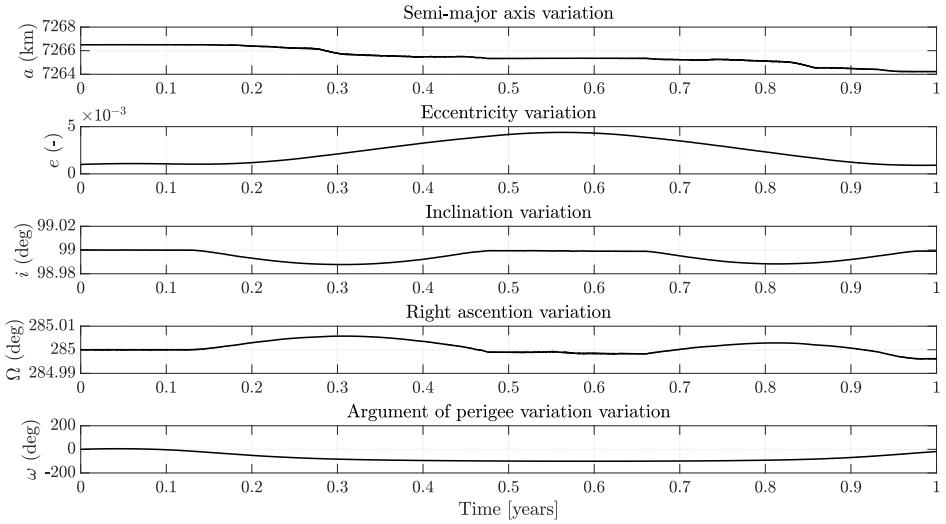

Figure 10.1: *Solar radiation pressure perturbative acceleration effect in 1 year. Initial epoch:* 21^{st} *of March* 2019.

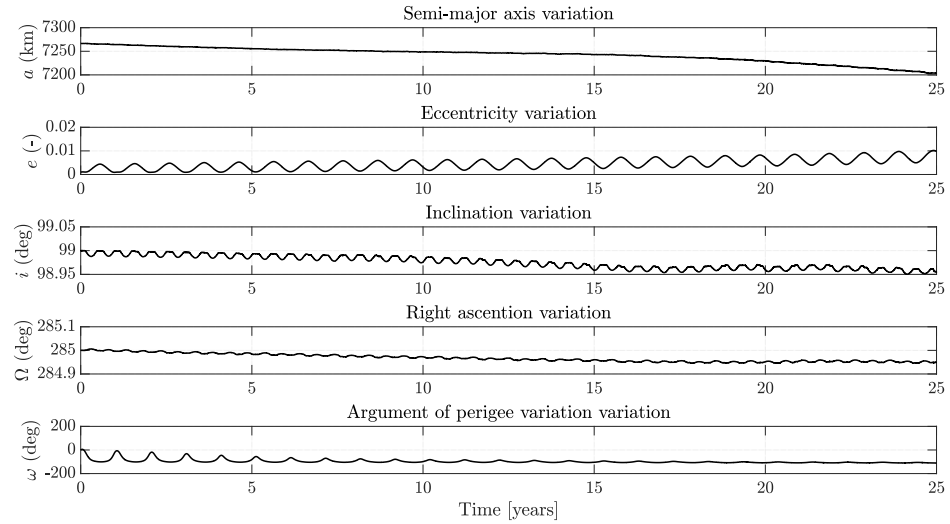

Figure 10.2: *Solar radiation pressure perturbative acceleration effect in 25 years. Initial epoch:* 21^{st} *of March* 2019.

From Figure 10.1 it is possible to appreciate the inclination and RAAN trend, due to the relative position of the orbit with respect to the Sun, during the year. The simulation starts the 21^{st} of March 2019, on spring equinox, when the orbital plane is orthogonal to the Sun direction and the platform does not experience any eclipse. In that position the solar radiation pressure does not affect the inclination and RAAN evolution, while approaching the summer solstice, the effect

is maximum, since the orbital angular momentum vector is orthogonal to the Sun direction and the orbit is half in eclipse and half in sunlight.

10.1.2 Atmospheric drag

As reported in [5], the drag is oriented in the opposite direction of relative wind, which corresponds to the opposite of the velocity direction only in the case analysed in the paper: almost equatorial orbits. In this Thesis the orbit of interest is characterised by an inclination of 99°, meaning that the cross-track perturbation is not negligible a priori. The drag and atmospheric density model are respectively reported in Eqs. (2.27)–(10.1) and 2.2 as drag coefficient, extrapolating the value from [60].
The propagation of Keplerian parameters in one year, under the effects of only drag, decoupled from the attitude dynamics (the spacecraft is assumed to be always Nadir pointing) is reported in Figure 10.3, and after 7 years in Figure 10.4. The plots evidences that the major effect of atmospheric drag is on semi-major axis reduction in time, till complete re-entry after 7 years, satisfying the IADC Space Debris Mitigation Guidelines, [47].

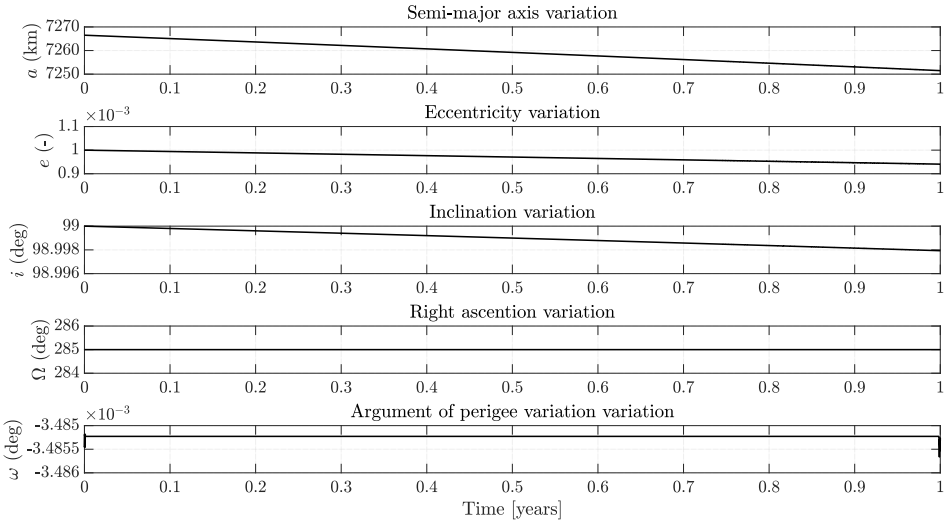

Figure 10.3: *Drag perturbative acceleration effect in 1 year. Initial epoch:* 21^{st} *of March* 2019.

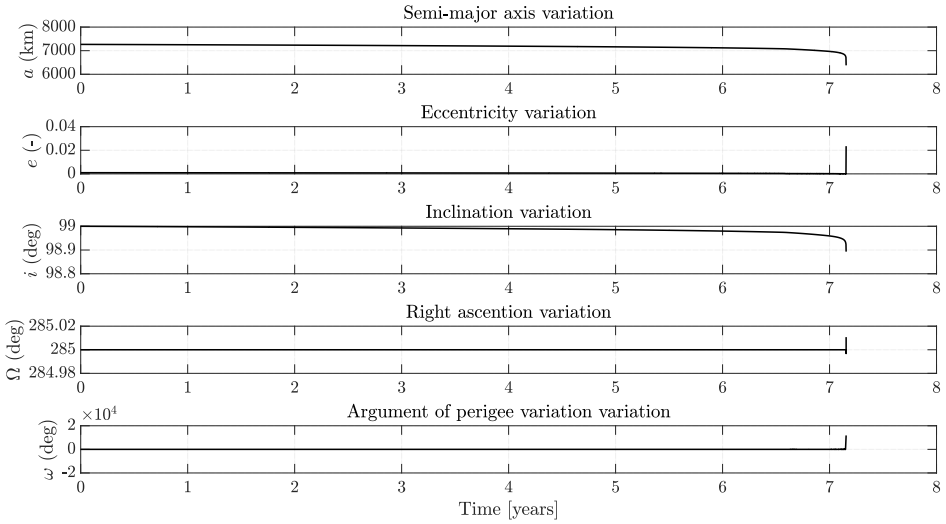

Figure 10.4: *Drag perturbative acceleration effect in 7 years. Initial epoch:* 21^{st} *of March* 2019.

The drag experienced by the ZodiArt platforms is almost constant from the attitude dynamics point of view, since the balloon is spherical, but the position of the bus with respect to the relative wind produces a increment/decrement of drag, resulting in a decrease/increase of semi-major axis, and altitude as well. This phenomenon, also known as *differential drag*, can be exploited to perform a relative fine positioning long-track of different platforms along close orbits. In fact, if the altitude increase, the velocity on orbit decreases and viceversa, inducing a shift with respect to the initial position of the spacecraft.

10.1.3 Atmospheric lift

An exhaustive description of the effects of lift on near circular orbits, for small spacecrafts can be found in [27]. In the case of the ZodiArt mission, a spherical balloon do not generate any lift if it is not spinned. As a result, the only lift effect is the one acting on the bus provided by Eq. (2.31), where C_l was selected exploiting the *specular reflection* assumption above 800 km, [28]:

$$C_l = 2sin(\alpha)sin(\alpha) \tag{10.2}$$

α is the bus angle of attack, measured between the satellite x-axis and the relative velocity vector.The propagation of Keplerian parameters in 1 and 25 years, under the effects of only the lift disturbance, decoupled from the attitude dynamics (the spacecraft is assumed to maintain a 45° angle of attack) is reported in Figure 10.5

and Figure 10.6. It is clear that the effects of lift can be neglected when evaluating the evolution of the orbit in time. This is not true when looking at the fine attitude coupling, where lift can make the spacecraft oscillate along one period.

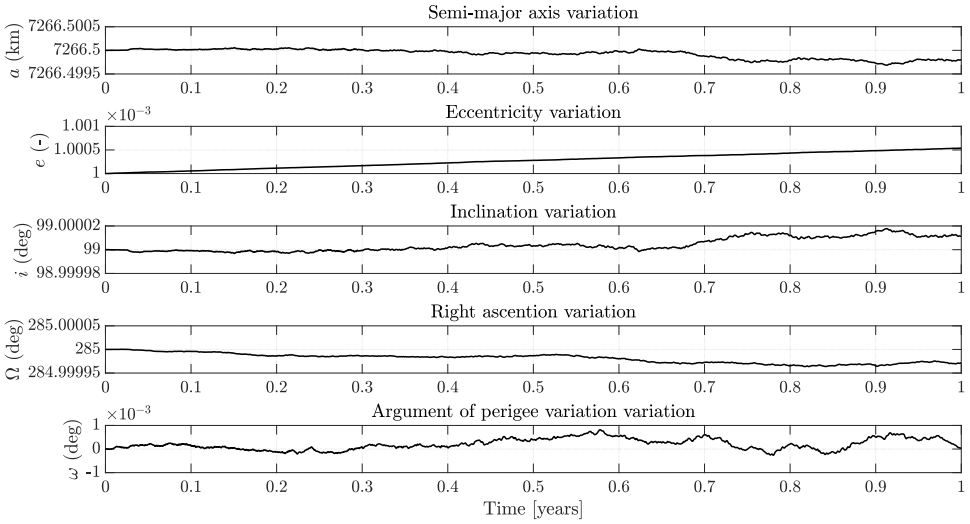

Figure 10.5: *Lift perturbative acceleration effect in 1 year. Initial epoch:* 21^{st} *of March* 2019.

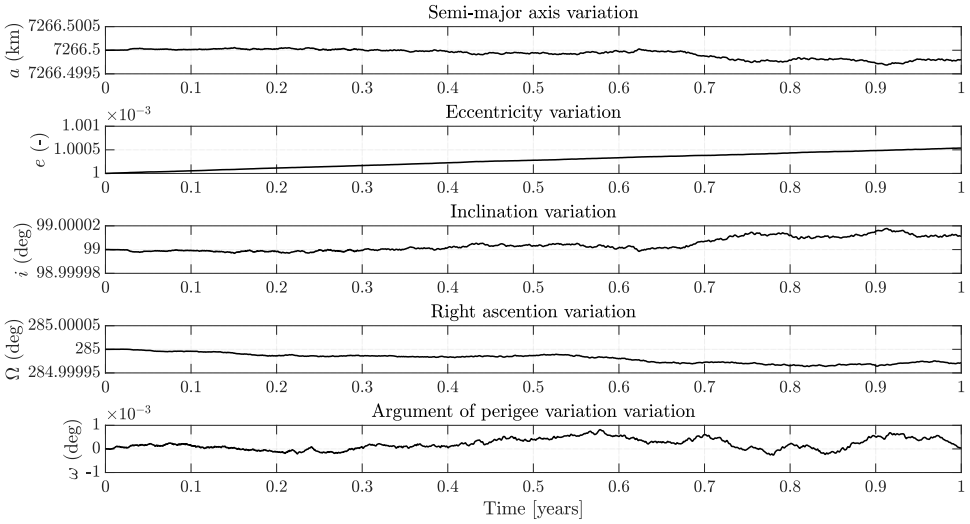

Figure 10.6: *Lift perturbative acceleration effect in 25 years. Initial epoch:* 21^{st} *of March* 2019.

Spinning balloon A possible strategy to increase the lift effect could be to spin the spacecraft along x-axis, maintaining it orthogonal to the direction of the relative

wind. In this way, according to the Kutta-Joukowski theorem, [12], it is possible to generate a lift:

$$F_{lift} = \frac{4}{3}(4\pi^2 R^3 s\rho||\boldsymbol{v_{rel}}||) \tag{10.3}$$

where s is the spinning velocity and R the balloon radius.

10.1.4 Effect of all the perturbations

It is important also to visualise the effect of all the perturbations considered (solar radiation pressure, drag, lift, Moon and Sun third body perturbations, Earth zonal harmonics) on the orbital evolution both in 1, Figure 10.7 and 25 years, Figure 10.8.

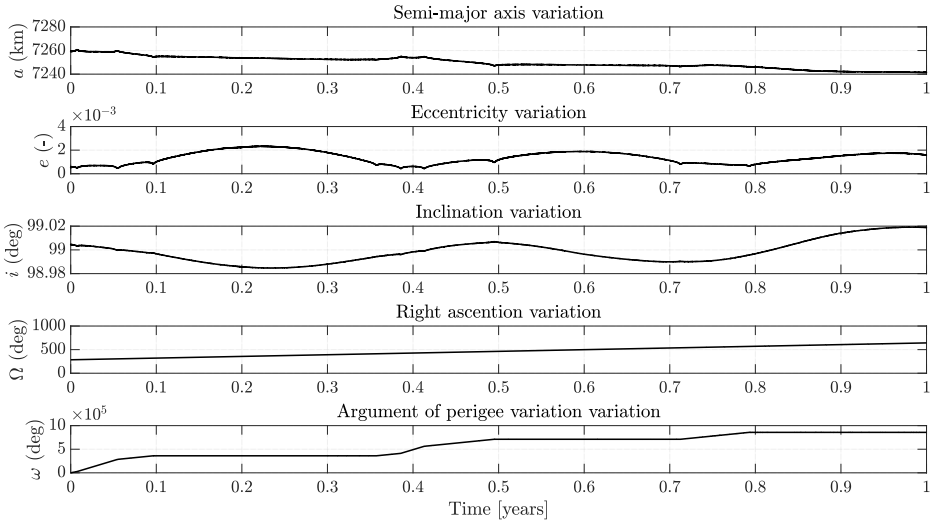

Figure 10.7: *All perturbative accelerations effect in 1 year. Initial epoch:* 21^{st} *of March* 2019.

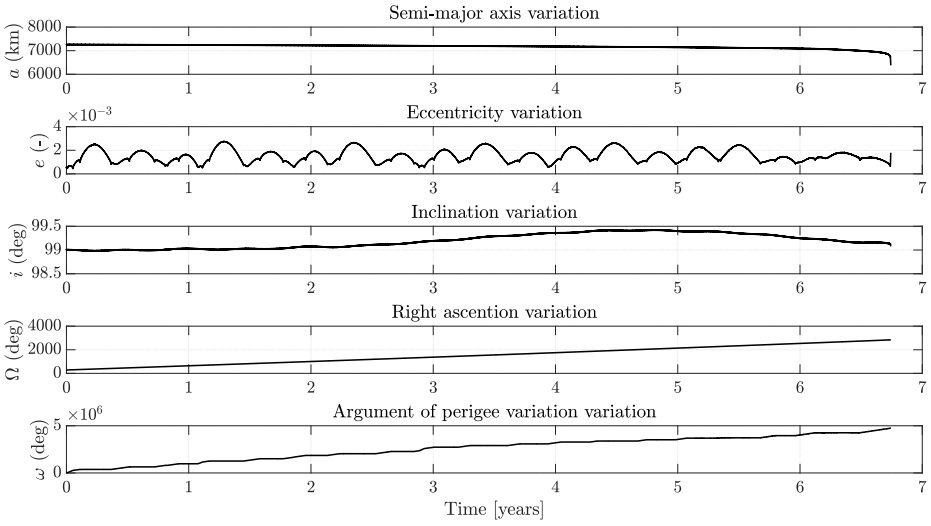

Figure 10.8: *All perturbative accelerations effect in 7 years. Initial epoch:* 21^{st} *of March* 2019.

All the plots presented in this chapter were obtained exploiting the *moving average filter technique* described in [61].

10.2 Quasi-frozen orbit under SRP and J_2 effect

The ZodiArt orbit does not change sensibly its inclination and eccentricity during the spacecrafts life-time, but it could be important for the mission to find a quasi-frozen orbit, with respect to both, SRP and J_2 perturbations, instead of only to J_2 effect, as done in [17]. In fact, from the mission analysis performed in [17], all the orbit keplerian elements result to be constrained by the mission requirements, but the anomaly of perigee, which could be treated as a degree of freedom for the selection of a quasi-frozen orbit.
In [62] it is reported a complete description of the effects of J_2 and SRP on planar and inclined orbits, in particular Figure 10.9 shows the eccentricity of the stationary points at $\phi = 0$ (bold continuous line) and $\phi = \pi$ (dotted and bold dashed lines) as function of the semi-major axis for different area-to-mass ratios and reflectivity coefficient of 1.8, where the blue line represents the J_2 case only. The ZodiArt mission, being characterised by a semi-major axis lower than 10^4 km and an area-to-mass ratio close to 3, is located close to the origin of the coordinate system. As a result, under the assumption of planar orbit, the equilibrium point is located at $\phi = 0$, where ϕ is the the angle between the Sun-Earth line and the direction of the orbit pericentre ($\phi = \omega + \Omega - (\lambda_{Sun} - \pi)$ where λ_{Sun} is the true longitude of the Sun), as shown in Figure 10.10.

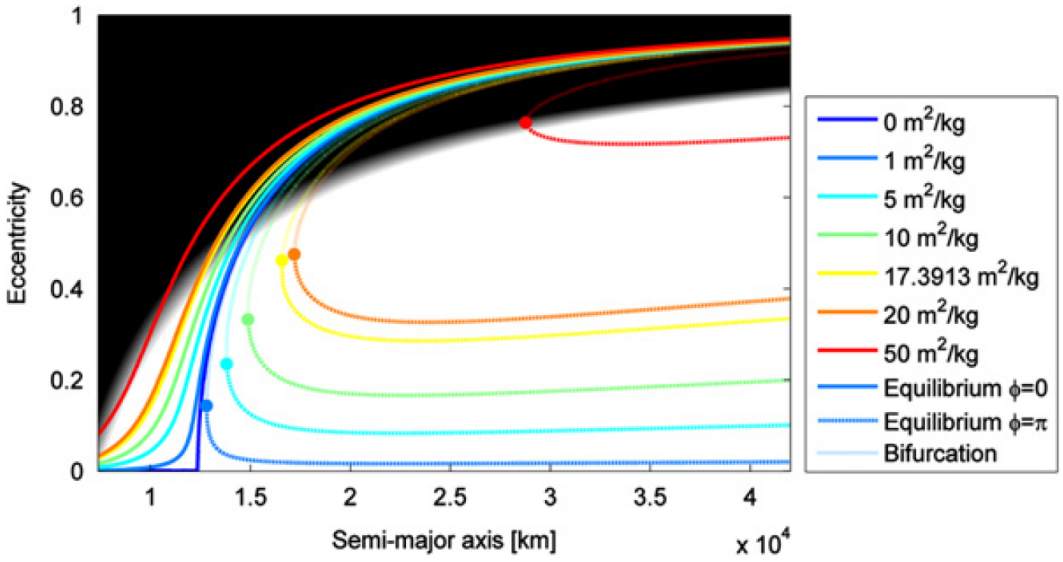

Figure 10.9: *Stationary points at $\phi = 0, \pi$ on planar orbits, [62]. The black part of the plot indicates eccentricities higher than the critical one, for which the orbit perigee is below the Earth radius.*

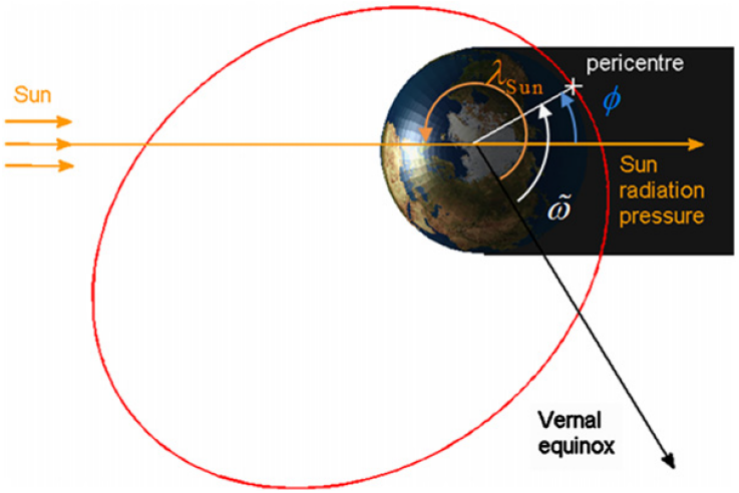

Figure 10.10: *Planar orbit geometry, [62], where $\tilde{\omega} = \omega + \Omega$.*

However, ZodArt orbit is characterised by a 99° inclination, meaning that the assumption of planar geometry has to be abandoned, in favor of a 3D description of the problem. The results evidenced in [62] and reported in Figure 10.11, on a different area-to-mass ratio satellite and semi-major axis, show that, increasing the inclination in correspondence of the $\phi = 0$ equilibrium, the eccentricity rises, but no quasi-frozen orbits exist for inclinations higher than 40°. As a result, for high inclination orbits, as for the ZodiArt one, there are no quasi-frozen orbits

with respect to J_2 and SRP. This result was proven analysing ϕ evolution in time, not evidencing oscillations around any equilibrium points.

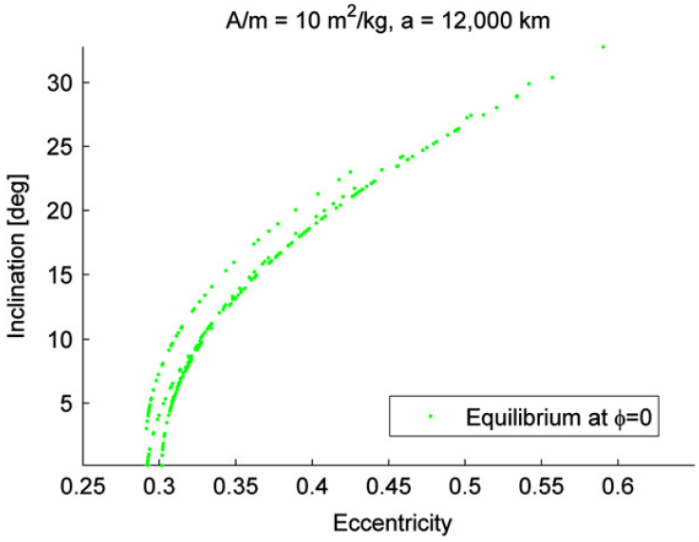

Figure 10.11: *Quasi-frozen orbits at non-zero inclination under SRP and J_2 for $A/m = 10$ m^2/kg and 12000 km, [62].*

10.3 Mission profile simulations

The balloon characterising the ZodiArt platforms is almost always visible from ground, due to the orbit selection and its high surface with respect to the one of the bus. For this reason, the position of the bus and, as a consequence, the overall attitude can vary without affecting the visibility of the constellation.
The real challenge for the ZodiArt mission is to counteract the uncommon drag and solar radiation torques on an 888 km high orbit, due to the peculiar shape of the platform. In fact, without the balloon surface and the huge distance between the center of pressure and the center of mass, drag could be almost negligible and SRP reduced in mangitude. The presence of such disturbances torques, decreases the time before saturation of the reaction wheels, meaning that it is not possible to maintain the platform 3-axis stabilised for long time periods.
Since the platform shall shoot pictures of the most important cities around the world while passing above them, [17], it is quite straightforward to consider as nominal mission profile a simple Nadir pointing 3-axis stabilized.
In order to size the actuators, the values from [17] were taken as first guess, as reported in Table 10.1 and Table 10.2:

Table 10.1: *Reaction wheels RSI 12, [63], characteristics.*

H (Nms)	**Torque** (Nm)	**Mass** (kg)	**Size** (mm)	**Power** (W)
12	0.075	4	247D x 85H	14

Table 10.2: *Magnetic torquers MT2502, [64], characteristics.*

Dipole (Am^2)	**Mass** (kg)	**Size** (mm)	**Power** (W)	
250	5.5	4	37D x 883H	14

The first set of simulations were performed maintaining the orbit and the attitude dynamics decoupled to check for simulator consistency, since the OUFTI-Next and the ZodiArt platforms belong to different spacecraft classes: the first one is a 3U CubeSat weighting 2.78 kg and the second is a MicoSat weighting 122 kg (20% margined) with an uncommon relative distance between the center of pressure and the center of mass.
The mission profile analysed is the following:

- De-tumbling phase with balloon stowed.
- Nadir pointing phase with balloon deployed, lasting till Reaction Wheels (RW) saturation.

10.3.1 De-tumbling model and results

During the de-tumbling phase, the spacecraft is assumed to have the balloon not yet inflated and the strategy adopted is exactly the same of the OUFTI-Next one, presented in Chapter 5, changing only the positive constant k_{DeT}, reported in Table 10.3. In order to find a suitable constant k_{DeT}, the value characterising the OUFTI-Next mission de-tumbling phase was increased till obtaining a magnetic torque close to saturation in the early phases of this mission phase: in this way the full potential of the torquers is exploited. The value of residual magnetic dipole is $\boldsymbol{m} = [1,\ 1,\ 1]$ Am^2, according to [65].

$$\boldsymbol{m} = -k_{DeT}\dot{\boldsymbol{B}}_{\boldsymbol{b}} \tag{10.4}$$

$$\boldsymbol{u} = \boldsymbol{m} \times \boldsymbol{B}_{\boldsymbol{b}} \tag{10.5}$$

where B_b is the magnetic field vector in *body-fixed reference frame*.

Table 10.3: *De-tumbling law positive constants.*

	OUFTI-Next	**ZodiArt**
K_{DeT}	10^5	10^7

The results are reported in Figures 10.12–10.13, which shows the angular velocities drop. The final angular velocities are $\boldsymbol{\omega} = [-3.592,\ -3.1897,\ 3.273] \times 10^{-4}\ rad/s$.

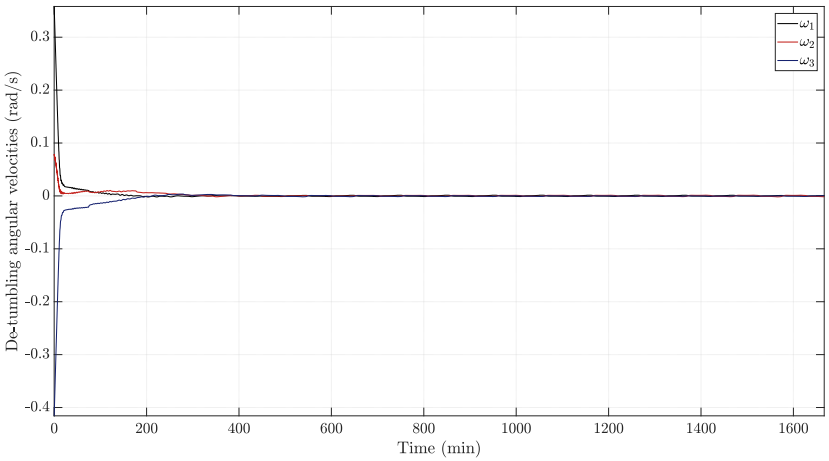

Figure 10.12: *Angular velocities de-tumbling in the ZodiArt mission. The detumbling time is almost 4 orbital periods.*

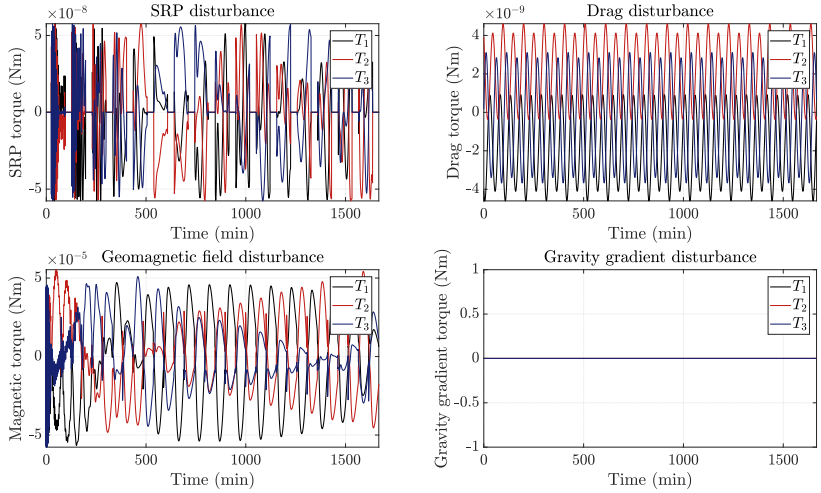

Figure 10.13: *Disturbances during de-tumbling phase in the ZodiArt mission. The detumbling time is almost 4 orbital periods. T_i are the torques components in body-fixed reference frame.*

From Figure 10.13 it is evidenced that gravity gradient is null, because under the assumption of uniform mass distribution, Eq. (10.6), the gravity gradient equation, Eq. (10.7) is driven to zero.

$$I_1 = I_2 = I_3 \tag{10.6}$$

$$\boldsymbol{T_{gravity}} = \int_M \begin{bmatrix} (y^2 - z^2)c_2c_3 \\ (z^2 - x^2)c_1c_3 \\ (x^2 - y^2)c_1c_2 \end{bmatrix} dm = \frac{3\mu}{R^3} \begin{bmatrix} (I_3 - I_2)c_2c_3 \\ (I_1 - I_3)c_1c_3 \\ (I_2 - I_1)c_1c_2 \end{bmatrix} = \mathbf{0} \tag{10.7}$$

It is important to remark that the angular velocities trend, evidenced in Figure 10.12, is slightly different from the one of the OUFTI-Next mission. This is due to the distribution of mass and geometry of the ZodiArt platform, which is a cube assumed to have a uniform mass distribution. Indeed, according to Eq. (10.6), the Euler equations, Eq. (2.11), are simplified with respect to the OUFTI-Next mission case:

$$\begin{cases} \dot{\omega}_1 = \frac{I_2 - I_3}{I_1}\omega_2\omega_3 + \frac{u_1 + d_1}{I_1} \\ \dot{\omega}_2 = \frac{I_3 - I_1}{I_2}\omega_1\omega_3 + \frac{u_2 + d_2}{I_2} \\ \dot{\omega}_3 = \frac{I_1 - I_2}{I_3}\omega_2\omega_1 + \frac{u_3 + d_3}{I_3} \end{cases} \rightarrow \begin{cases} \dot{\omega}_1 = \frac{u_1 + d_1}{I_1} \\ \dot{\omega}_2 = \frac{u_2 + d_2}{I_2} \\ \dot{\omega}_3 = \frac{u_3 + d_3}{I_3} \end{cases} \tag{10.8}$$

10.3.2 Nadir-pointing

The control strategy for what concerns the Nadir-pointing phase is the same of the OUFTI-Next mission, presented in Chapter 5. The most relevant results in terms of angular rates, quaternions, control action and pointing error, are reported in Figures 10.14–10.15, obtained performing Nadir pointing till saturating the wheels. The time taken is almost one orbital period.

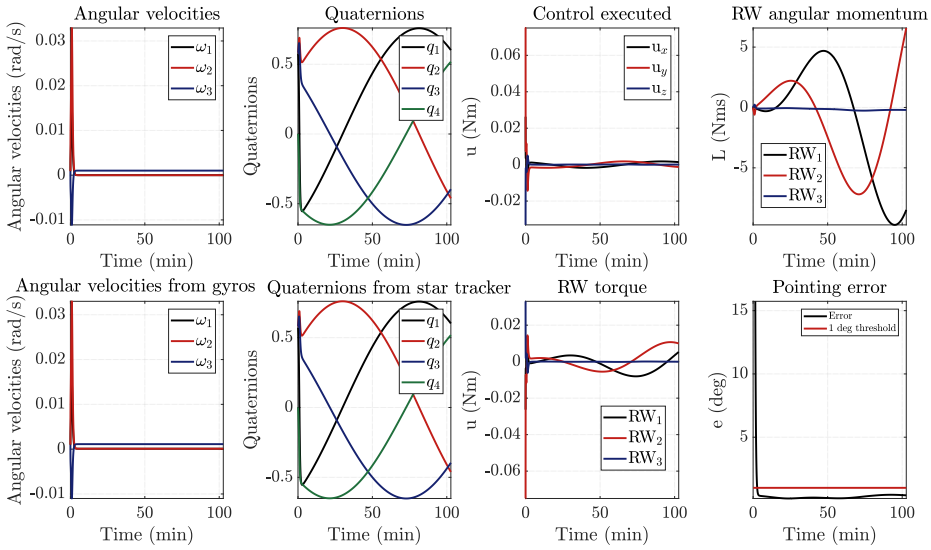

Figure 10.14: *The ZodiArt mission Nadir pointing main results. The plots are zoomed to evidence the most relevant trends, which are the transient phases. The saturation time is the 90% of one orbital period. Here the symbol e indicates the pointing error and not the orbital eccentricity.*

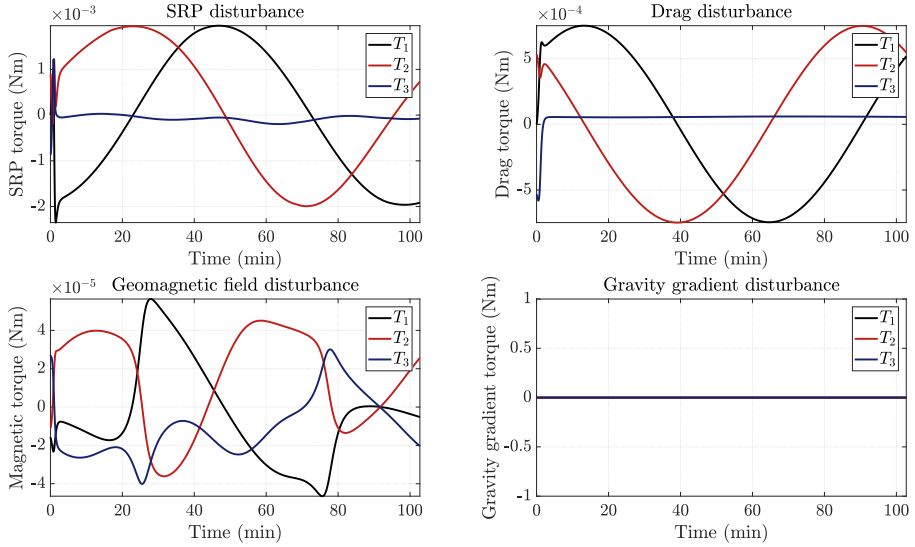

Figure 10.15: *The ZodiArt mission Nadir pointing main disturbances. T_i are the torques components in body-fixed reference frame.*

These results were achieved optimising the control parameters, K_p and K_d, in Eq. (2.83), using a multi-objective optimisation, based on *gamultiobj.m* by Mathworks^{TM}, minimising both the pointing error and the momentum stored by the wheels, using

the following set of cost functions:

$$\begin{cases} J1 = \int_{t_0}^{t_f} (pointing\ error - 0.1)^2 \, \mathrm{d}t. \\ J2 = \int_{t_0}^{t_f} (momentum\ stored)^2 \, \mathrm{d}t. \end{cases} \tag{10.9}$$

The optimised control parameters are:

$$\begin{cases} K_p = 0.3581 \\ K_d = 9.4073 \end{cases} \tag{10.10}$$

10.3.3 Decoupled orbit-attitude simulations conclusions

The results obtained once performed the nominal mission profile decoupled simulation are the following:

- De-tumbling can be performed in around 7 hours.
- Transient time before 3-axis stabilisation lasts 200 s.
- The actuators sized in [17] guarantee the pointing accuracy requested.
- The sensors chosen for the OUFTI-Next mission guarantee that the pointing error is maintained under 1 °.
- Saturation time is 1 h 55 min

CHAPTER 11

COUPLED ORBITAL-ATTITUDE DYNAMICAL ENVELOPES

The only coupling elements in the physical problem under investigation are atmospheric drag, lift and solar radiation pressure, since they produce a net force perturbing the orbit depending on the attitude. This effect was considered negligible in the OUFTI-Next mission, since its exposed surfaces are order of magnitudes less than the ones characterizing the ZodiArt platforms. Actually also for MicroSat like the ZodiArt platforms, the coupling can be neglected, since the balloon attitude do not affect at all the orbital dynamics and no lift is experienced by a non rotating sphere and the drag force is equal in every relative position with respect to the atmospheric wind. This scenario would completely change if the platforms would embark solar sails instead of the balloon on a lower altitude orbit: in that case, the change in the atmospheric and solar wind exposed surfaces would drive both the attitude and the orbital motion, since the sail can be considered as an aerodynamic profile. Nevertheless, the breakthrough challenge of the ZodiArt iSEE mission is to to fly a constellation of MicroSat in formation, with peculiar morphologic characteristics, due to the balloons presence, close to each other, in order to be recognised from ground as an artificial constellation. This means that high precision relative motion among the platforms is requested and even

if a formation flying control logic is beyond the aim of this Thesis, the reduced coupling between attitude and orbital dynamics was inspected and simulated to evidence possible opportunities and criticalities. In this chapter, the dynamics of the platform will be discussed in different perturbed scenarios, characterised by Earth zonal harmonics, Moon and Sun third body perturbations, Solar Radiation Pressure, drag and lift effects, with the aim to build an *orbital long-track envelope*, useful to plan attitude manoeuvres, capable of performing fine relative positioning in the context of formation flying. Obviously at lower altitudes the perturbation would be strong enough to make useful to build also a *cross-track envelope*, but this is not the case.
Before going into the details of the analysis, one basic concept has to be remarked: with respect to a reference configuration, the platform configuration with the maximum area exposed to the atmospheric and solar wind lowers the orbit semi-major axis, due to the resulting increase of drag and solar radiation pressure, while the one exposing the minimum area lowers it. According to elementary orbital dynamics, if two bodies are orbiting with different altitudes around the same attractor, they will experience a long-track drift, proportional to the difference in altitude. In particular the body characterised by an higher orbit will shift in the backward direction with respect to the other body and viceversa.
Performing differential drag/lift, means that the satellite will be exposed to the relative atmospheric wind, in order to achieve a desired long-track position and a certain altitude with respect to an other orbiting body, which, in this case, is another satellite of the constellation. Nevertheless, the same concept can be applied to the solar radiation pressure.

11.1 Differential drag/lift

Usually in literature the most exploited natural perturbation to control a spacecraft is the atmospheric drag only, as reported for instance in [5]. In the Thesis both lift and drag were considered and their effects were evaluated performing many simulations, varying:

- The initial epoch, spanning from the 6^{th} of December 2018 to the 21^{st} of November 2019, with a time interval of 15 days.
- The cross exposed area, spanning from 0° to 90° the bus inclination with respect to the velocity vector, since the balloon exposed surface is always the same.

with respect to a reference configuration attitude, inclined of 45°, over one orbital period. The results are collected in Figure 11.1, that represents the *Orbital long-track envelope*, showing the differential height and shift achieved performing a

differential drag/lift manoeuvre, under the effect of all the previously mentioned perturbances, at different epochs, in function of the platform angle of attack and given the initial true anomaly.

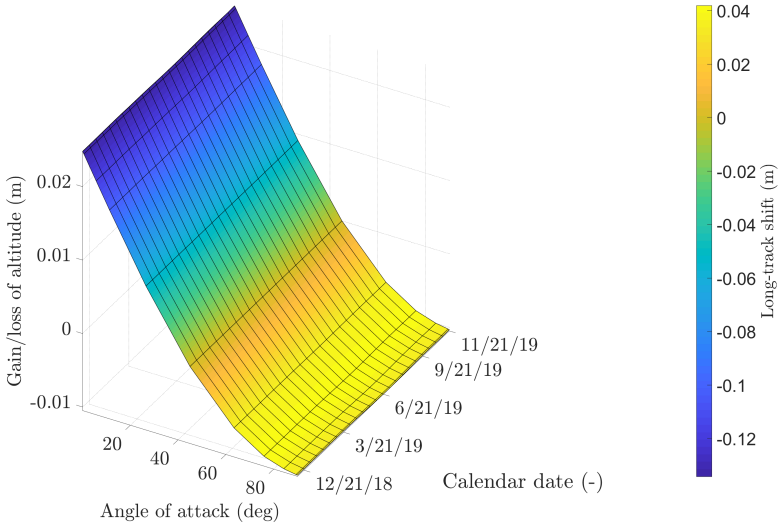

Figure 11.1: Orbital long-track envelope *related to drag/lift effects only.*

Figure 11.1 also evidences, as expected, that differential drag/lift is independent on the initial epoch. Moreover, the gain in altitude, and the consequent backward shift, are higher with respect to the altitude loss and advancing shift. This is due to the fact that, in the first case, the dynamics is evolving in the same direction of drag, while in the second case it is counteracted by the atmospheric wind.
The increase/decrease in altitude after one period is quite small compared to the one achievable at lower orbits, with solar sails, but it can be still exploited, especially if the differential drag manoeuvre lasts longer. Unfortunately, the simulations performed with the decoupled simulator evidenced that the saturation time is almost one period, meaning that, once reached the maximum momentum storable by the wheels, a de-saturation manoeuvre has to be performed, discretising the differential drag manoeuvre, making it even less efficient. Another option could be to accept a small error in the pointing accuracy, while the spacecraft is experiencing saturation and continue to increase/decrease the altitude. This technique will be inspected later in this chapter.

11.2 Solar radiation pressure

Solar radiation pressure effect is strictly related to the Sun position with respect to the orbital plane, resulting in an high dependence on the initial epoch. The

very same set of simulations were performed also in the case of only solar radiation pressure effect, resulting in a more complex dynamics, due to the fact that the exposed surface orientation is not optimised to point the Sun, but it is oriented almost towards the relative atmospheric wind. The results achieved are shown in Figure 11.2.

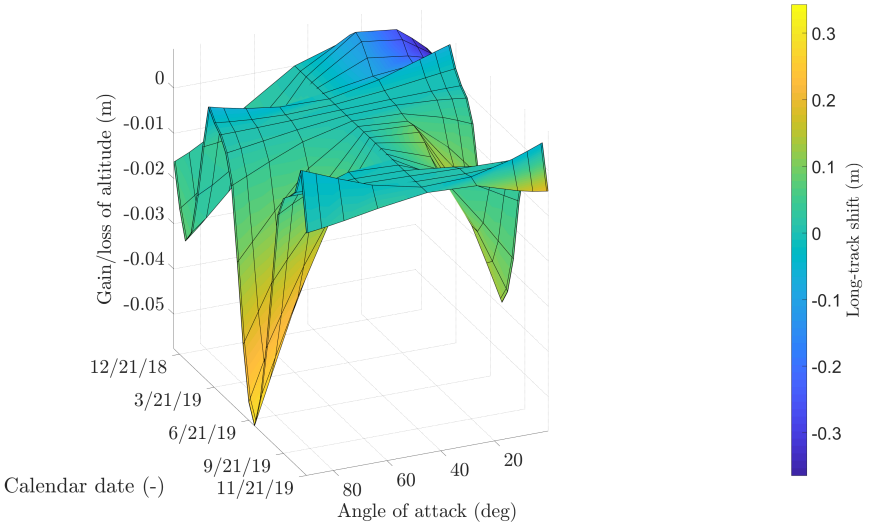

Figure 11.2: Orbital long-track envelope *related to solar radiation pressure effect only. The spacecraft, at the beginning of the manoeuvre, is characterised by declination almost null in eclipse.*

It is possible to notice that, close to the spring and autumn equinoxes, the effects of the solar radiation pressure are the lowest, since the Sun is almost orthogonal to the orbital plane, acting mostly on the cross-track orbital evolution, rather than the long-track one.
However, the most interesting effect that the plot evidences, is that the gain/loss in altitude, and correspondent shift, experienced close to the summer solstice are not the same evidenced during the winter solstice. Close to these two dates, the orbit is half in light and half in eclipse, with the Sun illuminating one of the two orbital semi-circumferences depending on the date considered and, according to this scenario, the spacecraft dynamics should be the same. Nevertheless, what is changing is the illumination condition of the satellite when the manoeuvre starts: in the case reported in Figure 11.2, during the summer solstice, the ZodiArt platform begins its manoeuvre in eclipse, with declination almost null, meaning that, after less than a quarter of orbit, it will start to experience solar radiation pressure, accelerating while covering the illuminated part of orbit, and finally continuing to slightly move in the direction of perturbation once entered in eclipse, due to the inertia acquired. During the winter solstice, on the contrary, the spacecraft

is characterised by almost null declination but it is in Sun-light, meaning that the perturbative acceleration will affect the spacecraft for slightly more than a quarter of orbit, then it will enter in eclipse and finally it will experience again the solar wind pressure. This means that, in the second case, the platform can not continuously accelerate in the illuminated half of orbit, resulting in a reduced gain/loss of altitude.
The proof of what just discussed can be find varying the initial true anomaly, as shown in Figure 11.3. The results are reported in Figure 11.4.

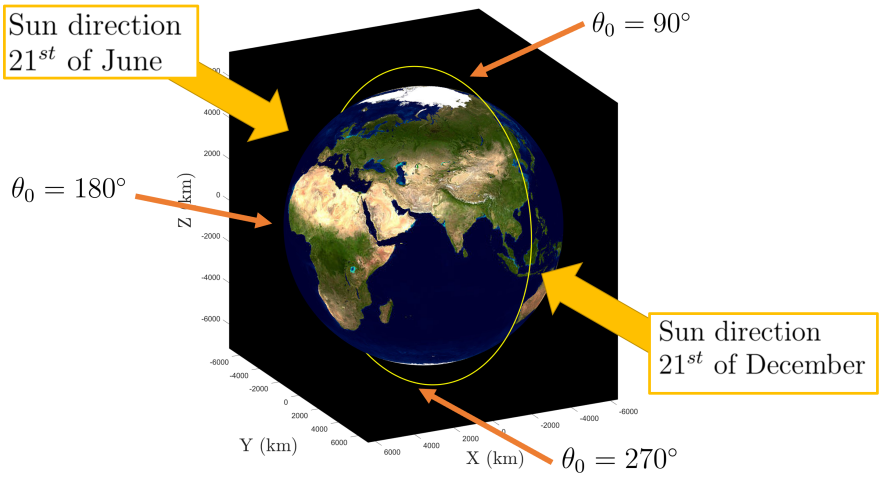

Figure 11.3: *Orbit and platform Sun exposition depending on θ_0 and date.*

In particular:

- At $\theta_0 = 90°$, the 21^{st} of June 2019, the platform starts the manoeuvre just at the end of the eclipse, maximising the acceleration due to SRP and, as a result, the deepest peak is reached.
- At $\theta_0 = 180°$, the dynamics is exactly the opposite of the one shown in Figure 11.2, since the spacecraft has declination almost null, but starts the manoeuvre 180° after on orbit.
- At $\theta_0 = 270°$, the dynamics is the opposite to the $\theta_0 = 90°$ case, since the spacecraft can exploit the overall perturbative acceleration only during the winter solstice.

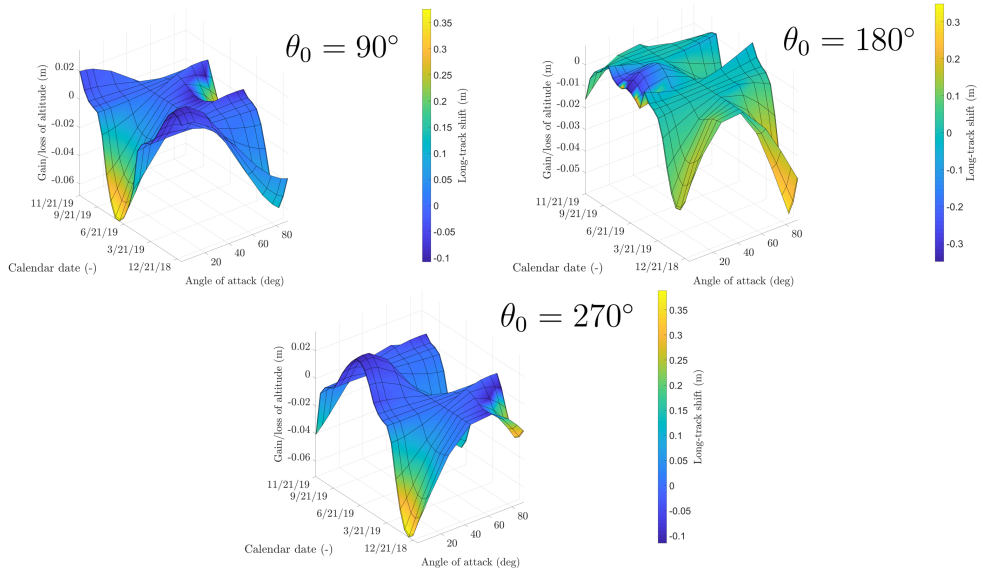

Figure 11.4: Orbital long-track envelope *related to solar radiation pressure effect only at different initial true anomalies,* θ_0.

11.3 Solar radiation pressure and drag/lift effects

In Section 11.2 it was shown that solar radiation pressure is the perturbative acceleration that mostly affect the differential dynamics, but in the case of equinoxes, when the Sun direction is almost orthogonal to the orbital plane, differential drag and lift are the main actors rising and lowering the altitude. In Figure 11.5, the cumulative effects of SRP and drag/lift are reported referred to null initial true anomaly.

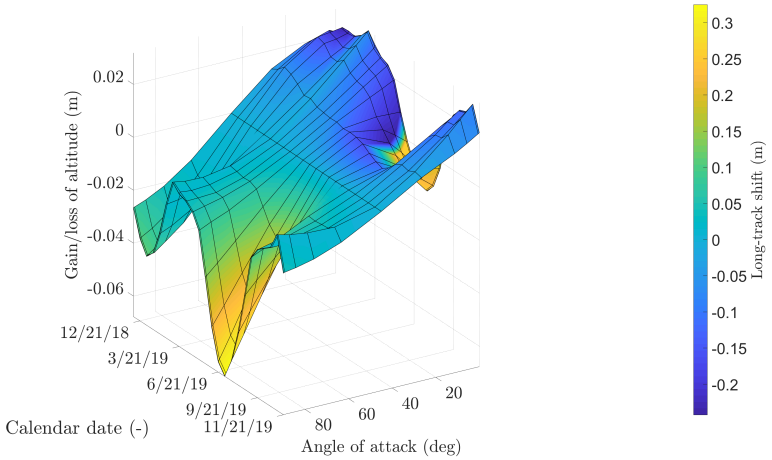

Figure 11.5: *Orbital long-track envelope related to solar radiation pressure and lift/drag effects. Initial true anomaly,* θ_0

It is possible to appreciate that, in correspondence of equinoxes, the gain and loss in altitude are the same achievable with differential drag only, while in the remaining periods of the year, SRP is the driving perturbation. In the case of different initial true anomalies, the same trend evidenced with the *solar radiation pressure long-track envelopes* is obtained.

11.4 Long-term differential drag

In this chapter it has been demonstrated that, during equinoxes, differential drag can be exploited, independently from SRP, to control the spacecraft. However, the differential height and shift acquired are quite small compared to the ones achievable at lower orbits and equipped with solar sails. For this reason, long-term differential drag/lift manoeuvres can be inspected to increase the effects of these perturbation.
In order to test one of these manoeuvres, a reference scenario was selected: three simulations, with the same initial condition but the initial orientation with respect to the velocity vector ($\boldsymbol{q_0}$), were performed over 10 periods with initial epoch at the apring equinox. In particular:

- The *reference configuration*: tilted of 45° with respect to the velocity vector.
- The *advancing configuration*: characterised by the maximum exposed surface, which will lower the altitude and shift in the same direction of velocity vector.
- The *receding configuration*: characterised by the minimum surface exposed, which will rise the altitude and shift in the opposite direction of velocity vector.

Together with SRP and drag/lift, also Earth oblateness and Moon/Sun third body perturbation were considered. During the manoeuvre, all the three spacecrafts experience saturation of the wheels, resulting in loss of pointing accuracy when the reaction wheels (RWs) cannot provide the desired torque anymore. This dynamics is shown in Figure 11.6, where the plots in the first line represent the reaction wheels angular momenta, while the ones on the second raw, the pointing error. Here the symbol e indicates the pointing error and not the orbital eccentricity

In order to help the reader to visualise the scenario, an animation performed with STK by AGI was created, animating the results obtained in Matlab^{TM}. In Figure 11.7 a frame is shown, representing the three platform configurations position after 10 orbits, while in Figures 11.8–11.9, the resulting shifts are reported.

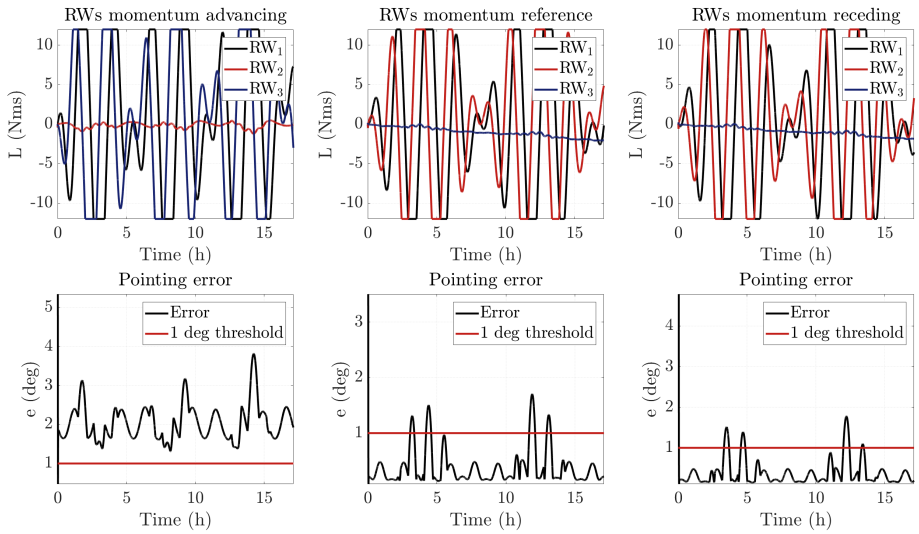

Figure 11.6: *Saturation during 10 periods performing differential drag and pointing error.*

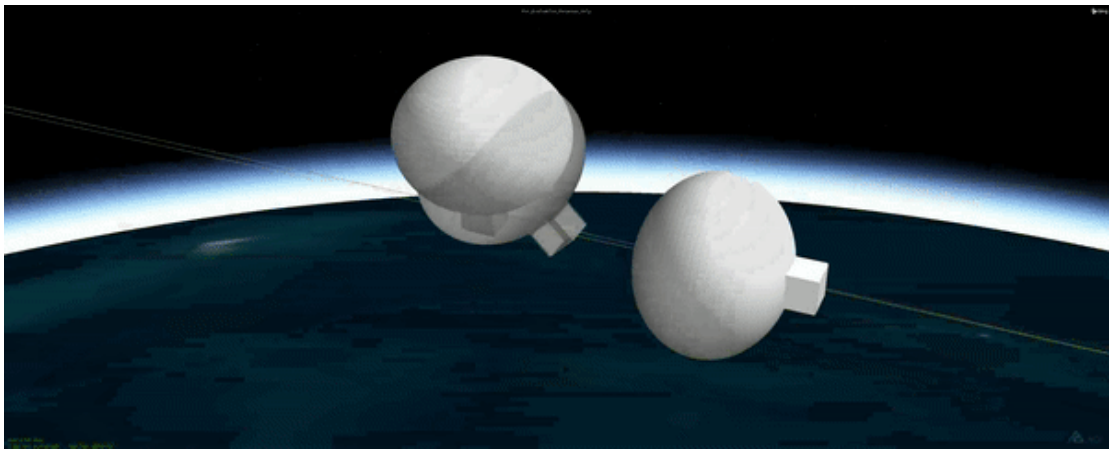

Figure 11.7: *STK by AGI animation over 10 orbits. The transparent platform is the* reference configuration *tilted of* 45° *in the direction of the velocity vector. If supported by the pdf reader used, it is possible to animate it by clicking on the image.*

Moreover, the same behavior evidenced in Figure 11.1 is evidenced also in this case: the platform rising its orbit acquires more height in altitude with respect to the the one lost by the platform lowering its orbit, because, in the first case, the dynamic evolution is in the same direction of drag action, while, in the second case, it is partially counteracted by drag and lift. In conclusion, performing a manoeuvre lasting 10 periods it is possible to achieve a gain in altitude of 0.29 m, with a correspondent backward shift of -12.6 m, and a loss in altitude of -0.12 m, with a frontward shift of 3.9 m, with respect of the orbital motion.

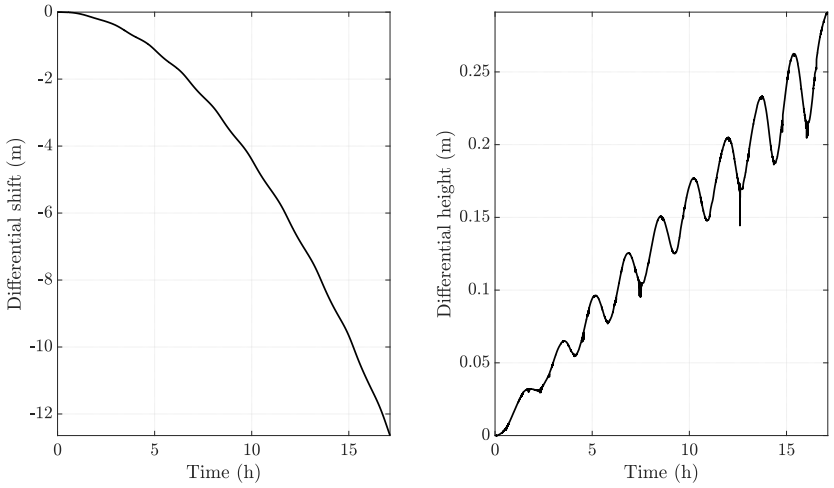

Figure 11.8: *Receding configuration gain altitude and shift in 10 periods.*

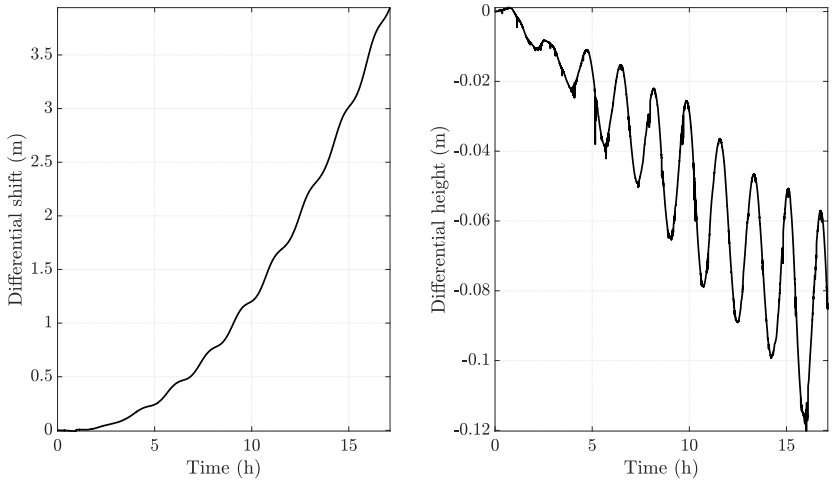

Figure 11.9: *Advancing configuration gain altitude and shift in 10 periods.*

CHAPTER 12

THE ZODIART ISEE MISSION CONCLUSIONS

12.1 Results achieved

THANKS to the work done on the ZodiArt iSEE project it was possible to test the coupled simulator, characterised by the presence of all the major disturbances experienced on orbit and capable to handle also the low and fine coupling between attitude and orbital dynamics in the ZodiArt mission. Moreover, in Section 10.1 Earth zonal harmonics till the 7^{th} order, Sun and Moon third body perturbation, drag, lift and solar radiation pressure disturbances were introduced and added to the evolution of the orbit designed in [17], based on Earth J_2 effect only. An analysis on the effect of each perturbative force on orbit evolution was performed, also evidencing the Keplerian parameters evolution in time. Then, a fully perturbed orbital propagation was evaluated, in order to check for the 25 years de-orbit IADC Space Debris Mitigation Guidelines, [47], which resulted to be fulfilled, being the de-orbit time around 7 years. Finally it was demonstrated that no quasi-frozen orbits with respect to both J_2 and SRP do exist.
The ZodiArt platform was characterised by a reflective balloon instead of a flat or pyramidal sail, in order to be always visible from ground without any active

attitude control. This choice revealed to be the best one in terms of control effort, even if, without a common sail, it is not possible to perform station keeping or large relative manoeuvres, exploiting perturbations. However, it is still possible to slightly rise and lower the orbit to shift long track the platforms, which could be useful, while flying in formation. The tool developed in Chapter 11 can provide *Orbital long-track envelopes*, representing the differential height and shift achieved performing a differential drag/lift manoeuvre under the effect of all the previously mentioned perturbances, at different epochs, in function of the platform angle of attack and given the initial true anomaly. Moreover, in the same chapter a simulation of a long-term manoeuvre, lasting 10 periods, was presented and animated with STK by AGI.

The most important remarks are here collected:

- The de-tumbling phase will last approximately 7 hours.
- The maximum time the spacecraft can remain Nadir pointing before saturating the reaction wheels is around 1 hour and 55 minutes.
- The sensors chosen for the OUFTI-Next mission guarantee that the pointing error is maintained under 1°.
- The platform will de-orbit in around 7 years.
- No quasi-frozen orbit with respect to J_2 and SRP can be found with an inclination of 99°. Nevertheless, the orbit selected in [17], does not change significally during the platform life-time.
- During equinoxes, with respect to a reference condition tilted of 45°, it is possible to obtain in the case of minimum surface exposed a gain in altitude of 0.29 m and a backward shift of -12.6 m, while a loss in altitude of -0.12 m and a frontward shift of 3.9 m can be achieved in the case of maximum surface exposed.
- Manoeuvring during solstices maximises the loss in altitude and correspondent forward shift.
- Accepting a pointing error of some degrees, it is possible to perform long-term differential drag/lift manoeuvres, increasing the platform shifts in altitude and in long-track distance.

Part IV

Conclusions

CHAPTER 13

CONCLUSIONS AND FUTURE DEVELOPMENTS

THE tool implemented in the Thesis is capable to simulate and size the ADCS of any kind of spacecraft, under the effects of the Earth zonal harmonics, the Moon and Sun third body perturbations, solar radiation pressure, atmospheric drag and lift, providing a complete disturbance model, including all the main environmental perturbations acting on a satellite. Moreover, the attitude and orbital coupling was not limited only to the atmospheric drag/lift or solar radiation pressure perturbative accelerations, but the three effects were analysed together, providing useful results in terms of precise relative positioning in formation flying environment, through compact plots, here called *Orbital long-track envelopes*, function of the initial epoch, the platform angle of attack and the initial true anomaly. The analyses performed were fundamental to size the OUFTI-Next and the ZodiArt ADCS and to simulate the missions nominal profiles, proving the tool robustness and versatility. The most relevant results about the two missions are collected in Chapter 8 and 12, respectively.

One of the limitations of the tool implemented are related to the computational power requested to perform and optimise long and complex mission profiles, as well as the absence of a user interface. A future development of the Thesis could

be the implementation of the simulator on a dedicated machine, interfaced with the ADCS components, and written in a lower-level programming language, such as C++, which has a more direct interaction with the hardware. Moreover, the tool does not provide a control strategy to efficiently exploit the perturbative forces with a control law. The next challenge could be to design a control strategy capable to perform relative navigation with respect to the other platforms, exploiting just the natural perturbations analysed in the Thesis. Finally the simulator can be improved including the sensors bias estimation performed by the Kalman filter and an orbital estimator.

Appendices

APPENDIX $\mathcal{A}$

QUATERNION INVERSE TRANSFORMATIONS

All the possible inverse transformations from quaternion to direction cosine matrices are:

$$\begin{cases} q_1 = \frac{1}{4q_4}(A_{23} - A_{32});\ q_2 = \frac{1}{4q_4}(A_{31} - A_{13});\ q_3 = \frac{1}{4q_4}(A_{12} - A_{21});\ q_4 = \pm\frac{1}{2}\sqrt{1 + A_{11} + A_{22} + A_{33}} \\ q_1^2 = \pm\frac{1}{2}\sqrt{1 + A_{11} - A_{22} - A_{33}};\ q_2^2 = \frac{1}{4q_1^2}(A_{12} + A_{21});\ q_3^2 = \frac{1}{4q_1^2}(A_{13} + A_{31});\ q_4^2 = \frac{1}{4q_1^2}(A_{23} - A_{32}) \\ q_1^3 = \frac{1}{4q_2^3}(A_{12} + A_{21});\ q_2^3 = \pm\frac{1}{2}\sqrt{1 - A_{11} + A_{22} - A_{33}};\ q_3^3 = \frac{1}{4q_2^3}(A_{23} + A_{32});\ q_4^3 = \frac{1}{4q_2^3}(A_{31} - A_{13}) \\ q_1^4 = \frac{1}{4q_3^4}(A_{13} + A_{31});\ q_2^4 = \frac{1}{4q_3^4}(A_{23} + A_{32});\ q_3^4 = \pm\frac{1}{2}\sqrt{1 - A_{11} - A_{22} + A_{33}};\ q_4^4 = \frac{1}{4q_3^4}(A_{12} - A_{21}) \end{cases} \tag{A.1}$$

APPENDIX B

THE OUFTI-NEXT SIMULATIONS RESULTS ON SSO

Mission 1 with Nadir pointing
Computational time usually requested: around 3 minutes, depending on the initial conditions.

De-tumbling After the de-tumbling phase, the angular velocities reached are:

$$\begin{cases} \omega_{b/n,1}(5000) = 1.016 \times 10^{-3} \text{ rad/s} \\ \omega_{b/n,2}(5000) = -7.080 \times 10^{-3} \text{ rad/s} \\ \omega_{b/n,3}(5000) = -4.435 \times 10^{-4} \text{ rad/s} \end{cases} \tag{B.1}$$

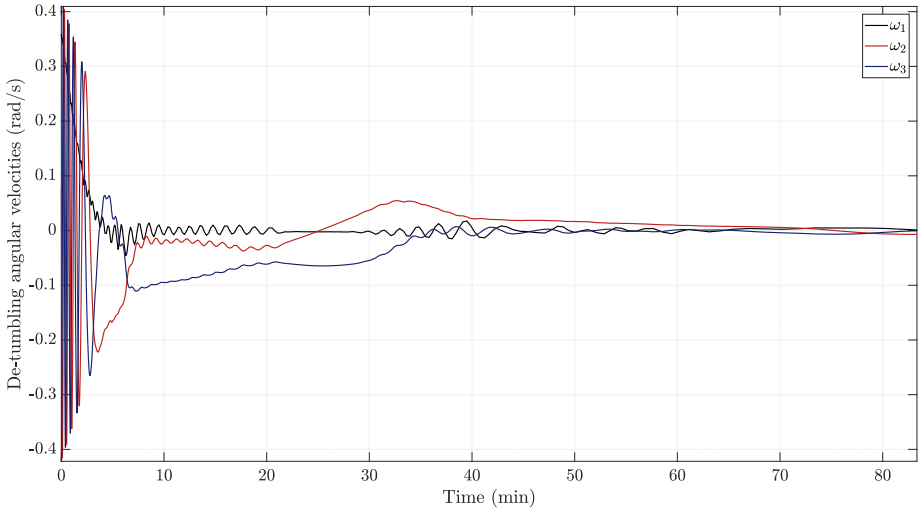

Figure B.1: *Angular velocities reduction during de-tumbling phase, in mission 1, on SSO.*

The disturbances experienced by the OUFTI-Next CubeSat are instead represented in Figure B.2. The solver relative tolerances was set to 10^{-3} just to speed up the simulation, since no lack of accuracy in the solution was evidenced.

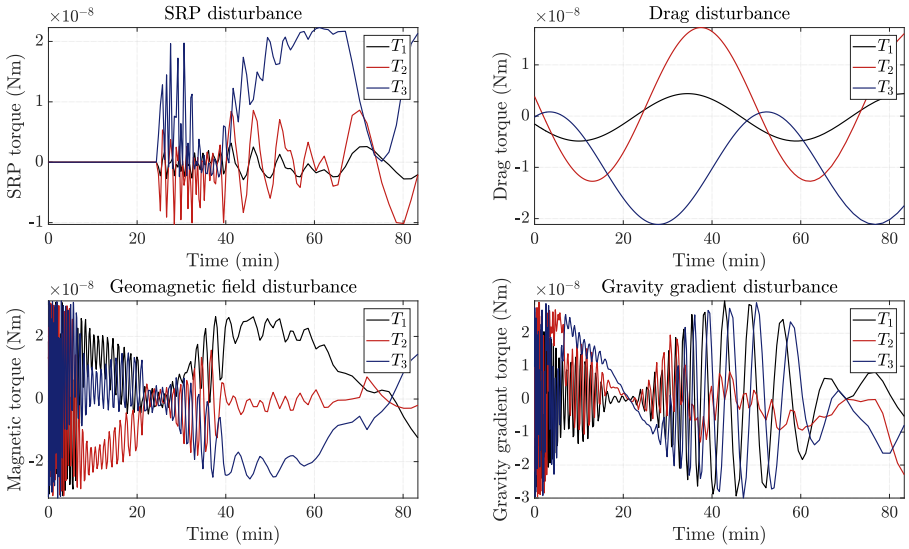

Figure B.2: *Main disturbances during de-tumbling phase, in mission 1, on SSO. T_i are the torques components in body-fixed reference frame.*

Sun-pointing 1 The phase lasts around 26.5 hours in total, 24 hours plus the time spent in orbit before arriving 30° from the National Park of Brasilia, and the solver absolute and relative tolerances were set to 10^{-6} both. The steady state is reached after around 100 seconds.

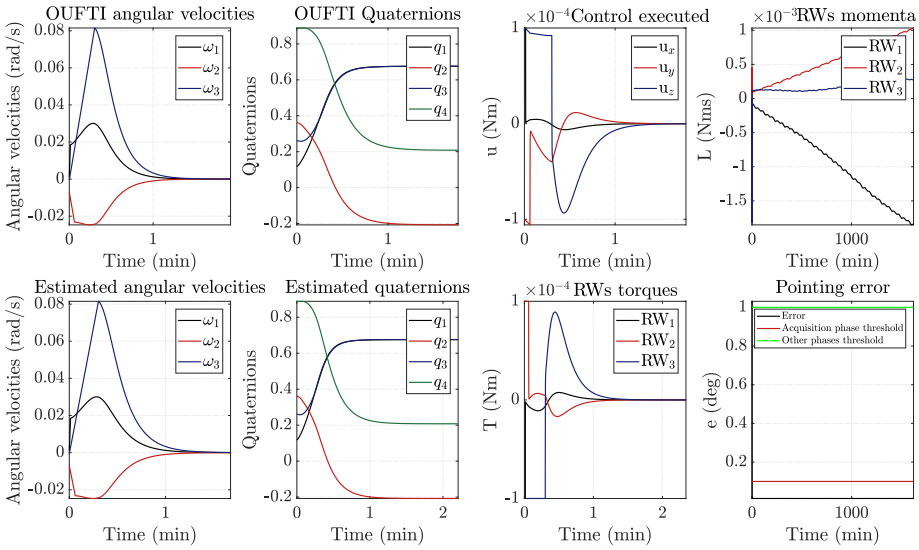

Figure B.3: *Most important results during Sun-pointing phase 1, in mission 1, on SSO. The plots are zoomed in order to catch the most interesting behaviors.*

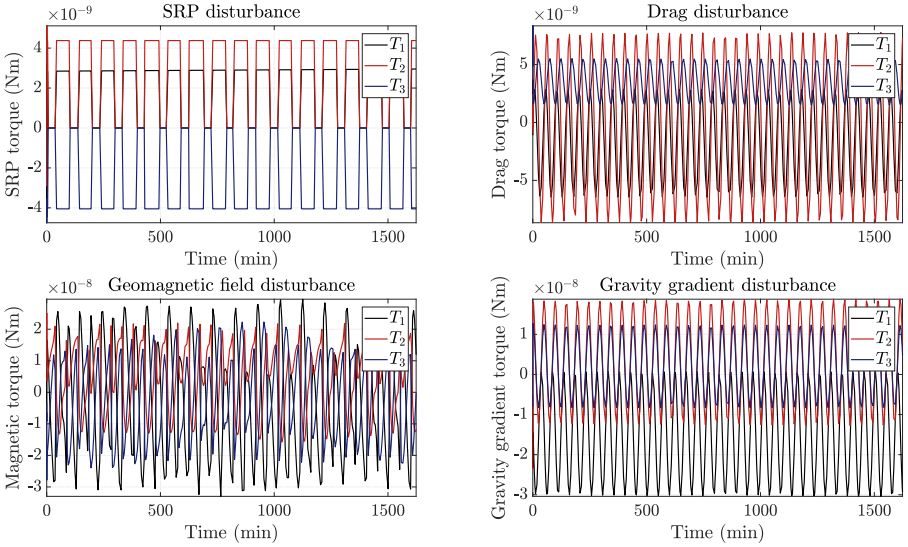

Figure B.4: *Main disturbances torques during Sun-pointing phase 1, in mission 1, on SSO. T_i are the torques components in body-fixed reference frame.*

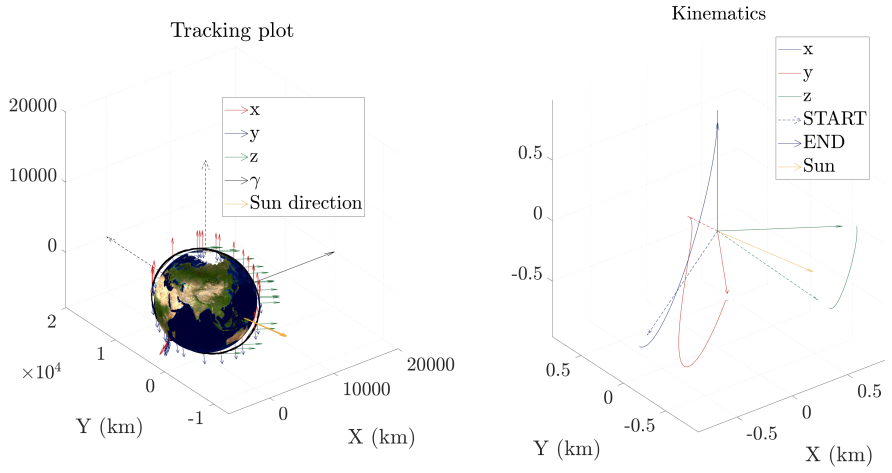

Figure B.5: *Body-fixed frame while orbiting around the earth during Sun-pointing phase 1, in mission 1, on SSO.*

De-saturation 1 The phase lasts 1 minute and the solver absolute and relative tolerances were set to 10^{-6} both. It is interesting to compare these results with the ones of de-saturation phase 2, when the CubeSat is in eclipse, Figure B.14. Figure B.6 proves that the platform will rotate very slowly independently from solar radiation pressure effect.

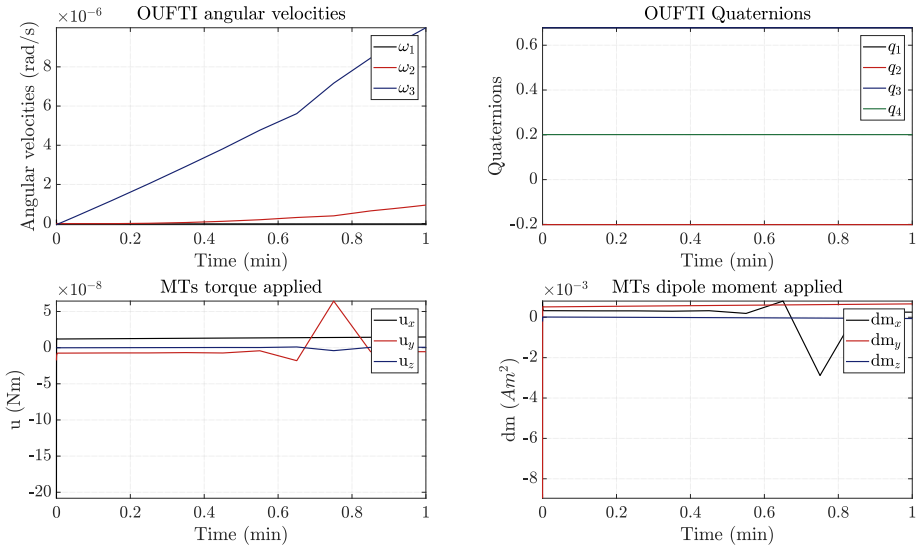

Figure B.6: *Most important results during de-saturation phase 1, in mission 1, on SSO.*

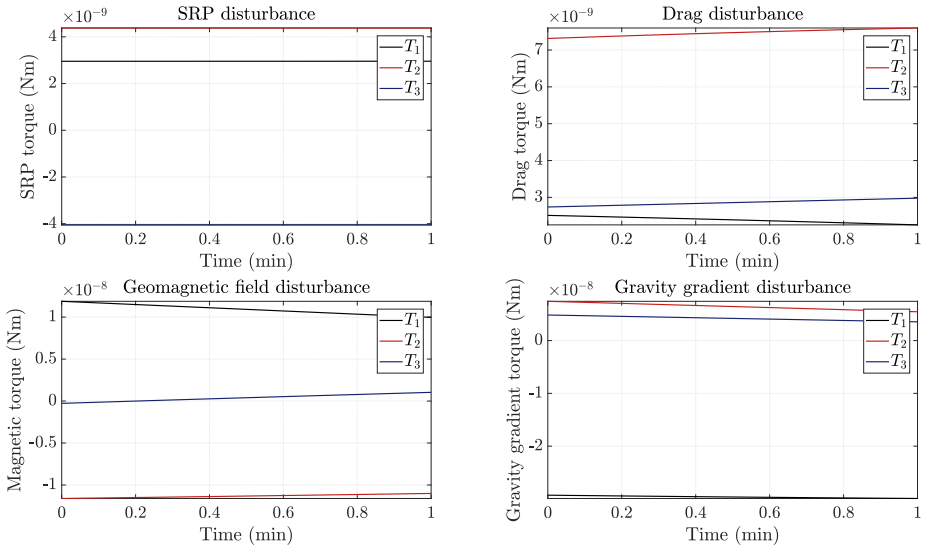

Figure B.7: *Main disturbances torques during de-saturation phase 1, in mission 1, on SSO. T_i are the torques components in body-fixed reference frame.*

Picture acquisition The picture acquisition phase in SSO requires the same pointing accuracy than the one in ISS orbit and, as shown in Figure B.8, the control action is able to maintain the pointing error below the 0.1° threshold, thanks to the control parameters optimisation.
The phase lasts around 15 minutes and the solver absolute and relative tolerances were set to 10^{-6} both. The steady state is reached less than 90 seconds.

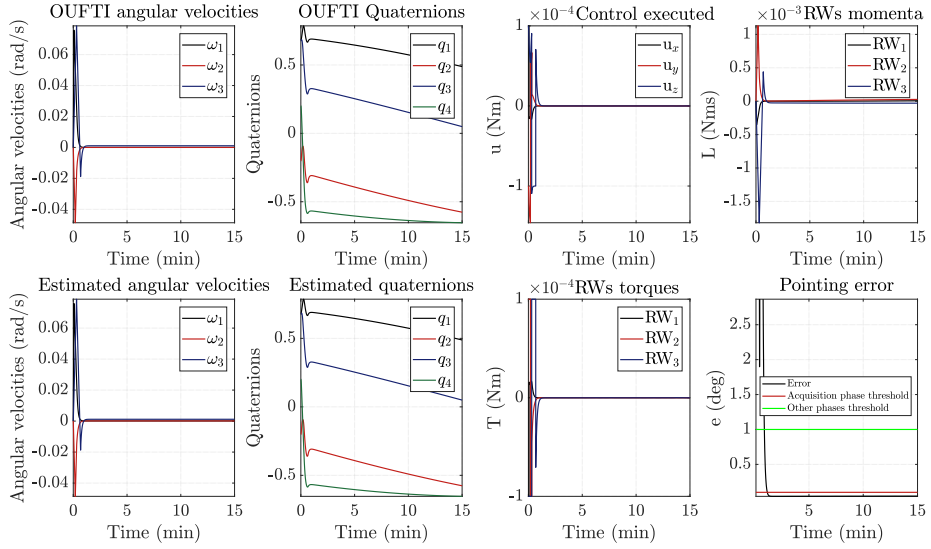

Figure B.8: *Most important results during Nadir pointing picture acquisition phase, in mission 1, on SSO. The plots are zoomed in order to catch the most interesting behaviors.*

From Figure B.8 it is also possible to appreciate how well the *unscented Kalman filter* estimates the state, comparing the integrated angular velocities and quaternion plots with the ones provided by the gyroscopes/star trackers and estimated by the filter.

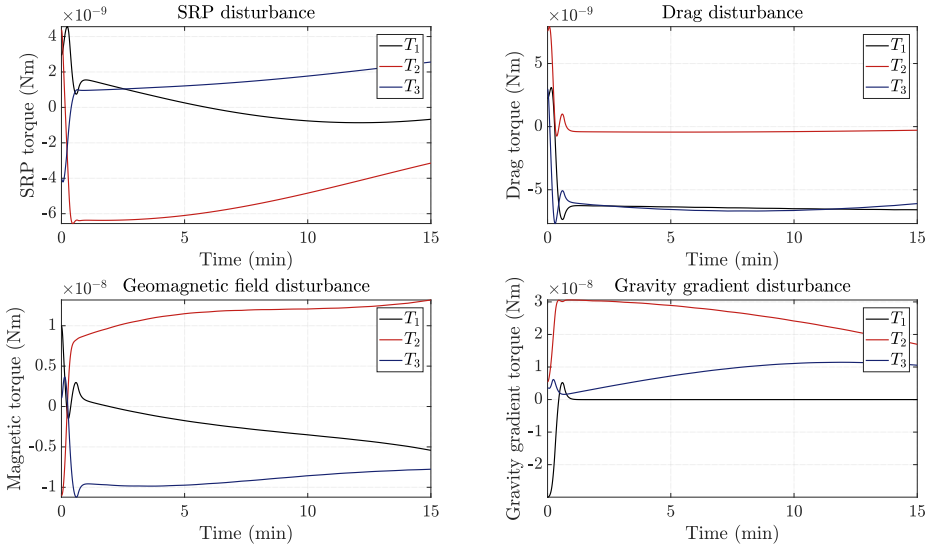

Figure B.9: *Main disturbances torques during Nadir pointing picture acquisition phase, in mission 1, on SSO. T_i are the torques components in body-fixed reference frame.*

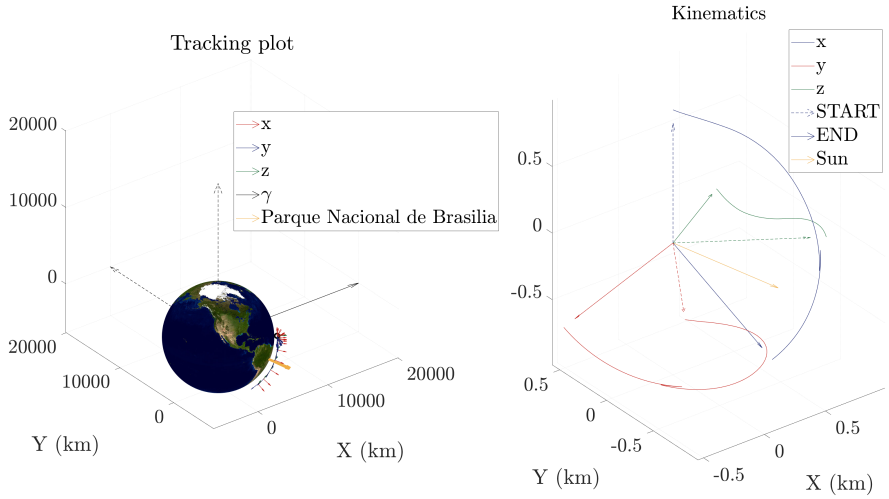

Figure B.10: *Body-fixed frame while orbiting around the earth during Nadir pointing picture acquisition phase, in mission 1, on SSO.*

Sun-pointing 2 This phase is quite similar to the previous ones in Sun-pointing. The phase lasts around 31.6 hours, the time needed to reach 10° from Liége, and

the solver absolute and relative tolerances were set to 10^{-6} both. The steady state is reached after around 80 seconds.

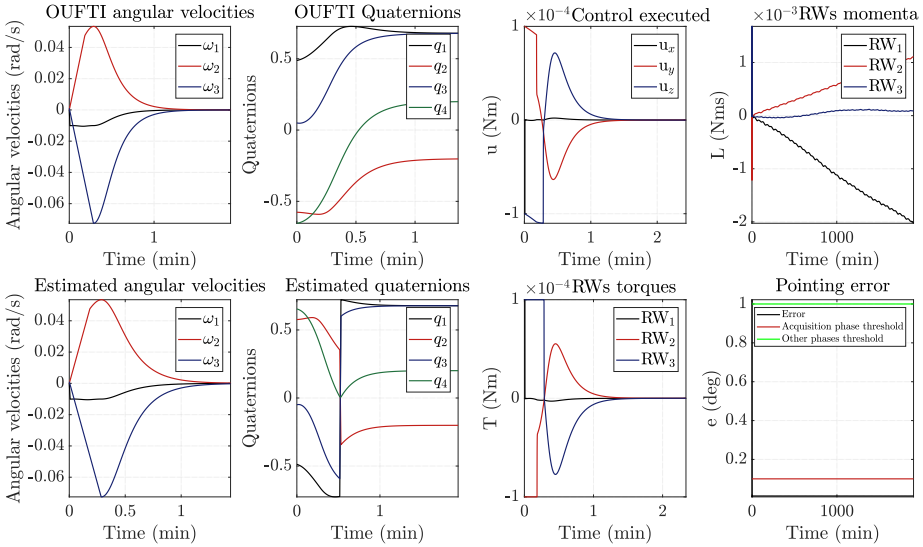

Figure B.11: *Most important results during Sun-pointing phase 2, in mission 1, on SSO. The plots are zoomed in order to catch the most interesting behaviors.*

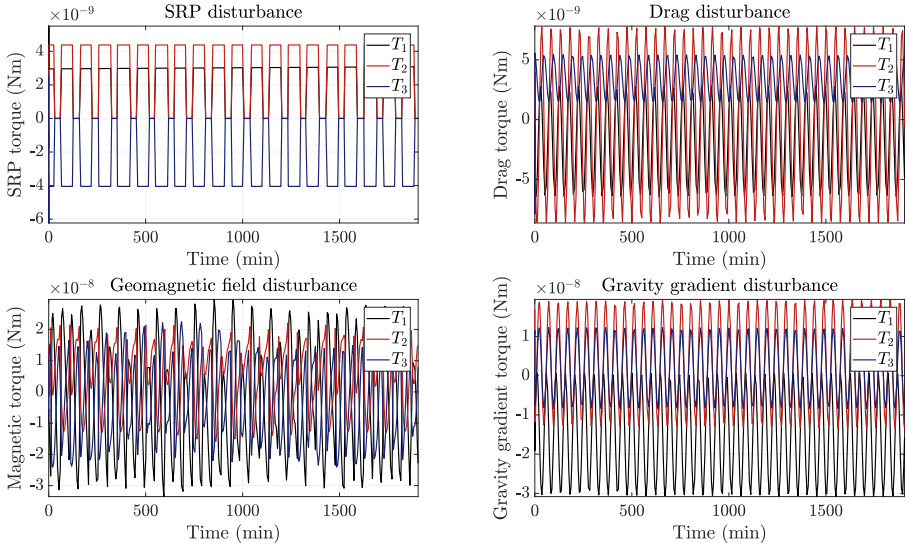

Figure B.12: *Main disturbances torques during Sun-pointing phase 2, in mission 1, on SSO. T_i are the torques components in body-fixed reference frame.*

De-saturation 2 These results are quite similar to the ones of the previous de-saturation phase and confirm that the spacecraft rotates very slowly.
The phase lasts 1 minute and the solver absolute and relative tolerances were set

to 10^{-6} both.

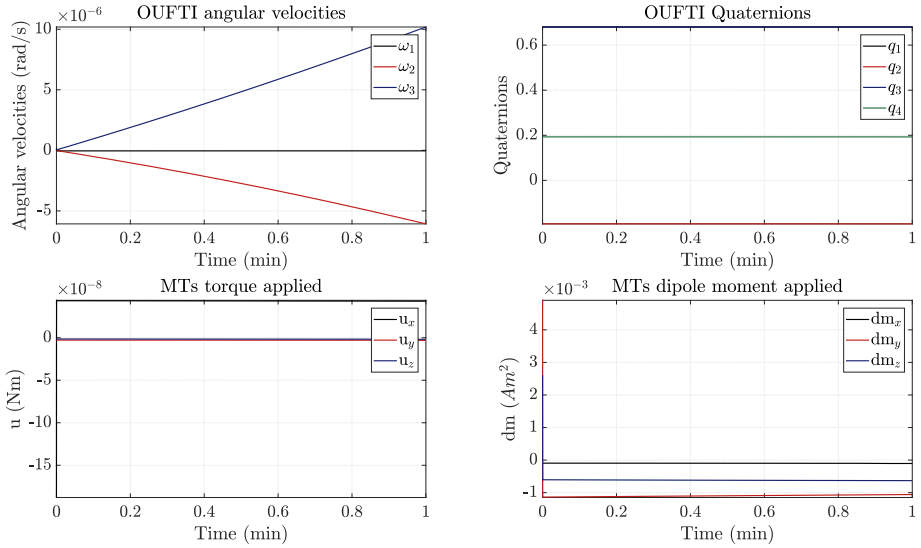

Figure B.13: *Most important results during de-saturation phase 2, in mission 1, on SSO.*

The peculiarity with respect to de-saturation phase 1 is that it occurs in eclipses, as it can be seen from the solar radiation pressure plot in Figure B.14.

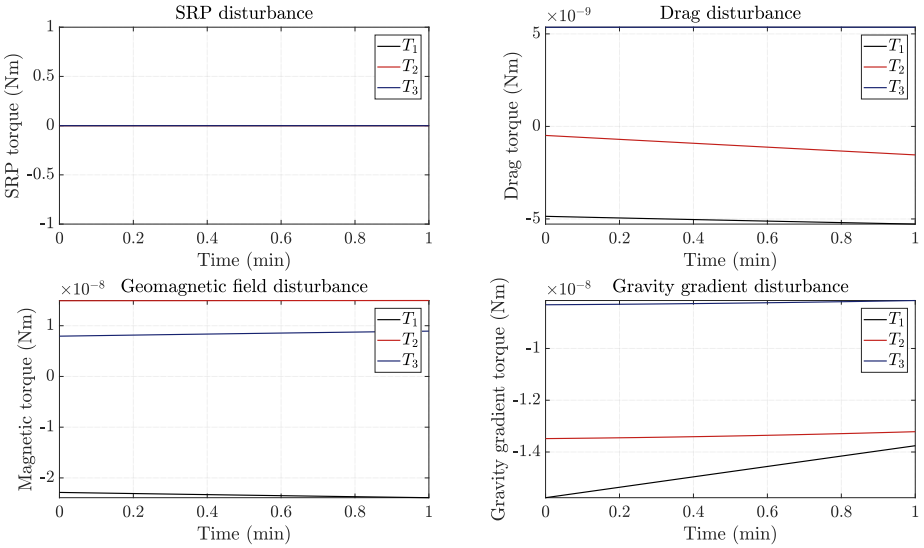

Figure B.14: *Main disturbances torques during de-saturation phase 2, in mission 1, on SSO. T_i are the torques components in body-fixed reference frame.*

Downloading Downloading phase above Liége lasts 5 minutes and the solver absolute and relative tolerances were set to 10^{-6} both. The steady state is reached after around 120 seconds.

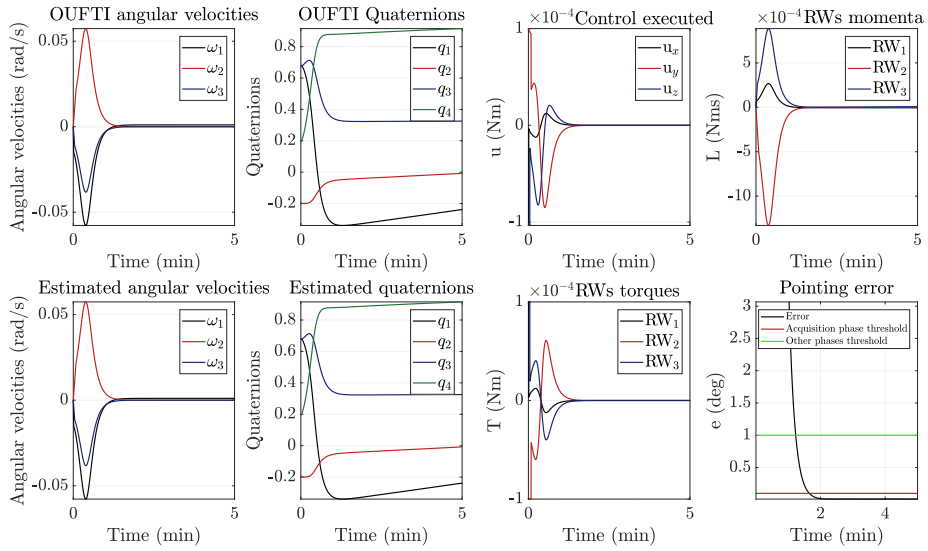

Figure B.15: *Most important results during downloading phase, in mission 1, on SSO. The plots are zoomed in order to catch the most interesting behaviors.*

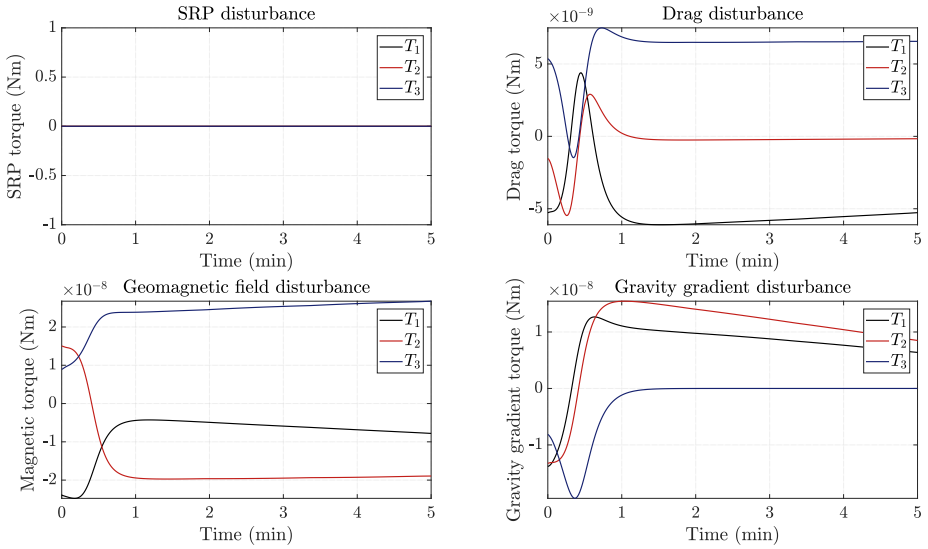

Figure B.16: *Main disturbances torques during downloading phase, in mission 1, on SSO. T_i are the torques components in body-fixed reference frame.*

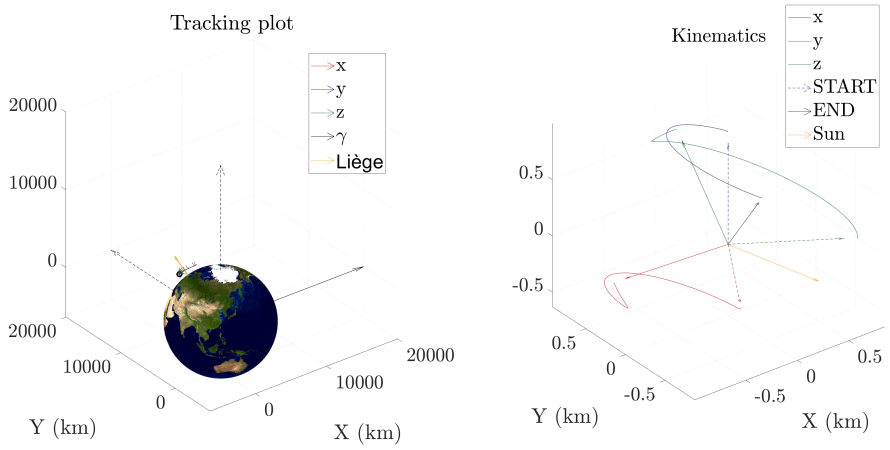

Figure B.17: *Body-fixed frame while orbiting around the earth during downloading phase, in mission 1, on SSO.*

Mission 3

Computational time usually requested: around 50 minutes, depending on the initial conditions. De-tumbling phase is not reported since it is almost equal to the one presented in Mission 1 results.

Sun-pointing The simulation lasts around 89 hours, the maximum time interval before saturation in Sun-pointing, with solver absolute and relative tolerances set to 10^{-6} both. The steady state is reached in less than 100 seconds.

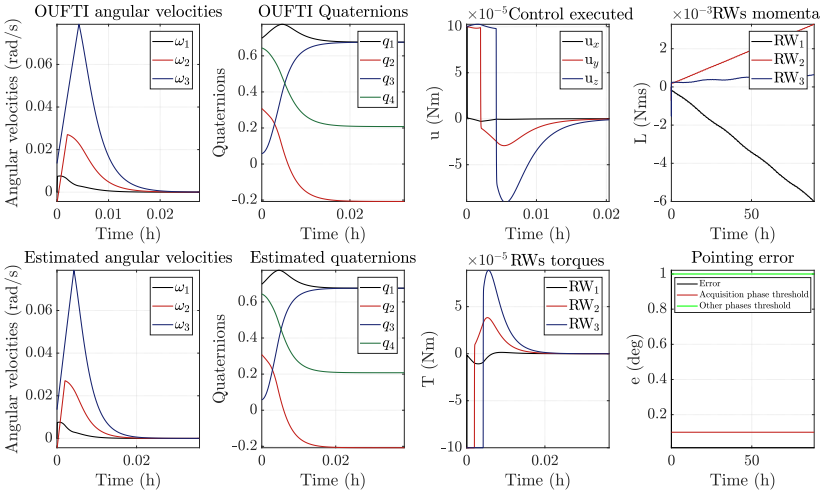

Figure B.18: *Most important results during Sun-pointing phase in mission 3, on SSO. The plots are zoomed in order to catch the most interesting behaviors.*

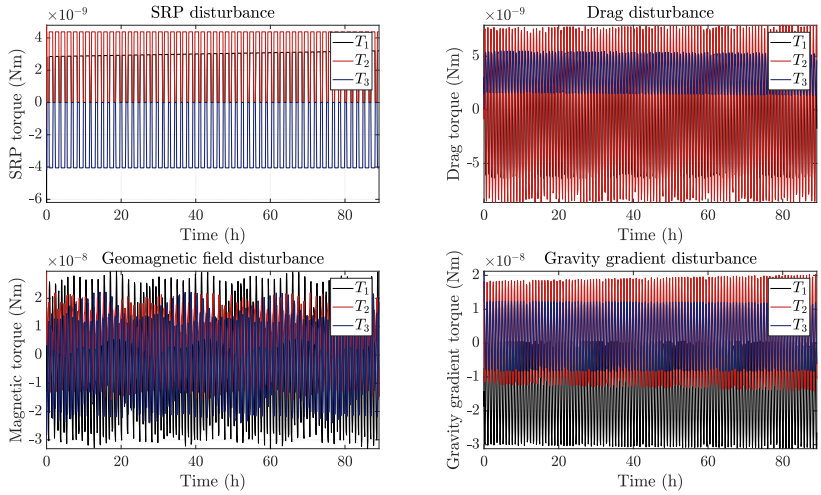

Figure B.19: *Main disturbances torques during Sun-pointing phase in mission 3, on SSO. T_i are the torques components in body-fixed reference frame.*

De-saturation De-saturation phase lasts one day, with solver absolute and relative tolerances set to 10^{-6} each.

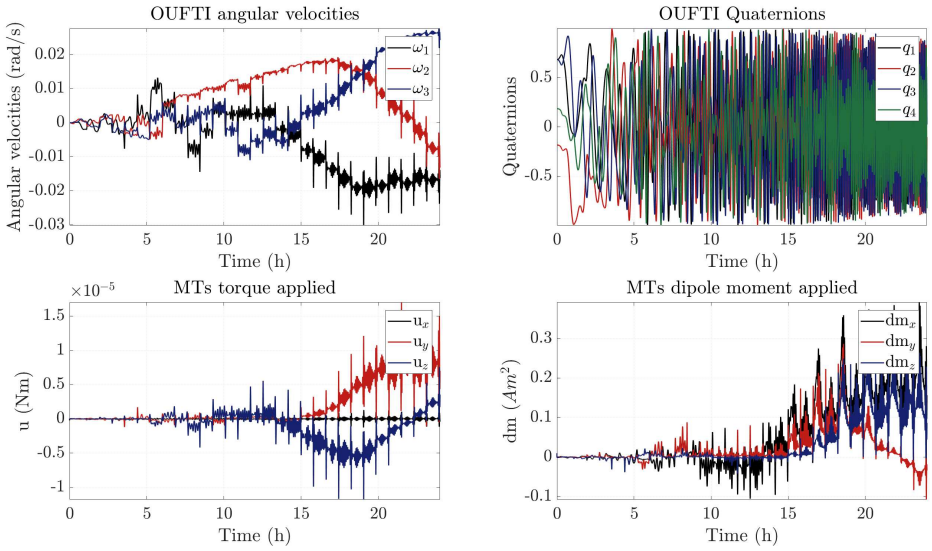

Figure B.20: *Most important results during de-saturation phase in mission 3, on SSO.*

In Figure B.21 it is clear that the angular velocity of the platform remains almost bounded inside 0.025 rad/s and −0.03 rad/s, meaning that it is still possible to store solar energy during shorter de-saturation phases.

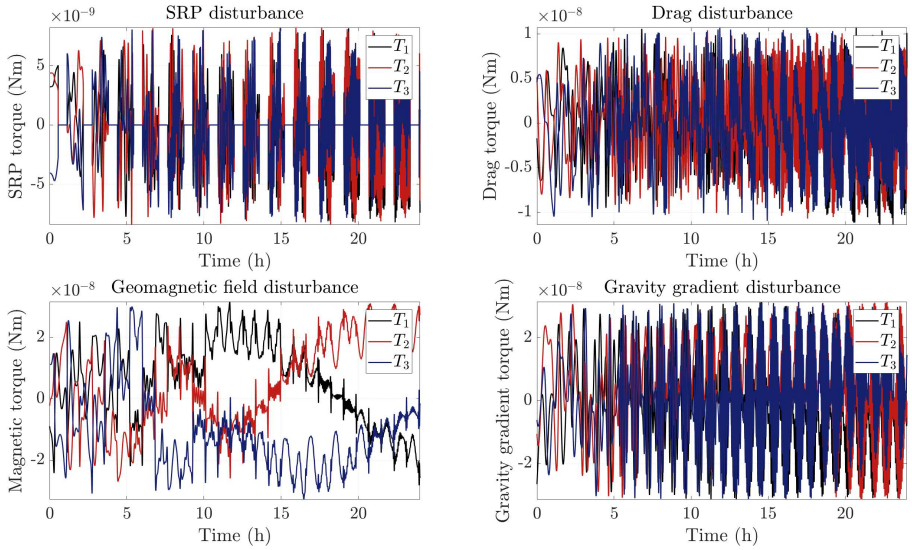

Figure B.21: *Main disturbances torques during de-saturation phase, in mission 3, on SSO. T_i are the torques components in body-fixed reference frame.*

Mission 1 with target following pointing

For what concerns mission 1 performed with target following pointing, here it is reported just the picture acquisition phase. The computational time requested to simulate the whole mission is usually around 10 minutes. From Figure B.22 it is possible to appreciate the angular velocity around Z-axis increasing and decreasing while the OUFTI-Next platform is passing over the target, rotating in order to follow the National Park of Brasilia, as well as the smooth drop of pointing error, while passing above the target. The solver absolute and relative tolerances are were to 10^{-6}.

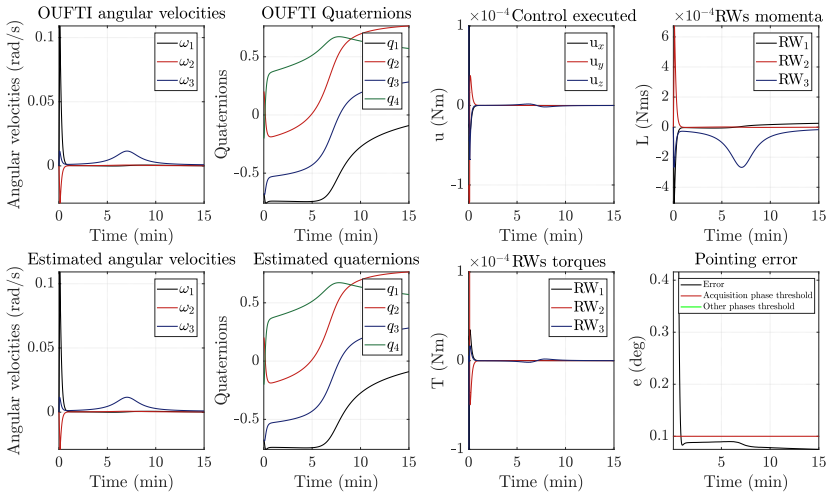

Figure B.22: *Most important results during picture acquisition phase, in mission 1, on SSO. The plots are zoomed in order to catch the most interesting behaviors.*

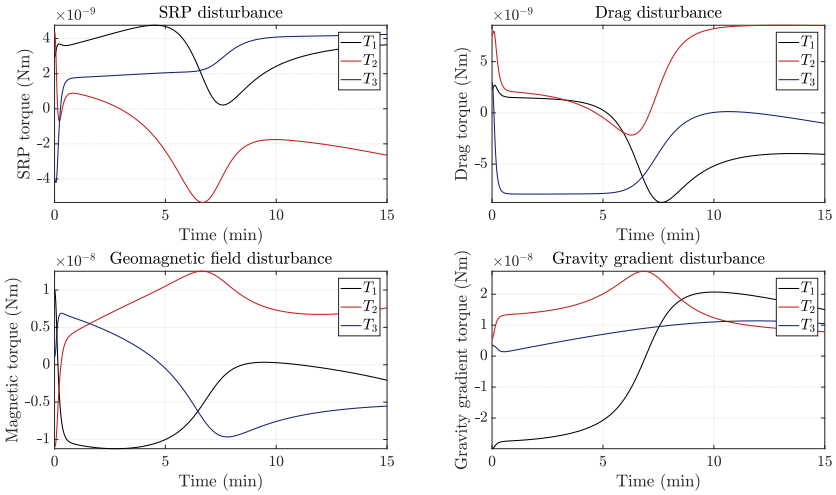

Figure B.23: *Main disturbances torques during picture acquisition phase, in mission 1, on SSO. T_i are the torques components in body-fixed reference frame.*

From Figure B.24 instead, it is possible to see the red vector (the X-axis of the body-fixed reference frame) following the National Park of Brasilia.

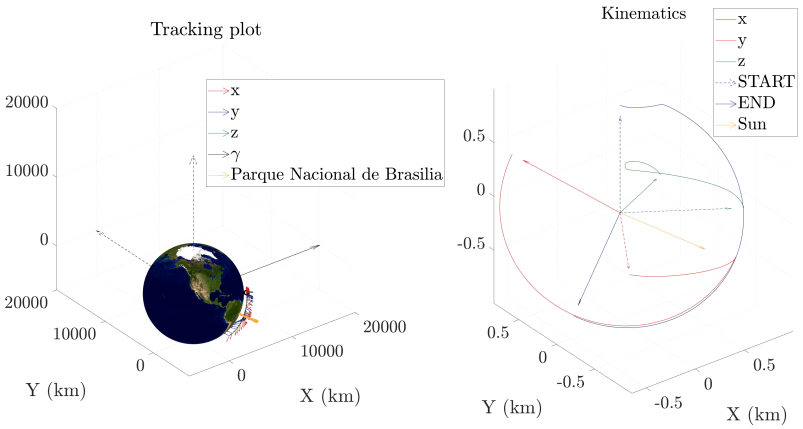

Figure B.24: *Body-fixed frame while orbiting around the earth during picture acquisition phase, in mission 1, on SSO.*

ACRONYMS & LIST OF SYMBOLS

Acronyms:

ADCS	Attitude Determination and Control System
COTS	Component Off The Shelf
COM	Communication Subsystem
CSL	center Spatial de Liége
ECI	Earth centered Inertial reference frame
EKF	Extended Kalman Filter
EPS	Electrical Power Subsystem
ESA	European Space Agency
GMT	Greenwich Mean Time
GNSS	Guidance and Navigation SubSystem
IR	InfraRed Radiation
ISS	International Space Station
KULeuven	Katholieke Universiteit Leuven
LMT	Local Mean Time
LVLH	Local Vertical Local Horizon
OBC	On-Board Computer
OUFTI-Next	Orbital Utility For Thermal Imaging Next

PD	Proportional Derivative law
PID	Proportional Integral Derivative law
PEET	Pointing Error Engineering Tool
PWR	Power Generation Subsystem
RAAN	Right Ascention of the Ascending Node
RC3BP	Restricted Circular 3 Body Problem
RMS	Root Mean Square
RW	Reaction Wheels
SRP	Solar Radiation Pressure
SSO	Sun Synchronous Orbit
TMTC	Telemetry & Telecommand
UKF	Unscented Kalman Filter
ULiége	University of Liége
WMM	World Magnetic Model

List of Symbols:

$\boldsymbol{A}$	Constant reaction wheels configuration matrix
$\boldsymbol{A_c}$	Sigma points partial generation matrix
$\boldsymbol{A_{b/l}}$	Rotation matrix from local to body-fixed frame
$\boldsymbol{A_{b/n}}$	Rotation matrix from inertial to body-fixed frame
$\boldsymbol{A_{b/n,real}}$	Real rotation matrix from inertial to body-fixed frame
$\boldsymbol{A_t}$	Desired attitude matrix
A_d	Area exposed to the atmospheric wind
$\boldsymbol{A_{l/n}}$	Rotation matrix from inertial to local frame
$\boldsymbol{A_{b/l}}$	Rotation matrix from local to body-fixed frame
A_s	Area exposed to the Sun radiation
$\boldsymbol{A_\epsilon}$	Bias matrix
$\boldsymbol{A_{\epsilon,B}}$	Magnetometers bias matrix
$\boldsymbol{A_{\epsilon,S}}$	Sun-sensors bias matrix
$\boldsymbol{B_b}$	Magnetic field vector in body fixed frame from magnetometers
$\boldsymbol{B_n}$	Magnetic field vector in inertial frame
C_d	Hypersonic drag coefficient
C_l	Hypersonic lift coefficient coefficient
C_r	Reflective coefficient
$\boldsymbol{F_{drag}}$	Drag force
$\boldsymbol{F_{lift}}$	Lift force
F_{lift}	Lift force magnitude
$\boldsymbol{F_k}$	Dynamical model
$\boldsymbol{F_{SRP}}$	Solar radiation pressure resulting force
H	Scale height
$\Gamma(x)$	Lyapunov function
$\boldsymbol{H_k}$	Measurements model
$\boldsymbol{I}$	Identity matrix
$\boldsymbol{I_z}$	The ZodiArt platform inertia matrix
I_i	Inertia
J	Cost function
J_2	Second order term of the Earth zonal harmonics
J_k	Zonal harmonics term
K	Kalman matrix
K_p	Proportional constant for PD controller
K_d	Derivative constant for PD controller
L	Number of states
M	Mean anomaly
$\boldsymbol{O_i}$	Vectors of star tracker observations in body frame
N	Number of surfaces

P_n^m	Schmidt quasi-normalized associated Legendre Polynomial
P_k	Legendre polynomial term
$\boldsymbol{P_k}$	Predicted covariance of the state error matrix
P_{SR}	Solar radiation pressure
P_1	Transformed covariance matrix
$P_{1,s}$	Transformed covariance of the state error matrix
$P_{1,m}$	Transformed covariance of the measurements matrix
P_{12}	Transformed cross-covariance of the state error
$\boldsymbol{Q_k}$	Additional covariance matrix uncertainty
R	Balloon radius
R_e	Earth radius
$\boldsymbol{R_k}$	Measurement uncertainty matrix
$\boldsymbol{R_r}$	Rotational matrix
$\boldsymbol{S}$	Satellite-Sun unit direction
$\boldsymbol{S_b}$	Sun direction in body fixed frame from Sun-sensors
$\boldsymbol{S_n}$	Sun direction in inertial frame from ephemeris
$\boldsymbol{S_i}$	Star position vectors from star catalogue
$\boldsymbol{T_{drag}}$	Torque due to drag
$\boldsymbol{T_{SRP}}$	Solar radiation pressure resulting torque
$\boldsymbol{T_{magnetic}}$	Torque due to Earth magnetic field interaction
$\boldsymbol{T_{gravity}}$	Torque due to gravity gradient
V	Earth magnetic field potential
$\boldsymbol{V_b}$	Body fixed frame TRIAD method matrix
$\boldsymbol{V_n}$	Inertial frame TRIAD method matrix
$\boldsymbol{X}$	Sigma points matrix
$\boldsymbol{Y}$	Unscented transformed state matrix
$\boldsymbol{Y_{ones}}$	$L \times L$ matrix full of ones
$\boldsymbol{Y_1}$	transformed deviation from the mean value matrix
$\boldsymbol{W_{m,c}}$	Kalman filter weight matrices
a	Semi-major axis
a_0	Initial semi-major axis
$\hat{c}$	Unscented Kalman filter constant
$\boldsymbol{d}$	Disturbances torque
$\boldsymbol{d_{int}}$	Internal disturbances torque
e	Eccentricity
e_0	Initial eccentricity
$\boldsymbol{f_k}(\hat{\boldsymbol{x_k}})$	Non linear dynamical model
$\boldsymbol{g_n^m}$	Tabulated Gaussian coefficients
$\boldsymbol{h_m}$	Angular momentum vector in inertial reference frame

$\boldsymbol{h_k(\hat{x_k})}$	Non linear measurement model
h_n^m	Tabulated Gaussian coefficients
$\boldsymbol{h_r}$	Reaction wheels angular momentum
$\boldsymbol{h_{r,0}}$	Initial reaction wheels angular momentum
h_0	Reference height
i	Inclination
i_0	Initial inclination
k_{DeT}	De-tumbling control constant
m	Mass
$\boldsymbol{m}$	Residual dipole moment
$\hat{\boldsymbol{n}}$	Normal unit vector
$\boldsymbol{n_i}$	Normal to i surface
$\boldsymbol{n_e}$	Measurement noise
$\boldsymbol{n_u}$	Drift rate ramp - Float torque derivative noise
$\boldsymbol{p}$	Perturbative vector in inertial reference frame
$\boldsymbol{p_{drag}}$	Perturbative vector due to atmospheric drag in inertial reference frame
$\boldsymbol{p_{obl}}$	Perturbative vector due to Earth oblateness in inertial reference frame
$\boldsymbol{p_{RC3BP}}$	Perturbative vector due to third body perturbation in inertial reference frame
$\boldsymbol{p_{SRP}}$	Perturbative vector due to solar radiation pressure in inertial reference frame
$\boldsymbol{q}$	Quaternion
$\boldsymbol{q_0}$	Initial quaternion
q	Standard deviation of the process
$\boldsymbol{q_c}$	Control quaternion
$\boldsymbol{q_e}$	Quaternion error
$\boldsymbol{r}$	Position vector in inertial reference frame
$\hat{\boldsymbol{r}}$	Position unit vector in inertial reference frame
r	Position vector magnitude
r_m	standard deviation of the measurements
$\boldsymbol{r_b}$	Vector connecting the body center of mass to the infinitesimal cube of mass dm
$\boldsymbol{r_{cp}}$	Vector from center of mass to center of pressure
$\hat{\boldsymbol{r}}_{\boldsymbol{s}}$	Sun direction unit vector
s	Spinning velocity
$\boldsymbol{v}$	Velocity vector in inertial reference frame
$\bar{\boldsymbol{v}}$	Velocity unit vector in inertial reference frame
$\tilde{\boldsymbol{v}}$	Measurements mean value
$\boldsymbol{v_{atm}}$	Earth atmospheric velocity vector
$\boldsymbol{v_{rel}}$	Relative velocity vector
$\hat{\boldsymbol{v}}_{\boldsymbol{rel}}$	Relative velocity unit vector
t	time
$\boldsymbol{u}$	Control torque

$\boldsymbol{u_d}$	Desired control torque
$\boldsymbol{u_r}$	Executed real control torque
$\boldsymbol{x}$	State vector
$\boldsymbol{x'}$	Estimated state
$\boldsymbol{\hat{x}_p}$	Body fixed reference frame x-axis unit vector
$\boldsymbol{y}$	Unscented transformed mean value vector
$\boldsymbol{\hat{y}_p}$	Body fixed reference frame y-axis unit vector
$\boldsymbol{z_k}$	Measurement
$\boldsymbol{\hat{z}_p}$	Body fixed reference frame z-axis unit vector
α	Angle of attack
$\hat{\alpha}$	Unscented Kalman filter constant
β	Unscented Kalman filter constant
γ	Vernal direction
δt	Sampling time
$\zeta_{e,u}$	Normally distributed random variable with 0 mean value and standard deviation 1
θ	True anomaly
θ_0	Initial true anomaly
$\hat{\theta}$	Accuracy on X-axis
$\tilde{\theta}$	Latitude measured in degrees positive from the equator
λ	Eigenvalue
$\hat{\lambda}$	Unscented Kalman filter constant
λ_{Sun}	True longitude of the Sun
μ	Planetary constant
$\boldsymbol{\hat{\mu}_{expected}}$	Expected measurement
Φ	Perturbation of the gravitational potential due to planet oblateness
ϕ	Angle between the Sun-Earth line and the direction of the orbit pericentre
$\hat{\phi}$	Accuracy on Y-axis
$\tilde{\phi}$	Earth fixed longitude measured in degrees positive from the equator
ρ	Atmospheric density
ρ_a	Surface absorption coefficient
ρ_d	Surface diffusive coefficient
ρ_s	Surface scattering coefficient
ρ_0	Reference density at 0 km height
$\boldsymbol{\sigma}$	Standard deviation vector
σ_ϵ	Standard deviation of the gyroscopescopes measurements
σ_u	Standard deviation of the gyroscopescopes drift rate ramp
τ	Time shift
τ_{AN}	Local Mean Time at Ascending Node
ψ	Polar angle

$\hat{\psi}$	Accuracy on Z-axis
ω	Anomaly of the perigee
ω_0	Initial anomaly of the perigee
$\boldsymbol{\omega}$	Angular velocity vector
$\boldsymbol{\omega_0}$	Initial angular velocity vector
$\boldsymbol{\omega_{b/n}}$	Angular velocity in body fixed reference frame
$\boldsymbol{\omega_t}$	Desired angular velocity
$\omega_\oplus$	Earth angular velocity
ω_{orbit}	Satellite angular velocity on orbit
$\hat{\boldsymbol{\Sigma}}_{\boldsymbol{expected}}$	Measurements covariance matrix expected
Ω	Right ascension of the ascending node
Ω_0	Initial Right ascension of the ascending node

BIBLIOGRAPHY

[1] Colombo C. Dal Monte L. *Zodiart iSEE mission*. Technical Report. 2017 (cit. on pp. 3, 109, 110).

[2] Ylén J. Riihimäki P. "Simulation of spacecraft attitude and orbit dynamics". In: *Simulation in Wider Europe–ECMS* (2005), pp. 1–4 (cit. on p. 4).

[3] *2017 Nano/Microsatellites Market Forecast*. URL: `http://asa.usno.navy.mil` (visited on 08/01/2018) (cit. on p. 4).

[4] Kelecy T.M. Jah M.K. Früh C. "Coupled orbit-attitude dynamics of high area-to-mass ratio (HAMR) objects: Influence of solar radiation pressure, Earth's shadow and the visibility in light curves". In: *Celestial Mechanics and Dynamical Astronomy* 117.4 (2013), pp. 385–404 (cit. on p. 4).

[5] Gurfil P. Ben-Yaacov O. "Long-term cluster flight of multiple satellites using differential drag". In: *Journal of Guidance, Control, and Dynamics* 36.6 (2013), pp. 1731–1740 (cit. on pp. 4, 116, 130).

[6] Nikolaev S. Pertica A. Horsley M. *Rendezvous Maneuvers of Small Spacecraft Using Differential Lift and Drag*. Tech. rep. Lawrence Livermore National Laboratory (LLNL), Livermore, CA, 2011 (cit. on pp. 4, 19).

[7] *Pointing Error Engineering Tool (PEET)*. URL: `http://peet.estec.esa.int/` (visited on 11/01/2018) (cit. on pp. 5, 98, 105).

[8] Fang J. Cui P. Sun K. "Anti-disturbance cooperative control for configuration and attitude of satellite formation". In: *Instrumentation and Control Technology (ISICT), 2012 8th IEEE International Symposium on*. IEEE. 2012, pp. 251–256 (cit. on p. 5).

[9] S.E. Lennox. "Coupled attitude and orbital control system using spacecraft simulators". PhD thesis. Virginia Tech, 2004 (cit. on p. 5).

[10] S.P. Altman. "A unified state model of orbital trajectory and attitude dynamics". In: *Celestial mechanics* 6.4 (1972), pp. 425–446 (cit. on p. 5).

[11] Dalla Vedova F. Colombo C. Gkolias I. "Preliminary end-of-life design report, the revolutionary design of spacecraft through holistic integration of future technologies - ReDSHIFT, D. 4.6". In: (November 2016) (cit. on p. 5).

[12] *Ideal Lift of a Spinning Ball*. URL: `https://www.grc.nasa.gov/www/k-12/airplane/beach.html` (visited on 10/25/2018) (cit. on pp. 5, 119).

[13] Menzio D. Romano M. Huang S. Rossi A. Volker Schaus Tonetti S. Colombo C. ""Review of the state-of-the-art and reference simulation results", The revolutionary design of spacecraft through holistic integration of future technologies ReDSHIFT project, Deliverable 2.1". In: (November 2016) (cit. on p. 5).

[14] Van Breukelen E.D. Zandbergen B.T.C. Bergsma O.K. Maessen D.C. "Development of a generic inflatable de-orbit device for CubeSats". In: *Proceedings of the 58th International Astronautical Congress, India*. 2007 (cit. on p. 5).

[15] Hubbs W. Stanaland T. Hollerman A. Altstatt R.L. Edwards D.L. "Characterization of space environmental effects on candidate solar sail material". In: *Photonics for Space Environments VIII*. Vol. 4823. International Society for Optics and Photonics. 2002, pp. 67–75 (cit. on p. 6).

[16] *The humanity star*. URL: `https://www.thehumanitystar.com/` (visited on 10/28/2018) (cit. on p. 6).

[17] M.P. Roccioletti. "Mission Analysis and concept design for a reflective balloon mission". Master Thesis, Supervisor: Colombo C. Politecnico di Milano, 2018 (cit. on pp. 6, 109–114, 120, 122, 127, 139, 140).

[18] *Echo I, a Balloon Satellite*. URL: `https://www.nasa.gov/multimedia/imagegallery/image_feature_2124.html` (visited on 11/01/2018) (cit. on p. 6).

[19] *Gossamer Orbit Lowering Device (GOLD) for Low-risk Satellite De-orbit*. URL: `http://gaerospace.com/projects/GOLD/applications.html` (visited on 11/28/2018) (cit. on p. 6).

[20] H. Curtis. *Orbital Mechanics: for Engineering Students*. Second Edition. Aerospace Engineering. Butterworth Heinemann, 2010 (cit. on pp. 10, 15–18, 61).

[21] Palais R. Rodi S. Palais B. "A Disorienting Look at Euler's Theorem on the Axis of a Rotation". In: *The American Mathematical Monthly* 116.10 (2009), pp. 892–909 (cit. on p. 10).

[22] J.A. Schetz. *Analytical Mechanics of Space Systems, Third Edition*. AIAA Education Series, 2014 (cit. on pp. 11, 36, 37).

[23] T.I. Fossen. *Handbook of Marine Craft Hydrodynamics and Motion Control*. JohnWiley & Sons Ltd., 2011 (cit. on p. 12).

[24] C. Bewick. "Space mission applications of high area-to-mass-ratio orbital dynamics". PHD Thesis. University of Strathclyde, 2013 (cit. on pp. 17, 114).

[25] D.D. Vallado. *Fundamentals of Astrodynamics and Applications*. Space Technology Series. McGraw Hill, 1997 (cit. on pp. 18, 22).

[26] J.R. Wertz. *Space Mission Analysis and Design, Ed. 3*. Space Technology Library, 1999 (cit. on pp. 19, 61).

[27] P. Moore. "The effect of aerodynamic lift on near-circular satellite orbits". In: *Planetary and space science* 33.5 (1985), pp. 479–491 (cit. on pp. 19, 117).

[28] C.L. Pulido. "Aerodynamic Lift and Drag Effects on the Orbital Lifetime Low Earth Orbit (LEO) Satellites". In: *University of Colorado Boulder* (2007) (cit. on pp. 19, 117).

[29] Wie Bong. *Space Vehicle Dynamics and Control*. AIAA Education Series. 2006 (cit. on p. 20).

[30] Inc. The MathWorks. *wrldmagm.m*. URL: `https://it.mathworks.com/help/aerotbx/ug/wrldmagm.html` (visited on 08/09/2018) (cit. on p. 23).

[31] J. Davis. "Mathematical modeling of Earth's magnetic field". In: *Technical Note* (2004), pp. 1157–1163 (cit. on pp. 23, 66).

[32] J.D. Biggs. *Spacecraft Attitude Dynamics and Control course*. 2017 (cit. on pp. 25, 26, 34, 99).

[33] Bzarg. *How a Kalman filter works, in pictures*. Aug. 10, 2015. URL: https://www.bzarg.com/p/how-a-kalman-filter-works-in-pictures/ (cit. on pp. 26–30).

[34] Van Der Merwe R. Wan E.A. "The unscented Kalman filter for nonlinear estimation". In: *Adaptive Systems for Signal Processing, Communications, and Control Symposium 2000. AS-SPCC. The IEEE 2000*. Ieee. 2000, pp. 153–158 (cit. on p. 31).

[35] Jensen K.F. Larsen J.A. Wisniewski R. Vinther K. "Inexpensive cubesat attitude estimation using quaternions and unscented Kalman filtering". In: *Automatic Control in Aerospace* 4.1 (2011), pp. 1–12 (cit. on p. 32).

[36] Adi Ben-Israel and Thomas NE Greville. *Generalized inverses: theory and applications*. Vol. 15. Springer Science & Business Media, 2003 (cit. on p. 34).

[37] *The Astronomical Almanac Online*. URL: http://www.spaceworkscommercial.com/wp-content/uploads/2018/01/SpaceWorks_Nano_Microsatellite_Market_Forecast_2017.pdf (visited on 09/01/2018) (cit. on pp. 34, 35).

[38] Engelen S. Buhl M. Monna B. Segert T. "iADCS-100, an Autonomous Attitude Determination and Control Subsystem based on Reaction Wheels and Star Tracker in 1/3U Package". In: *Small Satellites Systems and Services, The 4S Symposium 2012*. 2012 (cit. on p. 38).

[39] Prince P.J. Dormand J.R. "A family of embedded Runge-Kutta formulae". In: *Journal of computational and applied mathematics* 6.1 (1980), pp. 19–26 (cit. on p. 39).

[40] Reichelt M.W. Shampine L.F. "The matlab ode suite". In: *SIAM journal on scientific computing* 18.1 (1997), pp. 1–22 (cit. on p. 39).

[41] Shampine L.F. Bogacki P. "A 3 (2) pair of Runge-Kutta formulas". In: *Applied Mathematics Letters* 2.4 (1989), pp. 321–325 (cit. on p. 39).

[42] Gordon M.K. Shampine L.F. *Computer solution of ordinary differential equations: the initial value problem*. 1975 (cit. on p. 39).

[43] Reichelt M.W. Kierzenka J.A. Shampine L.F. "Solving index-1 DAEs in MATLAB and Simulink". In: *SIAM review* 41.3 (1999), pp. 538–552 (cit. on p. 39).

[44] Kofman E. Cellier F.E. *Continuous system simulation*. Springer Science & Business Media, 2006 (cit. on pp. 40, 41, 45, 46).

[45] *Stability Regions of ODE Formulas*. URL: https://www.mathworks.com/matlabcentral/mlc-downloads/downloads/submissions/23972/versions/22/previews/chebfun/examples/ode/html/Regions.html (visited on 11/01/2018) (cit. on p. 41).

[46] C. Dandumont. "From mission analysis to systems engineering of the OUFTI-Next nanosatellite". Master Thesis. University of Liége, 2018 (cit. on pp. 51–59, 67, 69, 103).

[47] *IADC Space Debris Mitigation Guidelines*. Sept. 2007. URL: http://www.unoosa.org/documents/pdf/spacelaw/sd/IADC-2002-01-IADC-Space_Debris-Guidelines-Revision1.pdf (visited on 11/10/2018) (cit. on pp. 54, 55, 116, 139).

[48] A.R. Salva. "Oufti-Next: Design of refractive lenses for an infrared camera". Master Thesis. University of Liége, 2018 (cit. on p. 59).

[49] D. Calozet. "Study of a IR reflective optical system for Earth observation from a 3U CubeSat". Master Thesis. University of Liége, 2018 (cit. on p. 59).

[50] *iADCS100 Attitude Determination And Control System*. Flyer. 2016 (cit. on pp. 59–61, 95).

[51] Bremer S. Rievers B. Selig H. List M. "Modelling of solar radiation pressure effects: Parameter analysis for the microscope mission". In: *International Journal of Aerospace Engineering* 2015 (2015) (cit. on pp. 60, 114).

[52] Cutler J. Bahcivan H. Springmann J. "Magnetic sensor calibration and residual dipole characterization for application to nanosatellites". In: *AIAA/AAS Astrodynamics Specialist Conference*. 2010, p. 7518 (cit. on p. 60).

[53] *Hyperion Technologies: KIVI SYMPOSIUM - KLEINE RUIMTEVAART*. URL: https://www.kivi.nl/uploads/media/58b03b4385a8f/Ruimtevaart-Bert%20Monna-Hyperion.pdf (cit. on p. 61).

[54] A. Pignéde. "Detumbling of the NTNU Test Satellite". Master Thesis. Norwegian University of Science and Technology, 2014 (cit. on pp. 64, 70).

[55] P.J. Olver. *Introduction to partial differential equations*. Springer, 2014 (cit. on p. 65).

[56] *KULeuven ADCS Accurate and Agile Attitude Determination and Control for CubeSats*. Flyer. 2018 (cit. on pp. 87, 95, 98).

[57] H.D. Black. "A passive system for determining the attitude of a satellite". In: *AIAA journal* 2.7 (1964), pp. 1350–1351 (cit. on p. 100).

[58] *About the Sustainable Development Goals*. Sept. 2018. URL: https://www.un.org/sustainabledevelopment/ (cit. on pp. 109, 110).

[59] *Grossamer Orbit Lowering Device (GOLD) for Safe and Efficient CubeSat Deorbit*. URL: http://mstl.atl.calpoly.edu/~workshop/archive/2015/Summer/Day%202/0940-SarziAmade-GOLD.pdf (visited on 10/11/2018) (cit. on p. 110).

[60] Moe K. Bowman B.R. "Drag coefficient variability at 175-500 km from the orbit decay analyses of spheres". In: *Paper AAS 05-257 presented at the AIAA/AAS Astrodynamics Specialist Conference. Lake Tahoe, California*. 2005 (cit. on p. 116).

[61] *Moving mean*. URL: https://it.mathworks.com/help/matlab/ref/movmean.html (visited on 11/01/2018) (cit. on p. 120).

[62] Lücking C. McInnes C.R. Colombo C. "Orbital dynamics of high area-to-mass ratio spacecraft with J2 and solar radiation pressure for novel Earth observation and communication services". In: *Acta Astronautica* 81.1 (2012), pp. 137–150 (cit. on pp. 120–122).

[63] *Rockwell Collins Products and Serivces*. Oct. 26, 2018. URL: https://www.rockwellcollins.com/Products-and-Services/Defense/Platforms/Space/RSI-12-Momentum-and-Reaction-Wheels.aspx (visited on 10/24/2018) (cit. on p. 123).

[64] *Magnetic Torquers for Spacecraft Attitude Control*. URL: https://www.yumpu.com/en/document/view/12694201/magnetic-torquers-for-spacecraft-attitude-control-zarm-technik-ag (visited on 10/24/2018) (cit. on p. 123).

[65] Lovera M. Silani E. "Magnetic spacecraft attitude control: a survey and some new results". In: *Control Engineering Practice* 13.3 (2005), pp. 357–371 (cit. on p. 123).

Colophon

This document was typeset using the typographical look-and-feel `PhD_Dis` developed by Diogene Alessandro Dei Tos. The style is inspired by J. Stevens and L. Fossati *phdthesis Style*.

`PhD_Dis` is available for both LaTeX and LyX:

`https://gitlab.com/diogene/PhD_Dis.git`